Direct Numerical Simulation of Evaporation and Burning of a Fuel Droplet

by

Muhammad Irfan

A Dissertation Submitted to the
Graduate School of Sciences and Engineering
in Partial Fulfillment of the Requirements for
the Degree of

Doctor of Philosophy

in

Mechanical Engineering

September, 2017

Direct Numerical Simulation of Evaporation and Burning of a Fuel Droplet

Koç University

Graduate School of Sciences and Engineering

This is to certify that I have examined this copy of a doctoral dissertation by

Muhammad Irfan

and have found that it is complete and satisfactory in all respects,
and that any and all revisions required by the final
examining committee have been made.

Committee Members:

_____

Prof. Dr. Metin Muradoglu

_____

Assoc. Prof. Dr. Murat Sozer

_____

Prof. Dr. Alper Kiraz

_____

Assoc. Prof. Dr. Mehmet Sahin

_____

Assoc. Prof. Dr. Onur Tuncer

Date: _____

To my family

ABSTRACT

A front-tracking method is developed for the Direct Numerical Simulation (DNS) of droplet evaporation and combustion in a liquid-gas multiphase system. One field formulation is used to solve the flow, energy and species equations with suitable jump conditions. Both phases are assumed to be incompressible; however, the divergence-free velocity field condition is modified to account for the phase change at the interface. Both temperature and species gradient driven phase change processes/models are simulated in 2D planar configuration. For the species gradient driven phase change process, the Clausius-Clapeyron equilibrium relation is used to find the vapor mass fraction and subsequently the evaporation mass flux at the interface. Extensive validation studies are performed using the benchmark cases: The Stefan and the sucking interface problems, d^2-law and the wet bulb temperature comparison with the psychrometric chart values. The models are then applied to simulate the evaporation of a single and two droplets systems that move, evaporate, interact and undergo significant deformation in a gravitational field. The implementations have been demonstrated to be grid convergent and the global mass conservation is satisfied for all the studied cases.

The temperature gradient based phase change model is then incorporated into the axisymmetric multiphase solver and comprehensive validation studies are performed. This is then further extended to model the burning process following the evaporation as a first step towards the development of a computational framework for the direct numerical simulations of spray combustion. We used single step as well as reduced chemical kinetic mechanism, constant thermodynamic properties, unity Lewis number for all the species and an ideal gas behaviour for a n-heptane droplet combustion; the chemical kinetics being handled by the CHEMKIN. An operator-splitting approach is

used to advance temperature and species mass fractions in time. The numerical results of the droplet burning rate, flame temperature, flame standoff ratio and ignition delay times show good agreement with the experimental and previous numerical studies.

ÖZETÇE

Sıvı-gaz çok fazlı akışkan sisteminde sıvı damlacığın buharlaşması ve yanmasının doğrudan simülasyonu için yeni bir ara-yüz izleme yöntemi geliştirildi. Akış, enerji ve bileşenlerin kütle korunum denklemleri tek-alan formülasyonu ve uygun ara-yüz sınır koşulları kullanılarak çözüldü. Bu çalışmada hem sıvı hem de gaz fazlarının sıkıştırılamaz olduğu varsayıldı. Bununla birlikte faz değişimi olmayan sıkıştırılamaz akışlar için geçerli olan hız alanının divarjansının sıfır olması prensibi faz değişimini hesaba katmak amacıyla ara-yüzeyde modifiye edildi. Sıcaklık ve konsantrasyon gradyantı kaynaklı damlacık buharlaşması için sayısal yöntem geliştirildi ve simülasyonlar yapıldı. Konsantrasyon gradyantı nedeniyle oluşan faz değişiminde, ara-yüzeydeki buhar kütle akısının hesaplanmasında Clausius-Clapeyron denge kanunundan yararlanıldı. Sayısal yöntemin doğrulanması için çok sayıda test problemi kullanıldı. Bu amaçla Stefan ve emme ara-yüz problemleri, d^2-kanunu ve ıslak termometre problemleri için hesaplamalar yapıldı ve sonuçlar analitik çözümlerle karşılaştırıldı. Sayısal yöntem daha sonra yerçekimi ile düşmekte olan ve bu esnada önemli ölçüde deformasyona uğrayan ve etkileşen tekil ve ikili damlacıkların buharlaşması problemlerine uygulandı. Sayısal yöntemin çözüm ağı yakınsamasının olduğu ve toplam kütlenin korunumu prensibinin sayısal çözüm seviyesinde sağlandığı gösterildi.

Sıcaklık gradyantına dayalı faz değişimi modeli daha sonra aksi-simetrik problemlere uyarlandı ve çok sayıda doğrulama testi yapıldı. Buna ilave olarak, sayısal yöntem damlacık buharlaşmasını takip eden yanma prosesini de içerecek şekilde genelleştirildi. Bu sayede sprey yanmasının doğrudan simülasyonu için geliştirilmekte olan sayısal yönteme doğru ilk adım atılmış oldu. Kimyasal kinetik denklemlerin etkin çözümü için CHEMKIN paketi sayısal yönteme entegre edildi. Kimyasal kinetik denklemlerinin akış denklemleriyle birlikte çözülmesinde operatör-ayrıştırma yöntemi kul-

lanıldı. Sayısal yöntem tek-adımlı çok basit bir kimyasal kinetik modeli yanında indirgenmiş detaylı kimyasal kinetik modeli de kullanılarak n-heptan damlacığının buharlaşması ve yanmasına başarıyla uygulandı. Elde edilen sonuçlar deneysel veriler ve literatürdeki önceki sayısal çalışmalarla karşılaştırıldı. Mevcut sonuçların damlacık yanma oranı, alev sıcaklığı, alev durma oranı ve tutuşma gecikme zamanı açısından deneysel veriler ve önceki sayısal çözümlerle uyumlu olduğu gösterildi.

ACKNOWLEDGMENTS

I am really gratefully to my thesis advisor Prof. Dr. Metin Muradoglu for granting me the opportunity to work on such an interesting and rich topic. His guidance, motivation, expert advice and innovative ideas made my journey smoother and joyful. It was really an honor working with him. I am thankful to the thesis monitoring committee members Prof. Dr. Alper Kiraz and Prof. Dr. Murat Sozer for their valuable inputs for presentation improvement, constructive ideas during the progress meetings and critical reading of the thesis draft. I would also like to thank the jury members for sparing their precious time and valuable comments for improving the thesis. I really enjoyed working with exceptional people in our research group. I would like to thank Dr. Daulet Izbassarov and Dr. Hasret Turkeri for fruitful discussions.

I would like to thank my parents and family for encouraging me during the toughest times and their understanding when i was not able to spare time for them. It was their unending support that helped me turning my dream into a reality.

I always felt privileged being a scholar of Higher Education Commission of Pakistan. It was indeed a source of pride, motivation and great honor for me and a turning point in my career.

All departments of the Koc University are in true sense a big contributors to what we achieve. I would especially like to mention the GSSE staff officials for making official things easier for us. Koc library contributed alot in the form of research articles, i would like to mention Mr. Deniz Han and Ms. Emine Cengiz for their help in providing articles. Most of the computations in the present work are performed at HPC facility of the Koc University for which i am thankful to the whole team.

TABLE OF CONTENTS

LIST OF TABLES

LIST OF FIGURES

Chapter 1

INTRODUCTION

1.1 Motivation and Literature Survey

Interfacial flows are frequent occurrences in nature, industrial processes and biological systems. Air/gas bubbles rising in a water bed under buoyancy, a free-falling rain droplet in air, core annular flows for oil/gas transportation in petroleum industries, breathing system in living organisms are some of the examples involving multiphase flows; where interfaces move, deform and even topological changes occur during the course of time. In addition to experiments, the numerical simulations have become an indispensable tool for the medical and the industrial sector to help improve their products and system designs for maximum efficiency. Over decades, researchers have developed various numerical techniques to simulate multiphase flows. It is quite a challenging task to simulate multiphase flows in the sense that sharp property gradients exist across the interfaces, which evolve and undergo substantial deformations including topological changes.

Harlow and Welch [1] proposed one of the first methods to simulate free surface flows: the marker and cell method. In this method, marker particles are spread in the fluid region. These particles move with the local fluid velocity and therefore defines the interface shape and location at current time. Instead of many marker particles per mesh cell, Hirt and Nichols [2] came up with a memory efficient region-following scheme, called the volume of fluid (VOF) method, with a single value of fluid volume fraction in each mesh cell. Interface can also be viewed as a level set function; the technique has been successfully implemented by various authors to simulate multi-

phase flows [3, 4]. In order to keep the level set function continuous and well resolved, the level set function is maintained as a signed distance function for all the time, without reconstructing the interface [4]. The notion of diffuse interface has also been used to model the interfacial flows [5]. Jacqmin [6] performed critical test cases to show the ability of the phase field method to simulate two phase flows. All the above mentioned methods fall under the category of interface capturing method. The second category may be called as interface tracking method, in which the interface is represented by a separate Lagrangian grid, whereas the governing equations are solved on the background Eulerian mesh. In some earlier implementations, the moving interface is tracked by modifying the background Eulerian grid near the interface such that the fixed grid lines follow the interface [7, 8, 9]. Tryggvason et al. [10, 11] devised a front tracking method, which does not require any re-meshing of the background grid to track the interface. Rather, the interface or front is explicitly tracked by interpolating the velocity field from the Eulerian grid onto the interface marker points.

The phase change phenomenon adds another dimension to the interfacial flows and thus makes modeling even more challenging. Condensation, solidification, dissolution, boiling and vaporization/evaporation are different phase change processes that are frequently encountered in nature and industrial applications. Design of heat exchangers and boilers for efficient heat transfer, achieving uniform material properties through casting process, efficient burning of fuel droplets in internal combustion engines and the dissolution of drugs in human body are some of the application areas, where a better understanding of the physical processes and the design parameters is expected to result in increased system efficiencies and better health standards. The ever rising computational powers have proven Direct Numerical Simulation (DNS) a promising technique to simulate and analyze the designs for the system performance under a wide range of operating parameters. Also, with the advent of micro and nano-scale applications, the direct numerical simulation has proven to be an efficient tool in design improvement of the systems, where experimentation has serious limitations [12].

Researchers have applied different multiphase flow modeling techniques to simulate different phase change phenomena. Welch and Wilson [13] studied horizontal film boiling problem using a VOF method. Detailed numerical simulation of 3D evaporating and strongly deformed droplet was performed by Schlottke and Weigand [14] using the VOF method. Film boiling case has been studied using a level set method by Son and Dhir [15] and Gibou et al. [16]. The level set method, in combination with the ghost fluid method [17], has been used to simulate evaporation of a moving and deforming droplet by Tanguy et al. [18]. Another promising numerical scheme to model and simulate multiphase flow is the lattice Boltzmann method. Safari et al. incorporated the temperature [19] and species gradient [20] based phase change models into the lattice Boltzmann method developed by Lee [21].

The original front-tracking method developed for isothermal multifluid flows by Tryggvason and coworkers [10, 11] has been extended by various researchers to include the mass transfer and the phase change phenomena. For example, Juric and Tryggvason [22] simulated the film boiling. They used an iterative procedure to set the correct temperature boundary condition at the interface. The same procedure has also been used to track the flame front of a premixed flame by Qian et al. [23]. Esmaeeli and Tryggvason [24, 25] eliminated the iterative algorithm by setting the interface temperature as the saturation temperature at the system pressure. Koynov et al. [26] performed simulations of a single bubble and bubble swarms rising due to buoyancy including mass transfer and chemical reactions at different operating conditions. Aboulhasanzadeh et al. [27] have recently developed a multiscale approach to compute the mass transfer from buoyant bubbles using a boundary-layer approximation next to the bubble. This approach greatly reduced the overall grid resolution requirement. The front tracking method has mostly been applied to film boiling [22, 25, 28] and solidification [29, 30, 31, 32]; the phase change being driven solely by the temperature gradient. To the best of our knowledge, the species gradient driven phase-change process has not been studied in the front-tracking framework. A part of this thesis describes in detail the implementation of both the temperature and

species gradient driven phase change processes and discusses about the validation and general results.

The evaporation and combustion of droplets in fuel sprays have been the area of immense interest for decades due to its industrial and defense importance. Researchers have mostly tackled this problem by studying the evaporation and combustion of a single droplet system as a base case and a first step towards the understanding of the overall phenomena [33]. One of the very first studies about droplet evaporation dates back in 1940s when Kobayashi [34] performed numerical calculations for a single droplet evaporation in air at high temperatures. He assumed constant Nusselt number at the droplet surface and showed that the results compare well with his experiments. The pioneering study about the fuel droplet combustion was performed in early 1950s by Godsave [35]. He examined a burning droplet suspended at the tip of a fine quartz fiber and interpretted his results successfully based on the assumption that the rate of burning is not controlled by the chemical reaction rates. This assumption greatly simplified the analytical treatment of the combustion of the fuel droplets. Spalding [36] performed detailed experiments to show that the transfer or diffusion of mass and energy of the fuel vapor should be one of the controlling factors for the combustion process. The validity of their assumptions were critically analyzed in the later studies by numerous authors [37, 38, 39, 40, 41, 42, 43] and various advanced evaporation models were proposed [44, 45, 46]. Following these landmark studies about evaporation and combustion of droplets, the vaporization of single/multiple water, alkane and alcohol droplets have been studied experimentally by various researchers under normal or microgravity conditions [47, 48, 49, 50, 51]. They observed the effects of ambient pressure and temperature, convective currents and droplet size on the droplet equilibrium temperature, diameter history, evaporation rate, and drag coefficient. Using these experimental results as validation base cases, various numerical studies have been performed for the evaporation and burning of fuel droplets. Miller et al. [52] numerically evaluated different droplet evaporation models through comparisons with experiments. They observed that if properties of both the gas and

vapor phases are calculated at either the wet-bulb or boiling temperature then the constant properties assumption can be safely used throughout each simulation. The numerical studies for the evaporation and burning of n-heptane [53, 54, 55, 56, 57], decane [51, 58] and methanol [59, 60] droplets have been performed under various operating conditions as a first step towards the simulation of spray combustion in engine like environment. Some of the above mentioned studies are performed using detailed transport model, detailed chemical kinetics and variable thermodynamic properties [54, 55, 56, 59] while others assume an overall single-step irreversible reaction, constant thermodynamic properties, constant Lewis numbers and ideal gas behaviour [51, 57, 58, 60]. It is argued that these simplifying assumptions are well justified to test the numerical aspects during algorithm design and code development.

1.2 Contribution and Composition of Thesis

A front-tracking method is developed for the direct numerical simulation of evaporation and burning processes in a liquid-gas multiphase system [61]. A one-field formulation is used to solve the governing equations in the framework of the finite-difference/front-tracking method on a fixed, uniform Cartesian grid, with suitable jump conditions at the interface. Both phases are assumed to be incompressible; however, the divergence-free velocity field condition is modified to account for the phase-change/mass transfer at the interface. Both temperature and species gradient driven phase-change processes are simulated in 2D planar setting.

Temperature gradient driven phase change model is validated using the two benchmark cases: The Stefan and the sucking interface problems. The numerical results of the interface location, temperature profile, velocity field and pressure jump across the interface show excellent agreement with the analytical results. The variation of the normalized squared-diameter (d^2) follows the analytical profile for various Stefan numbers. The method is also applied to simulate highly deformed moving and evaporating droplets falling under the gravitational acceleration.

For the species gradient driven phase change model, the Clausius-Clapeyron equi-

librium relation is used to find the vapor mass fraction and subsequently the evaporation mass flux at the interface. Two strategies are compared for implementing the species mass fraction boundary condition at the interface. The one that adds the evaporation mass flux as a source term to the species equation, following the adsorption layer concept developed by Muradoglu and Tryggvason [62, 63] for treating soluble surfactant, is easy to implement, is numerically efficient and yields better results as compared to the one that imposes the species mass fraction at the interface directly as the boundary condition [64, 65]. First, a simplified test case is simulated for which analytical solution is available for the evaporation mass flux. Numerical results agree very well with the analytical solution for various values of interface temperature boundary condition. It is shown that the model predicts the correct values of equilibrium wet bulb temperatures for a water droplet evaporating in the air for various combinations of dry bulb temperature and relative humidity. These results ensure the correct coupling of the Clausius-Clapeyron relation with the solution of the flow, energy and species conservation equations. The model is then applied to simulate the evaporation of a single and two droplets systems that move, evaporate, interact and undergo significant deformation in a gravitational field. The method has been demonstrated to be grid convergent and the global mass conservation is satisfied for all the above studied cases.

A temperature gradient based axisymmetric phase change solver is then developed and validated against the classic d^2 law and the experimental results of n-heptane droplet evaporation [50]. Present numerical results show a good agreement with the analytical [66], experimental [50] and the previous numerical results [53]. The phase change solver is then extended to incorporate the burning process following the evaporation/vaporization as a first step towards the development of a computational framework for direct numerical simulations of spray combustion. The chemical kinetics in the gas phase is handled using the CHEMKIN package [67, 68]. We used a single step chemistry as well as reduced chemical kinetic mechanism, constant thermodynamics properties, unity Lewis number and an ideal gas behaviour in the gas

phase. An operator-splitting approach [69, 70, 71, 72] is used to advance temperature and species mass fractions in time. We need a heat source to artificially raise the temperature locally near the droplet to ignite the fuel vapors. Once the fuel is ignited the combustion proceeds in a smooth fashion maintaining the sperical symmetry of the flame. The validation tests are performed for a burning n-heptane droplet by comparing the time histories of normalized d^2, gasification rate, peak temperatures and the ignition delay times with the previous numerical results [54, 55, 73]. The initial flame diameter and the profile of flame standoff ratio also verify our numerical results qualitatively.

The rest of this thesis is composed as follows: Chapter 2 describes the mathematical formulation of the phase change phenomenon in a liquid-gas multiphase system. A one-field formulation of the governing equations and associated jump conditions are explained. In Chapter 3, strategies are described for the solution of governing equations and their numerical implementation for 2D planar setting in the framework of front tracking method. In Chapter 4, results are presented for both the temperature and species gradient based phase change processes in 2D planar configuration. Detailed discussions are made about the results of validation cases and gravity driven single/multiple deformable evaporating droplet systems. In Chapter 5, mathematical and numerical details are presented and validation tests are performed for the direct numerical simulation of evaporation and combustion of a n-heptane droplet in axisymmerric configuration. Finally, conclusions are drawn in Chapter 6.

Chapter 2

MATHEMATICAL FORMULATION

This chapter describes, in a broader sense, the mathematical formulation of the phase change process in a multiphase system. The modeling details specific to the axisymmetric configuration and the combustion process are explained in the relevant chapters. Consider a liquid-gas multiphase system; both of which are assumed to be incompressible. Fluid flow in each phase is governed by the Navier-Stokes equations. We can write a single set of governing equations applicable to the whole domain as long as the jumps in the property fields are properly handled across the interface and surface tension effects are taken into account appropriately. Then the momentum conservation equations can be written for the entire computational domain as

$$\frac{\partial \rho \mathbf{u}}{\partial t} + \nabla \cdot (\rho \mathbf{u}\mathbf{u}) = -\nabla p + \rho \mathbf{g} + \nabla \cdot \mu(\nabla \mathbf{u} + \nabla \mathbf{u}^T) + \int_A \sigma \kappa \mathbf{n} \delta(\mathbf{x} - \mathbf{x}_\Gamma) dA, \quad (2.1)$$

where $\mathbf{u}$ and $\mathbf{g}$ are the velocity and the gravitational acceleration vectors, respectively, p is the pressure, t is time and ρ and μ are the discontinuous density and viscosity fields, respectively. The last term on the right hand side represents the body force due to the surface tension, where σ is the surface tension coefficient, κ is twice the mean curvature, and $\mathbf{n}$ is a unit vector normal to the interface. The surface tension acts only on the interface as indicated by the three-dimensional delta function δ whose arguments $\mathbf{x}$ and $\mathbf{x}_\Gamma$ are the point at which the equation is being evaluated and a point at the interface, respectively.

For a multiphase flow without phase change, the continuity equation satisfies the incompressibility condition throughout the domain, i.e., $\nabla \cdot \mathbf{u} = 0$. However, for the phase change problem, the divergence-free velocity field condition is modified at the interface to account for the phase-change/mass-transfer, so the continuity equation

becomes

$$\nabla \cdot \mathbf{u} = \frac{1}{h_{lg}} \left(\frac{1}{\rho_g} - \frac{1}{\rho_l} \right) \int_A \delta(\mathbf{x} - \mathbf{x}_\Gamma) \dot{q_\Gamma} dA_\Gamma. \tag{2.2}$$

The delta function makes the above equation non-zero at the interface and zero elsewhere. In Eq. (2.2), h_{lg} is the latent heat of vaporization and $\dot{q_\Gamma}$ represents the heat flux per unit time at the interface. Subscripts Γ, l and g represent the interface, the liquid and gas phases of a multiphase system, respectively. The mass and momentum jump conditions at the interface are:

$$\rho_l(\mathbf{u}_l - \mathbf{u}_\Gamma) \cdot \mathbf{n} \;=\; \rho_g(\mathbf{u}_g - \mathbf{u}_\Gamma) \cdot \mathbf{n} = \dot{m_\Gamma}, \tag{2.3}$$

$$\dot{m_\Gamma}(\mathbf{u}_g - \mathbf{u}_l) \;=\; (\boldsymbol{\tau}_g - \boldsymbol{\tau}_l) \cdot \mathbf{n} - (p_g - p_l)\mathbf{I} \cdot \mathbf{n} + \sigma\kappa\mathbf{n}, \tag{2.4}$$

where $\dot{m_\Gamma}$ is the mass flux per unit time across the interface, $\boldsymbol{\tau}$ is the stress tensor and $\mathbf{I}$ is the identity tensor. Note that the Marangoni effects are not considered in this study but can easily be incorporated into the present numerical method [74]. The energy equation is solved in the whole domain and is given by

$$\frac{\partial \rho c_p T}{\partial t} + \nabla \cdot \rho c_p T \mathbf{u} = \nabla \cdot k \nabla T - \Lambda \int_A \delta(\mathbf{x} - \mathbf{x}_\Gamma) \dot{q_\Gamma} dA_\Gamma, \tag{2.5}$$

where T is the temperature, c_p is the specific heat at constant pressure and k is the thermal conductivity. Subscript *sat* denotes the saturation value of the variable. The last term in the above equation incorporates the thermal effects of phase change into the energy equation where the coefficient $\Lambda = (1 - (c_{p,g} - c_{p,l})T_{sat}/h_{lg})$ is a constant which modifies the latent heat h_{lg} due to unequal specific heats of the liquid and gas phases. The convection-diffusion equation for the species evolution in space and time reads as:

$$\frac{\partial \rho Y_\alpha}{\partial t} + \nabla \cdot \rho Y_\alpha \mathbf{u} = \nabla \cdot \rho D_\alpha \nabla Y_\alpha \qquad \alpha = 1, 2, ..., n_s \,, \tag{2.6}$$

where Y_α and D_α represent the mass fraction and mass diffusion coefficient of species component α, respectively. The energy and species jump conditions must be satisfied to ensure the energy and mass conservation across the interface. These are:

$$\dot{m_\Gamma} h_{lg} = \dot{q_\Gamma} = k_g \left. \frac{\partial T}{\partial n} \right|_g - k_l \left. \frac{\partial T}{\partial n} \right|_l, \tag{2.7}$$

$$\dot{m}_\Gamma Y_l^\Gamma - \dot{m}_\Gamma Y_g^\Gamma + \rho_g D_\alpha \left.\frac{\partial Y}{\partial n}\right|_\Gamma = 0. \tag{2.8}$$

For a mono-component liquid droplet, $Y_l^\Gamma = 1$ and gradients of the species mass fraction are zero. Thus Eq. (2.8) takes the form:

$$\dot{m}_\Gamma = \frac{\rho_g D_\alpha \left.\frac{\partial Y_{vap}}{\partial n}\right|_\Gamma^g}{1 - Y_{vap}^\Gamma}. \tag{2.9}$$

The vapor mass fraction at the interface, Y_{vap}^Γ, is calculated using the Clausius-Clapeyron relation, i.e.,

$$p_{vap}^\Gamma = p_{atm} \exp\left\{-\frac{h_{lg} m_{vap}}{R}\left(\frac{1}{T^\Gamma} - \frac{1}{T^B}\right)\right\}, \tag{2.10}$$

$$Y_{vap}^\Gamma = \frac{p_{vap}^\Gamma m_{vap}}{(p_{atm} - p_{vap}^\Gamma) m_g + p_{vap}^\Gamma m_{vap}}, \tag{2.11}$$

where p_{vap}^Γ is the saturated vapor pressure corresponding to the interface temperature T^Γ, T^B is the liquid boiling temperature at the ambient pressure conditions, i.e., at $p = p_{atm}$, R is the perfect gas constant, and m_{vap} and m_g are the molar masses of the vapor and gas, respectively.

We also assume that the material properties remain constant following a fluid particle, i.e.,

$$\frac{D\rho}{Dt} = 0; \quad \frac{D\mu}{Dt} = 0; \quad \frac{Dk}{Dt} = 0; \quad \frac{Dc_p}{Dt} = 0; \quad \frac{DD_\alpha}{Dt} = 0, \tag{2.12}$$

where $\frac{D}{Dt} = \frac{\partial}{\partial t} + \mathbf{u} \cdot \nabla$ is the material derivative. The relevant non-dimensional parameters for this study can be expressed as

$$\begin{aligned} \gamma &= \frac{\rho_l}{\rho_g}; \quad \zeta = \frac{\mu_l}{\mu_g}; \quad Sc = \frac{\mu_g}{\rho_g D}; \quad Pr = \frac{\mu c_p}{k}; \\ Re &= \frac{\rho_g u_s l_s}{\mu_g}; \quad St = \frac{c_{p,g}\left(T_\infty - T_{sat}\right)}{h_{lg}}, \end{aligned} \tag{2.13}$$

where γ and ζ represent the density and the viscosity ratios, respectively. Sc, Pr, Re and St are the Schmidt number, Prandtl number, Reynolds number and Stefan numbers, respectively. u_s and l_s are appropriately selected velocity and length scales, respectively, and $t_s = l_s/u_s$ be the time scale.

Chapter 3

NUMERICAL METHOD

The governing equations for the flow (Eqs. (2.1)-(2.2)), energy (Eq. (2.5)) and species mass fraction (Eq. (2.6)) fields are solved in a coupled form on a fixed, uniform, staggered MAC grid using a finite-difference/front-tracking method [10, 11, 22, 25, 75]. The spatial derivatives in the momentum equations are discretized using a second-order central difference scheme, whereas, the time integration is performed using a first-order projection method [76]. The solution of the energy and the species equations is advanced in time using a first order explicit Euler method. All spatial derivatives in the energy and species equations are approximated using second-order central differences except for the convective terms where a $5th$ order WENO-Z [77] scheme is used. The pressure, temperature, species mass fractions and all material properties are stored at the cell centers, whereas, the velocity components are stored at the cell face centers on an Eulerian grid as shown in Fig. 3.1(b). The time integration of energy and species equations is slightly modified when combustion process is also considered. The relevant numerical details are presented in Chapter 5.

The interface or front, separating different phases, is made up of connected marker points and is tracked explicitly [10, 11, 75]. Each marker point moves with the local flow velocity, in addition to the velocity due to phase change, Eqs. (3.3)-(3.4). The piece of the interface between two adjacent marker points is called a front element. The schematic representation of the Lagrangian grid on the background fixed mesh is shown in Fig. 3.1(a). The Indicator function $I(\mathbf{x}, t)$ tracks the liquid and the gas phases both in space and time and is defined as:

$$I(\mathbf{x}, t) = \begin{cases} 1 & \text{in droplet phase,} \\ 0 & \text{in bulk phase.} \end{cases} \tag{3.1}$$

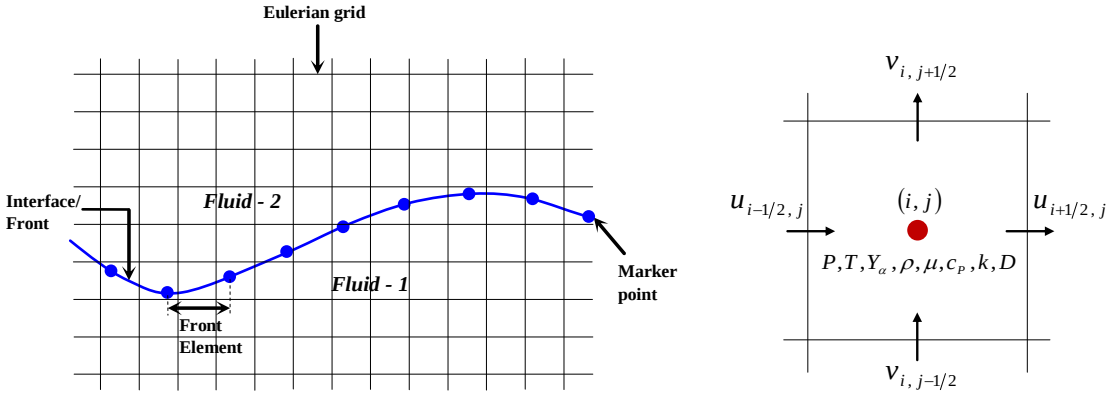

(a) (b)

Figure 3.1: (a) The schematic illustration of a Lagrangian grid on an Eulerian background mesh. (b) The staggered grid used in the numerical solution of the governing equations.

The indicator function $I(\mathbf{x},t)$ is computed at each time step using the standard procedure described by Tryggvason et al. [11], which involves the solution of a separable Poisson equation. Then the material property fields are updated at each time step as a function of $I(\mathbf{x},t)$

$$\begin{aligned}
\rho &= \rho_l I(\mathbf{x},t) + \rho_g(1-I(\mathbf{x},t)); \qquad \mu = \mu_l I(\mathbf{x},t) + \mu_g(1-I(\mathbf{x},t));\\
k &= k_l I(\mathbf{x},t) + k_g(1-I(\mathbf{x},t)); \qquad \rho c_p = \rho_l c_{p,l} I(\mathbf{x},t) + \rho_g c_{p,g}(1-I(\mathbf{x},t));\\
D_\alpha &= D_{\alpha,g}(1-I(\mathbf{x},t)).
\end{aligned} \tag{3.2}$$

Information needs to be communicated between the fixed grid and the moving interface during the solution process. For example, the surface tension as well as the heat and mass fluxes are first calculated at the interface and then smoothed onto the fixed Eulerian grid while solving momentum, energy and species equations, respectively. Similarly, the velocity field is only available at the fixed Eulerian grid nodes and needs to be interpolated onto the marker points for moving the interface. A complete description of the smoothing and interpolation procedure can be found in the review paper and the recent book by Tryggvason et al. [11, 75]. We have introduced some modifications in the standard procedure for handling certain quantities which

are discussed in the relevant sections. Also, to keep the front resolution within the prescribed limits, front restructuring is necessary. The element addition and deletion is performed using a third-order Legendre polynomial fit to preserve interface curvature during the restructuring [11].

The interface location is updated at each time step by moving the individual marker points; the velocity of each marker point comprises of the local flow velocity and the velocity of vaporization, i.e.,

$$\frac{d\mathbf{x}_\Gamma}{dt} = u_n \mathbf{n}_\Gamma, \tag{3.3}$$

where

$$u_n = \frac{1}{2}(\mathbf{u}_l + \mathbf{u}_g) \cdot \mathbf{n} - \frac{\dot{q_\Gamma}}{2h_{lg}} \left(\frac{1}{\rho_l} + \frac{1}{\rho_g} \right). \tag{3.4}$$

Further details of the front-tracking method are available in a paper by Unverdi and Tryggvason [10] and a review by Tryggvason et al. [11].

3.1 Flow Solver

The flow equations are solved on an Eulerian grid using the projection method developed by Chorin [76]. It is a predictor-corrector type method in which we first predict the temporary velocity field by ignoring the pressure effects, and in the second step, the predicted velocity field is corrected to satisfy the continuity equation, Eq. (2.2). The momentum equations can be written in the form:

$$\frac{\rho^{n+1}\mathbf{u}^{n+1} - \rho^n \mathbf{u}^n}{\Delta t} = \mathbf{A}^n - \nabla p, \tag{3.5}$$

where $\mathbf{A}$ represents the advection, the diffusion, the gravitational and the surface tension force terms and the superscript n indicates the current time level. The projection method splits the above equation as

$$\frac{\rho^{n+1}\mathbf{u}^{*} - \rho^n \mathbf{u}^n}{\Delta t} = \mathbf{A}^n, \tag{3.6}$$

$$\frac{\rho^{n+1}\mathbf{u}^{n+1} - \rho^{n+1} \mathbf{u}^{*}}{\Delta t} = -\nabla p, \tag{3.7}$$

where $\mathbf{u}^*$ is the unprojected velocity field, calculated using Eq. (3.6), by ignoring the pressure effects. Next, we take divergence of Eq. (3.7) to obtain a Poisson equation for the pressure, i.e.,

$$\nabla \cdot \frac{1}{\rho^{n+1}} \nabla p = \frac{\nabla \cdot \mathbf{u}^* - \nabla \cdot \mathbf{u}^{n+1}}{\Delta t}. \tag{3.8}$$

For $\nabla \cdot \mathbf{u}^{n+1}$, we use Eq. (2.2) as

$$\nabla \cdot \mathbf{u}^{n+1} = \frac{1}{h_{lg}} \left(\frac{1}{\rho_g} - \frac{1}{\rho_l} \right) \left[\int_A \delta(\mathbf{x} - \mathbf{x}_\Gamma) \dot{q}_\Gamma dA_\Gamma \right]^{n+1}, \tag{3.9}$$

where $\dot{q}_\Gamma$ is computed at $(n+1)$ time level, i.e., using the front position at $(n+1)$. We substitute Eq. (3.9) into Eq. (3.8) and solve the resulting Poisson equation for pressure iteratively using a Red-Black Gauss-Seidel method with a Successive Over Relaxation (SOR). In the axisymmetric setting, we use multigrid method [78] to solve the Poisson equation for pressure. Once $\mathbf{u}^*$ and p are known, the velocity field at the next time level, $n+1$, is found using Eq. (3.7) as:

$$\mathbf{u}^{n+1} = \mathbf{u}^* - \frac{\Delta t}{\rho^{n+1}} \nabla p. \tag{3.10}$$

The above algorithm is first order accurate in time. However, it can easily be extended for the second-order accuracy using a predictor corrector scheme as described by Tryggvason et al. [11, 25].

3.2 Temperature Gradient Based Evaporation Model

In this model, it is assumed that the interface temperature T^Γ is the same as the saturation temperature T_{sat}, since pressure fluctuations in the system are small as compared to the absolute pressure. Thus the energy jump condition, Eq. (2.7), is used to calculate the heat flux per unit time at the interface, and is rewritten here for the kth marker point as

$$\dot{q}_{\Gamma_k} = k_g \left. \frac{\partial T}{\partial n} \right|_g^{\Gamma_k} - k_l \left. \frac{\partial T}{\partial n} \right|_l^{\Gamma_k}, \tag{3.11}$$

where Γ_k represents the kth marker point of the interface. A first-order one-sided finite difference discretization of Eq. (3.11) yields [25, 79]

$$\dot{q}_{\Gamma_k} = \frac{1}{\eta h}[k_g(T_g - T_{sat}) - k_l(T_{sat} - T_l)], \tag{3.12}$$

where T_g and T_l are the temperatures approximated at points (x^+, y^+) and (x^-, y^-), in the gas and the liquid domains, respectively, using a bi-linear interpolation, as shown in Fig. 3.2(a). These points are at a distance ηh, normal from the kth marker

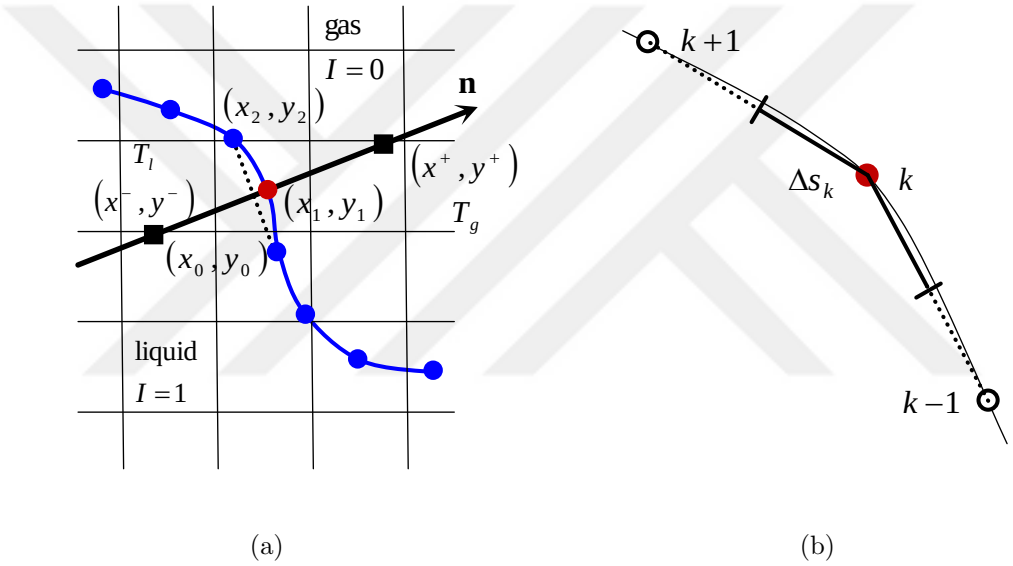

(a) (b)

Figure 3.2: (a) The method used to approximate the temperature gradients at the interface. (b) Computation of the interface length Δs_k corresponding to the k^{th} marker point.

point (x_1, y_1). In Eq. (3.12), h is the uniform grid spacing and η scales the length of the probe and can be selected between 1 - 2 without any significant effect on the results [24, 25, 30]. Once $\dot{q}_{\Gamma_k}$ is found, the last term of the energy equation, Eq. (2.5), is computed first and then smoothed onto the neighbouring fixed grid nodes in a conservative manner. Following Tryggvason et al. [11, 75], for smoothing an interface quantity, say ϕ_Γ, onto fixed grid node (i, j) in two-dimensions, we must have

$$\int_{\Delta s} \phi_\Gamma(s)\, ds \;=\; \int_{\Delta A} \phi_{i,j}(\mathbf{x})\, dA, \tag{3.13}$$

which is approximated for a 2D planar case as

$$\phi_{i,j} = \sum_k \phi_\Gamma^k w_{i,j}^k \frac{\Delta s_k}{h^2}, \tag{3.14}$$

where Δs_k is the length of the piece of the interface between the centers of the front elements sharing the kth marker point and is calculated as shown by the thick lines in Fig. 3.2(b); and $w_{i,j}^k$ is the weight of the fixed grid node (i, j) corresponding to the kth marker point and is calculated using the Peskin's cosine function [80]. The weights must also satisfy the consistency condition

$$\sum_{i,j} w_{i,j}^k = 1. \tag{3.15}$$

Next, for the species field, we need $\dot{m}_{\Gamma_k}$, which can be computed as,

$$\dot{m}_{\Gamma_k} = \frac{\dot{q}_{\Gamma_k}}{h_{lg}}. \tag{3.16}$$

3.3 Species Gradient Based Evaporation Model

In this model, it is assumed that species concentration gradient at the interface is the only driving force for the phase change. The species mass fraction at the interface and consequently the evaporative mass flux is computed using the Clausius-Clapeyron relation. For the kth marker point of the interface, the evaporative mass flux per unit time ($\dot{m}_{\Gamma_k}$) is computed using Eq. (2.9) as

$$\dot{m}_{\Gamma_k} = \frac{\rho_g D_\alpha \left.\frac{\partial Y}{\partial n}\right|_{\Gamma_k}^g}{1 - Y_{vap}^{\Gamma_k}}, \tag{3.17}$$

where $Y_{vap}^{\Gamma_k}$ is obtained from the Clausius-Clapeyron relation, i.e., Eqs. (2.10) - (2.11). The species gradient in the gas phase, normal to the interface, is calculated following the same procedure as discussed for the temperature gradient (see Fig. 3.2(a)). Corresponding to each marker point, we find a point (x^+, y^+) in the gas phase, at a distance ηh normal from the marker point. The species mass fraction, Y^+, is approximated at (x^+, y^+) using a bi-linear interpolation. The species gradient is then calculated using a first-order one-sided finite difference approximation as

$$\left.\frac{\partial Y}{\partial n}\right|_{\Gamma_k}^g = \frac{1}{\eta h}(Y_{vap}^{\Gamma_k} - Y^+)\,. \tag{3.18}$$

To solve the governing equation for the species mass fraction, the vapor mass fraction at the interface Y_{vap}^{Γ} may be applied directly as the boundary condition [64, 65] or the mass flux per unit time $\dot{m}_{\Gamma_k}$ can be distributed in a conservative manner onto a thin layer just outside the liquid droplet [62, 63] and then added as a source term to the species equation, Eq. (2.6). Both the strategies are briefly described below.

3.3.1 Interface Mass Fraction as the Dirichlet Boundary Condition

In this case, the interface mass fraction, $Y_{vap}^{\Gamma_k}$, is applied as the Dirichlet boundary condition. The first step is to identify the grid cells which contain interface in their immediate vicinity. An algorithm is devised to find the interface cells based on the indicator function I, which defines interface as $I = 0.5$. An array is defined to store interface cells coordinates and is updated at each time step.

The discretization of convective and diffusive terms of the species equation, Eq. (2.6), is modified in the interface cells to incorporate $Y_{vap}^{\Gamma_k}$ as the boundary condition. Figure 3.3 shows one of the several irregular stencil configurations that may arise depending on the interface location. The convective term is approximated using a

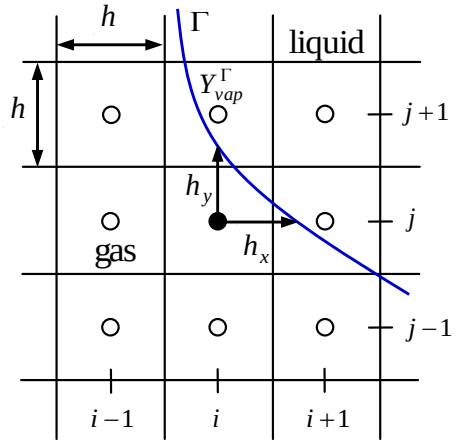

Figure 3.3: Schematic illustration of an interface cell (i, j) showing the nomenclature.

first-order upwind scheme [65]. A second order central difference discretization of the diffusion term for the interface cell (i, j) in Fig. 3.3 can be written as

$$(D_\alpha \nabla \cdot \nabla Y)_{i,j} = D_{\alpha(i,j)} \left(\frac{\partial^2 Y}{\partial x^2} + \frac{\partial^2 Y}{\partial y^2} \right)_{i,j}, \tag{3.19}$$

$$\begin{aligned} = \; D_{\alpha(i,j)} \Bigg\{ & \left(\frac{2Y_{i-1,j}}{h(h+h_x)} - \frac{2Y_{i,j}}{h(h_x)} + \frac{2Y^{\Gamma}_{vap}}{h_x(h+h_x)} \right) \\ & + \left(\frac{2Y_{i,j-1}}{h(h+h_y)} - \frac{2Y_{i,j}}{h(h_y)} + \frac{2Y^{\Gamma}_{vap}}{h_y(h+h_y)} \right) \Bigg\}, \end{aligned} \tag{3.20}$$

where h is the uniform grid size; h_x and h_y are the distances between cell center (i, j) and the interface in x and y directions, respectively. In the rest of the domain, discretization of the species equation is fairly straight forward.

3.3.2 Evaporation Mass Flux as a Source Term

Instead of applying $Y^{\Gamma_k}_{vap}$ as the Dirichlet boundary condition, the evaporation mass flux per unit time, $\dot{m}_{\Gamma_k}$, found using Eq. (3.17), is distributed as a species source, $\dot{S}_\alpha$, onto the adjacent fixed grid nodes, just outside the interface, in a conservative manner. The conventional symmetric and the modified one-sided distribution stencils are schematically depicted in Figs. 3.4(a) and 3.4(b), respectively. This approach is similar and closely related to the adsorption layer concept developed by Muradoglu and Tryggvason [62, 63] for the treatment of mass exchange between the interface and bulk fluid in the simulation of soluble surfactant in multiphase flows. The species equation, Eq. (2.6), is thus modified to account for the evaporative mass transfer as a source term

$$\frac{\partial \rho Y_\alpha}{\partial t} + \nabla \cdot \rho Y_\alpha \mathbf{u} = \nabla \cdot \rho D_\alpha \nabla Y_\alpha + \dot{S}_\alpha \qquad \alpha = 1, 2, ..., n_s \,. \tag{3.21}$$

The source term $\dot{S}_{\alpha_{i,j}}$ at grid node (i, j) is approximated as [11, 75]

$$\dot{S}_{\alpha_{i,j}} = \sum_k \dot{m}_{\Gamma_k} w^k_{i,j} \frac{\Delta s_k}{h^2}, \tag{3.22}$$

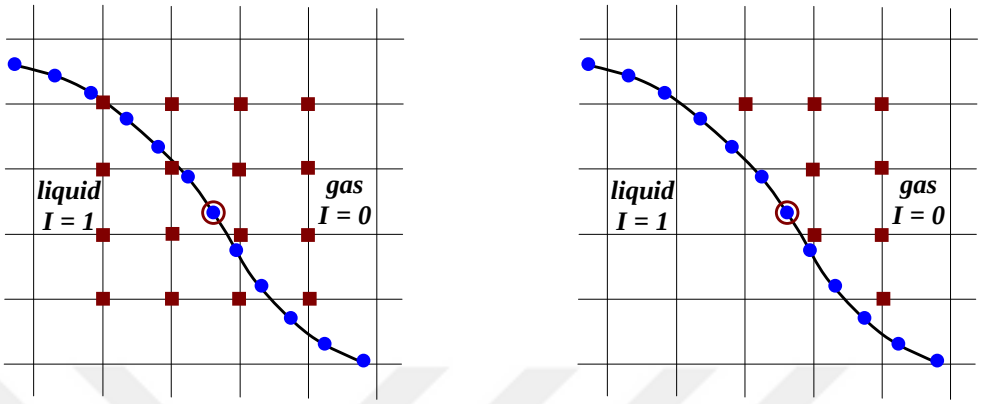

(a) The conventional symmetric distribution stencil.

(b) The modified one-sided distribution stencil.

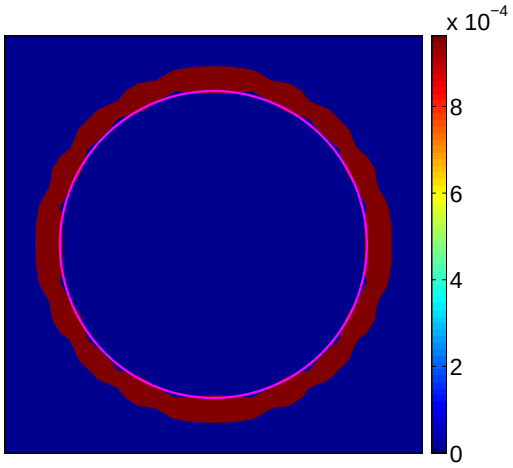

(c) Evaporative mass source distributed outside the droplet.

Figure 3.4: Treatment of the evaporation mass flux per unit time $\dot{m}_{\Gamma_k}$ as a source term: schematic plot showing (a) the standard symmetric distribution stencil and (b) its modified version. Subfigure (c) is the contour plot of vapor mass fraction showing the distribution of $\dot{m}_{\Gamma_k}$ onto the fixed Eulerian grid using modified strategy for a static evaporating droplet case; the convective and diffusive terms of species equation are switched off to better explain the scenario.

where $\dot{m}_{\Gamma_k}$ is evaporation mass flux per unit time computed at the kth marker point, Δs_k is the length of the interface corresponding to the kth marker point (see Fig. 3.2(b)), h is the uniform grid spacing and $w^k_{i,j}$ is the weight of grid point (i, j) corresponding to the kth marker point. The weight should satisfy the consistency condition in order to conserve the total source strength in going from the interface to the grid, i.e.,

$$\sum_i \sum_j w^k_{i,j} = 1. \tag{3.23}$$

The weight for the grid node (i, j), for smoothing a quantity from the kth marker point, can be written as

$$w^k_{i,j} = \frac{\tilde{w}^k_{i,j}}{\sum_i \sum_j \tilde{w}^k_{i,j}}. \tag{3.24}$$

The non-normalized weight is obtained as a product of one-dimensional distribution functions, i.e.,

$$\tilde{w}^k_{i,j} = d(x_{\Gamma_k} - ih)d(y_{\Gamma_k} - jh), \tag{3.25}$$

where $(x_{\Gamma_k}, y_{\Gamma_k})$ is the coordinate of the kth marker point and the distribution function d is a slightly modified version of the Peskin's cosine function [62, 63, 80] defined as

$$d(x) = \begin{cases} \frac{1}{2\lambda}\left(1 + \cos(\frac{\pi x}{\lambda})\right) & \text{if } |x| < \lambda \text{ and } I < 0.5, \\ 0 & \text{otherwise,} \end{cases} \tag{3.26}$$

where λ is the width of the layer onto which $\dot{m}_{\Gamma_k}$ is distributed as a mass source, and is selected as $\lambda = 2h$ in the present study. We also checked for $\lambda = 3h$ but no considerable effect on the output parameters is observed. Fig. 3.4(c) shows the sample contour plot of the species mass source smoothed onto the fixed grid following the above strategy, i.e., $I < 0.5$.

Chapter 4

EVAPORATIVE PHASE CHANGE IN 2D PLANAR CONFIGURATION[1]

For 2D planar configuration, the momentum conservation equations for u and v velocity components in the x and y coordinate directions, respectively, can be written in conservative form as

$$\begin{aligned}\frac{\partial \rho u}{\partial t}+\frac{\partial \rho u^2}{\partial x}+\frac{\partial \rho uv}{\partial y} &= -\frac{\partial p}{\partial x}+\Delta\rho g_x+\frac{\partial}{\partial x}\left(2\mu\frac{\partial u}{\partial x}\right)+\frac{\partial}{\partial y}\mu\left(\frac{\partial u}{\partial y}+\frac{\partial v}{\partial x}\right)\\ &\quad+\int_A \sigma\kappa\mathbf{n}\delta(\mathbf{x}-\mathbf{x}_\Gamma)dA\cdot\mathbf{i}\ , \end{aligned} \tag{4.1}$$

$$\begin{aligned}\frac{\partial \rho v}{\partial t}+\frac{\partial \rho vu}{\partial x}+\frac{\partial \rho v^2}{\partial y} &= -\frac{\partial p}{\partial y}+\Delta\rho g_y+\frac{\partial}{\partial x}\mu\left(\frac{\partial u}{\partial y}+\frac{\partial v}{\partial x}\right)+\frac{\partial}{\partial y}\left(2\mu\frac{\partial v}{\partial y}\right)\\ &\quad+\int_A \sigma\kappa\mathbf{n}\delta(\mathbf{x}-\mathbf{x}_\Gamma)dA\cdot\mathbf{j}\ , \end{aligned} \tag{4.2}$$

Similarly, the conservative form of the energy (Eq. (2.5)) and species (Eq. (2.6)) equations in 2D planar configuration reads as

$$\begin{aligned}\frac{\partial \rho c_p T}{\partial t}+\frac{\partial \rho c_p Tu}{\partial x}+\frac{\partial \rho c_p Tv}{\partial y} &= \frac{\partial}{\partial x}\left(k\frac{\partial T}{\partial x}\right)+\frac{\partial}{\partial y}\left(k\frac{\partial T}{\partial y}\right)\\ &\quad-\Lambda\int_A \delta(\mathbf{x}-\mathbf{x}_\Gamma)\dot{q_\Gamma}dA_\Gamma\ , \end{aligned} \tag{4.3}$$

$$\begin{aligned}\frac{\partial \rho Y_\alpha}{\partial t}+\frac{\partial \rho Y_\alpha u}{\partial x}+\frac{\partial \rho Y_\alpha v}{\partial y} &= \frac{\partial}{\partial x}\left(\rho D_\alpha\frac{\partial Y_\alpha}{\partial x}\right)+\frac{\partial}{\partial y}\left(\rho D_\alpha\frac{\partial Y_\alpha}{\partial y}\right)\\ &\quad+\dot{S}_\alpha \qquad\qquad \alpha=1,2,...,n_s\ , \end{aligned} \tag{4.4}$$

[1]PUBLISHED AS: M. IRFAN AND M. MURADOGLU, A FRONT TRACKING METHOD FOR DIRECT NUMERICAL SIMULATION OF EVAPORATION PROCESS IN A MULTIPHASE SYSTEM, JOURNAL OF COMPUTATIONAL PHYSICS, 337, 132 - 153 (2017).

The numerical recipes used to discretize and solve the above governing equations are explained in Chapter 3. In the present study, only one species is considered, the vapor, but the method can be extended to include many species straightforwardly. The species equation is solved only for the vapor phase in the gas domain, outside the liquid droplet. We used the strategy discussed in section 3.3.2 to implement the species mass fraction boundary condition at the interface unless otherwise stated; the last term in Eq. (4.4) represents the species mass source used in the said strategy. Validation cases are presented and comprehensive discussions are made about the results for both the temperature and species gradient based phase change processes. The methods are then applied to moving deformable evaporating droplets in the gravitational field.

4.1 Temperature Gradient Based Evaporation Model

This model simulates the evaporative multiphase systems where the temperature gradient at the interface drives the phase change, e.g., the fuel droplet evaporation and burning in the internal combustion engines.

4.1.1 Validation Test - 1: The Stefan Problem

The Stefan problem is a well-known test case to validate the phase change models [13, 15, 16, 19, 24, 25, 81]. Figure 4.1 shows the schematic of the Stefan problem used in this study. A vertical interface separates the liquid and the vapor phases. Both the phases are assumed to be incompressible and are initially at rest at the saturation temperature condition, T_{sat}. The temperature of the left wall, T_w, adjacent to the vapor phase, is increased above the saturation value. The heat flows from the wall towards the interface. At the interface, the liquid vaporizes due to the temperature gradient. The interface moves towards right due to the free flow boundary conditions applied at the right boundary. As a result, a velocity field is developed in the liquid phase. The liquid temperature, however, stays fixed at the saturation value. The vapor is assumed to remain stationary, therefore, diffusion is responsible for heat

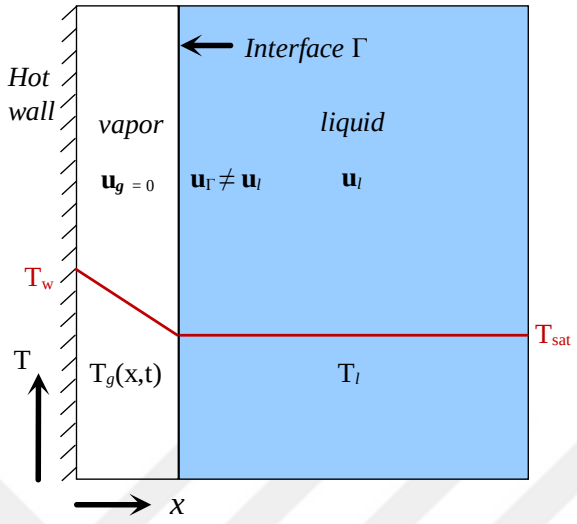

Figure 4.1: Schematic of the Stefan problem.

transfer from the wall to the interface. Hence, the energy equation needs to be solved just in the vapor phase and can be written as

$$\frac{\partial T}{\partial t} = \alpha_g \frac{\partial^2 T}{\partial x^2} \qquad 0 \leq x \leq x_\Gamma(t), \tag{4.5}$$

where T is the temperature, α_g is the thermal diffusivity of the vapor phase and $x_\Gamma(t)$ is the interface location at time t. Equation (4.5) is solved subject to the boundary conditions

$$T(x = 0, t) = T_w \ , \qquad T(x = x_\Gamma(t), t) = T_{sat} \ . \tag{4.6}$$

Heat flux per unit time at the interface, $\dot{q}_\Gamma$, is computed using the energy jump condition

$$\dot{q}_\Gamma = k_g \left. \frac{\partial T}{\partial n} \right|_g^\Gamma \ , \tag{4.7}$$

where k_g is the thermal conductivity of the vapor phase. The analytical solution for the interface location at any time t can be expressed as

$$x_\Gamma(t) = 2\beta\sqrt{\alpha_g t} \ , \tag{4.8}$$

where β is the solution of the transcendental equation

$$\beta \exp(\beta^2) \operatorname{erf}(\beta) = \frac{c_{p,g}(T_w - T_{sat})}{h_{lg}\sqrt{\pi}} \ . \tag{4.9}$$

The analytical value of temperature at any point x in the vapor domain and at any time instant t is given by the expression

$$T_g(x,t) = T_w + \left(\frac{T_{sat} - T_w}{\operatorname{erf}(\beta)}\right) \operatorname{erf}\left(\frac{x}{2\sqrt{\alpha_g t}}\right). \tag{4.10}$$

The velocity in the liquid phase can be found analytically using the following relation

$$u_l = \left(1 - \frac{\rho_g}{\rho_l}\right) u_n \ , \tag{4.11}$$

where $u_n = \beta\sqrt{\alpha_g/t}$. For a flat interface with uniform velocity field, the momentum jump condition in the normal direction, Eq. (2.4), simplifies to the following pressure jump relation

$$p_g - p_l = -\rho_g \left(1 - \frac{\rho_g}{\rho_l}\right) u_n^2. \tag{4.12}$$

The fluid properties used in this numerical test case are: $\rho_g = 0.5$, $\rho_l = 2.5$, $\mu_g = 0.007$, $\mu_l = 0.098$, $k_g = 0.0035$, $k_l = 0.0015$, $c_{p,g} = c_{p,l} = 1.0$ and $h_{lg} = 100$. Saturation temperature, T_{sat}, is set as 10 and wall temperature $T_w = 12$ to achieve the Stefan number $St = 0.02$.

We performed numerical simulations on a 1×1 domain. Results are presented for four different density ratios, i.e., $\gamma = \rho_l/\rho_g = 5$, 10, 20 and 40. Vapor phase density, ρ_g, is varied to achieve these values; the thermal diffusivity α_g is also changed as a result. For all the cases, the initial interface location is set as $x_\Gamma = 0.1$, which corresponds to different initial times $t_o(\gamma)$ depending on the density ratio (γ). The initial temperature field is specified in the vapor phase using the analytical solution, Eq. (4.10), at the initial time $t_o(\gamma)$. First, a grid convergence study is performed for density ratio $\gamma = 20$. The results for interface location and temperature profile show that a 64×64 grid resolution gives a very good match with the analytical results as shown in Fig. 4.2. Next, the numerical results of interface location, liquid phase

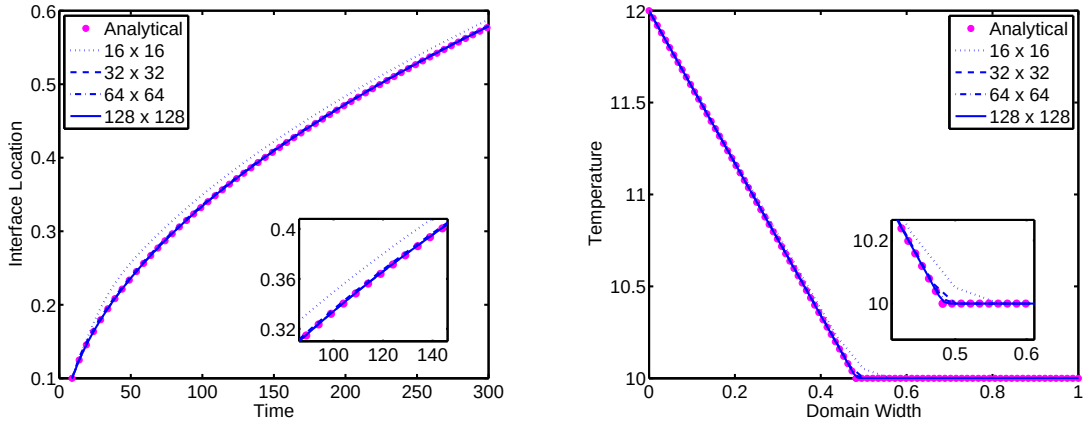

Figure 4.2: Grid convergence results for the Stefan problem for density ratio $\gamma = 20$. (Left) the evolution of the interface location, (right) the temperature profile at $t = 208.98$. The insets show the enlarged views in each plot.

velocity and pressure jump are compared with the analytical solutions for different density ratios. A very good agreement is observed for all the cases, as shown in Fig. 4.3.

4.1.2 Validation Test - 2: The Sucking Interface Problem

The sucking interface problem is also a benchmark case used to validate the temperature gradient based phase change model and has previously been studied by Welch and Wilson [13] and Guedon [81] to validate their phase change models. In this problem, a vapor layer is attached to the left wall of the domain while the rest is filled with a liquid as schematically shown in Fig. 4.4. Both phases are assumed to be incompressible and are separated by a vertical interface. The vapor phase is at saturation temperature T_{sat}, and stays at rest throughout the simulation. The liquid temperature T_∞ is higher than the saturation value, therefore, the phase change will occur at the interface. This will cause the interface to move towards right and a flow will be developed in the liquid phase. The heat of vaporization, absorbed at the interface due to phase change, comes from the liquid, which results in the formation of thermal boundary layer at the interface. A complete convection-diffusion energy

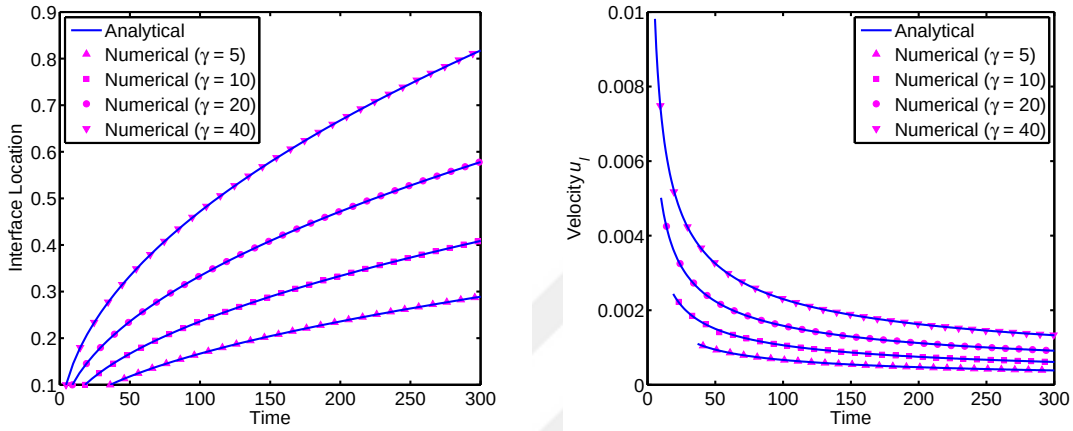

(a)

(b)

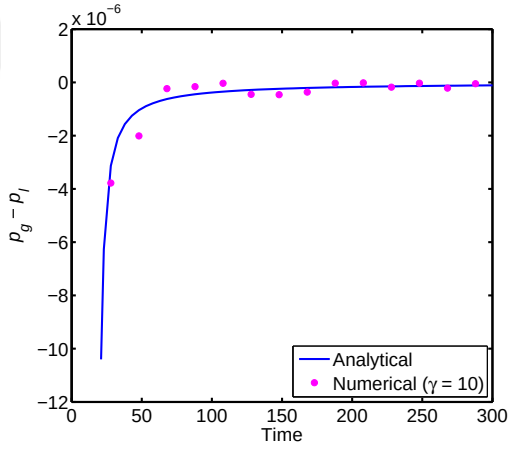

(c)

Figure 4.3: Comparison of the analytical and numerical results for the 1D Stefan problem. The evolution of (a) the interface location, (b) the liquid phase velocity, and (c) the pressure difference with time. Grid: 64×64.

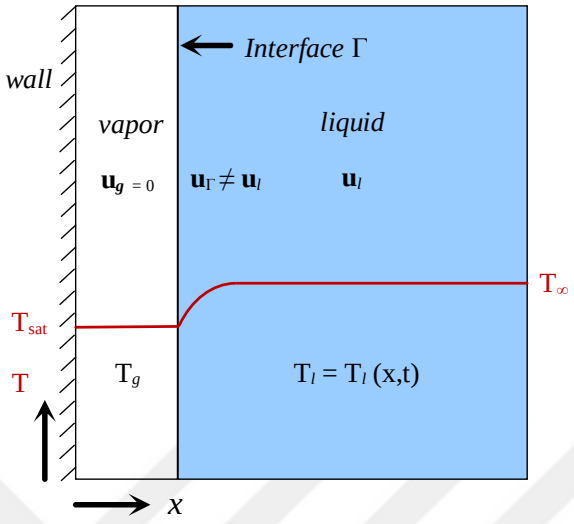

Figure 4.4: Schematic of the sucking interface problem.

equation needs to be solved in the liquid phase in the following form

$$\frac{\partial T}{\partial t} + \mathbf{u} \cdot \nabla T = \alpha_l \frac{\partial^2 T}{\partial x^2} \qquad x_\Gamma(t) \leq x \leq 1, \tag{4.13}$$

subject to the boundary condition

$$T(x \leq x_\Gamma(t), t) = T_{sat}, \tag{4.14}$$

where α_l is the thermal diffusivity of the liquid phase. Heat flux per unit time at the interface is computed using the energy jump condition given by Eq. (2.7). The sucking interface problem is a more stringent test case as compared to the Stefan problem since we also need to solve the convective term of the energy equation in addition to the diffusion term coupled with the Navier-Stoke equations. Analytical solutions are available in the literature for this test problem [13, 81]. At any time t, the interface location is calculated using the same expression as for the Stefan problem

$$x_\Gamma(t) = 2\beta\sqrt{\alpha_g t}\ ,$$

where β is the solution of the following transcendental equation

$$\exp(\beta^2)\,\mathrm{erf}(\beta)\left[\beta - \frac{(T_\infty - T_{sat})\,c_{p,g}k_l\sqrt{\alpha_g}\exp\left(-\beta^2\frac{\rho_g^2\alpha_g}{\rho_l^2\alpha_l}\right)}{h_{lg}k_g\sqrt{\pi\alpha_l}\,\mathrm{erfc}\left(\beta\frac{\rho_g\sqrt{\alpha_g}}{\rho_l\sqrt{\alpha_l}}\right)}\right] = \frac{c_{p,g}(T_w - T_{sat})}{h_{lg}\sqrt{\pi}}. \quad (4.15)$$

The analytical solution for the temperature profile in the vapor phase is given as

$$T_g(x,t) = T_w + \left(\frac{T_{sat} - T_w}{\mathrm{erf}(\beta)}\right)\mathrm{erf}\left(\frac{x}{2\sqrt{\alpha_g t}}\right). \quad (4.16)$$

The temperature profile can be found in the liquid phase analytically using the following relation

$$T_l(x,t) = T_\infty - \left[\frac{T_\infty - T_w}{\mathrm{erfc}\left(\beta\frac{\rho_g\sqrt{\alpha_g}}{\rho_l\sqrt{\alpha_l}}\right)}\right]\mathrm{erfc}\left(\frac{x}{2\sqrt{\alpha_l t}} + \frac{\beta(\rho_g - \rho_l)}{\rho_l}\sqrt{\frac{\alpha_g}{\alpha_l}}\right). \quad (4.17)$$

The horizontal velocity in the liquid phase and the pressure jump across the interface at any time t can be found analytically for this case too using the same expressions as we used for the Stefan problem, i.e., Eqs. (4.11) and (4.12), respectively.

The fluid properties considered for this numerical test case are: $\rho_g = 0.25$, $\rho_l = 2.5$, $\mu_g = 0.007$, $\mu_l = 0.098$, $k_g = 0.0035$, $k_l = 0.0015$, $c_{p,g} = c_{p,l} = 10.0$ and $h_{lg} = 100$. The saturation temperature T_{sat} is set as 10, which is also the wall temperature T_w. The liquid is superheated with $T_\infty = 12$. The simulations are performed on a 1 $\times$ 1 domain. The interface is initially placed at $x = 0.1$ which corresponds to the initial time $t_o = 24.7$. The temperature is initialized in the gas and liquid domains using the analytical solutions, Eqs. (4.16) and (4.17), respectively. Numerical and analytical results of the interface location, temperature profile, liquid phase velocity and pressure jump are compared as shown in Fig. 4.5. The comparisons clearly show that the numerical results approach the analytical solutions as the grid is refined. Also, the numerical values of pressure jump satisfies the analytical values. Hence our implementation is grid convergent, tracks the interface very well and successfully captures the pressure jump and the sharp thermal boundary layer.

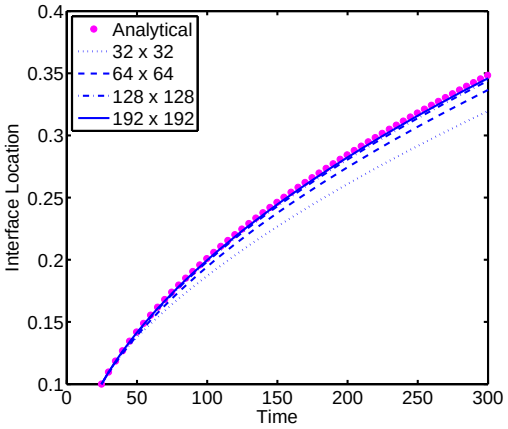

(a) The evolution of the interface location.

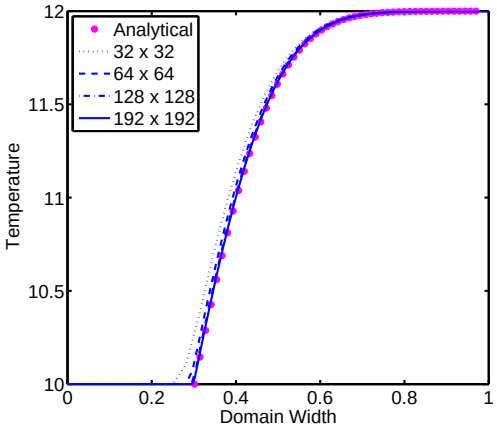

(b) Temperature profile at $t = 224.7$.

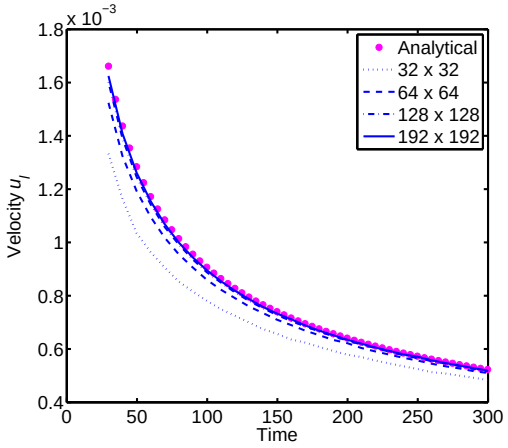

(c) The evolution of the liquid phase velocity.

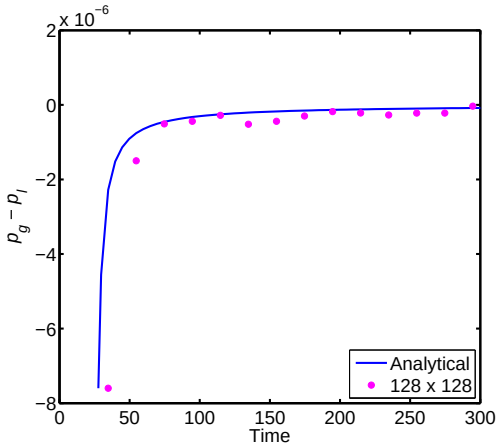

(d) The pressure jump across the interface.

Figure 4.5: Comparison of the numerical and analytical results for the sucking interface problem, $\gamma = 10$.

4.1.3 Evaporation of a 2D Static Droplet

This case simulates the evaporation of a static droplet in 2D planar configuration. l_x and l_y denote the dimensions of the domain in the x and y coordinate directions, respectively, with the origin marked at the bottom left corner as shown in Fig. 4.6. The same nomenclature is used regarding the geometric dimensions of the domain in the rest of the study. A droplet of initial diameter $d_o = 0.25$ mm is placed at the center of 1×1 mm^2 domain ($l_x = l_y$). At walls, the Dirichlet boundary condition is applied for temperature T_w; and vapors are allowed to leave the domain freely. The

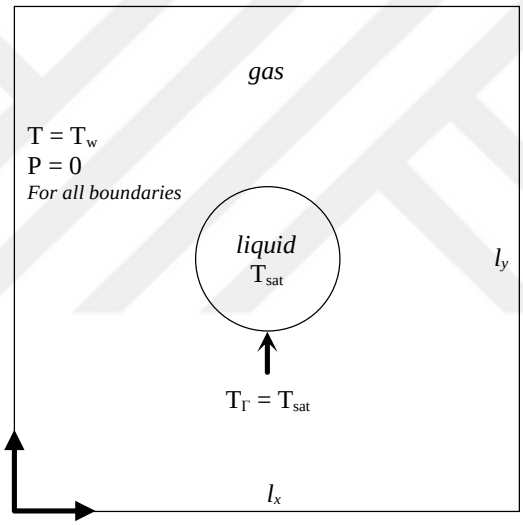

Figure 4.6: The schematic illustration of a 2D planar static droplet evaporation case.

physical properties considered here yield the non-dimensional parameters as $\gamma = 5$, $\zeta = 10$, $Pr_l = 1.75$, $Pr_g = 0.7$ and $Sc = 1.0$. The temperature inside the liquid droplet is initialized as $T_{sat} = 373$ K and approximately stays constant during the simulation, whereas the temperature in the gaseous domain is higher than T_{sat}. This temperature gradient is varied to achieve various values of Stefan number, St. The length scale l_s and time scale t_s are selected as d_o and d_o^2/α_g, respectively. Due to the temperature gradient at the interface, phase change occurs and a radially outward Stefan flow is

generated in the gas domain as shown by the velocity vector plot in Fig. 4.7. The temperature contour plot is also presented for $St = 0.05$ to show the spatial evolution of temperature in the gas domain during evaporation. The area of the droplet, and

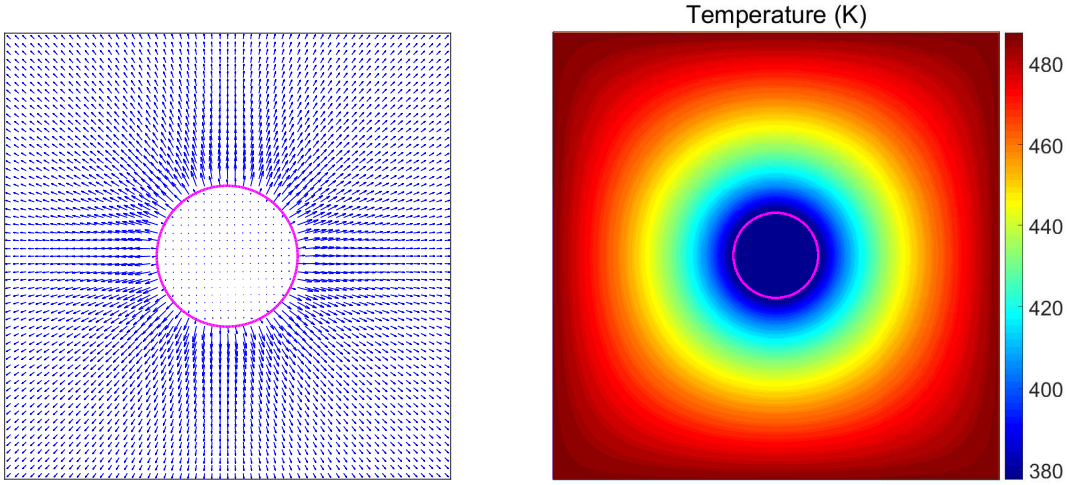

Figure 4.7: (Left) The velocity vectors showing the Stefan flow generated in the gas domain as a result of evaporation. For clarity in the presentation, every 2nd grid point data is plotted to generate the velocity field. Also, the velocity vectors are scaled by factor 1.5. (Right) Temperature contour plot is presented to demonstrate the gas phase temperature evolution. For both plots, $t^* = 8.0$, $St = 0.05$, $Sc = 1.0$, $Pr_l = 1.75$, $Pr_g = 0.7$, $\gamma = 5$ and $\zeta = 10$. Grid: 192×192.

therefore the squared-diameter (d^2) of a 2D evaporating droplet reduces with time according to the following analytical expression

$$\frac{dd^2}{dt} = -\frac{8k_g}{\rho_l c_{p,g}} \frac{\ln(1+St)}{\ln(d_{ins}/\sqrt{d^2})}. \tag{4.18}$$

where d_{ins} is the diameter of the inscribed circle in the computational domain. We numerically integrated Eq. (4.18) using MATLAB ode45 solver and compared the time history of the normalized d^2 with our simulation results for various values of Stefan number as shown in Fig. 4.8(a). A good agreement is observed till 50 % of the droplet mass is evaporated for all the three cases. Also, it is observed that, doubling the Stefan number reduces the time to reach 50 % mass reduction by half; the trend

similar to the findings of Safari et al. [19]. The inset shows droplet interface at two time instants during the course of evaporation for $St = 0.05$. The spherical symmetry is perfectly maintained during the evaporation. A grid convergence study is performed for $St = 0.025$, the global mass conservation error being the target parameter. The global mass conservation error is defined as

$$\varepsilon_{mass} = \left| \frac{\Delta M_l + \Delta M_{vap}}{M_{l_o}} \right| , \tag{4.19}$$

where ΔM_l and ΔM_{vap} denote the changes in the mass of the liquid droplet and vapor, respectively. These are computed as $\Delta M_l = M_{l_o} - M_{l_t}$ and $\Delta M_{vap} = M_{vap_o} - M_{vap_t}$, where M_l and M_{vap} are the liquid and vapor masses, respectively. The subscript 'o' denotes the initial values and 't' represents the corresponding variables at time instant t. Figure 4.8(b) shows the global mass conservation error plotted against the percentage reduction in the droplet mass for various grid resolutions for $St = 0.025$. The error approaches to zero as the grid is refined demonstrating the consistency and the grid convergence of our numerical method. The inset shows the order of convergence for this test case which is above the first order.

4.1.4 Evaporation of a 2D Moving Droplet

This is the case of an evaporating droplet moving under the action of the gravity. A droplet of initial diameter $d_o = 0.25$ mm is centered at $(x_c, y_c) = (0.5,3.6)$ mm in a 1 $\times$ 4 mm^2 domain. The initial droplet temperature is $T_{sat} = 373$ K whereas gas phase temperature is initialized as 480 K. Domain boundaries are specified as walls where the Dirichlet boundary conditions are specified for temperature and species mass fraction as $T_w = 480.0$ K and $Y_w = 0$, respectively. The magnitude of the gravitational acceleration g is varied to obtain various combinations of Eotvos (Eo) and Morton (Mo) numbers, which characterize the shape of drop moving in a surrounding fluid. Eotvos and Morton numbers are defined as $Eo = (\rho_l - \rho_g)d^2g/\sigma$ and $Mo = \mu_g^4(\rho_l - \rho_g)g/\rho_g^2\sigma^3$. The method is first tested for the global mass conservation and grid convergence for a moving droplet that deforms sufficiently while evaporating as may be the case in the combustion environment. The physical properties are selected to

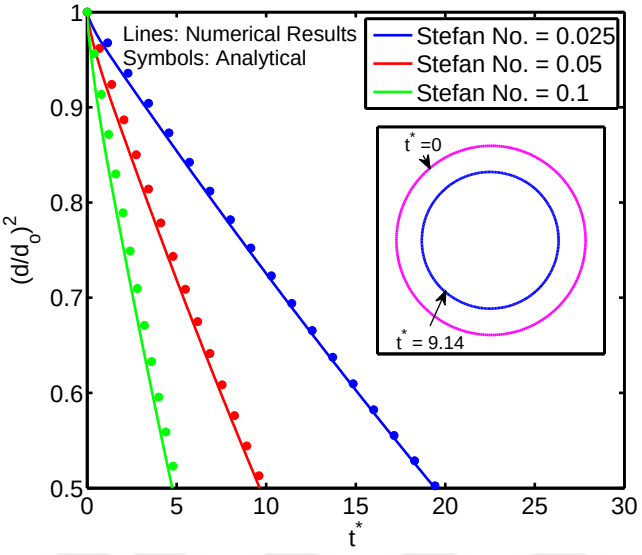

(a)

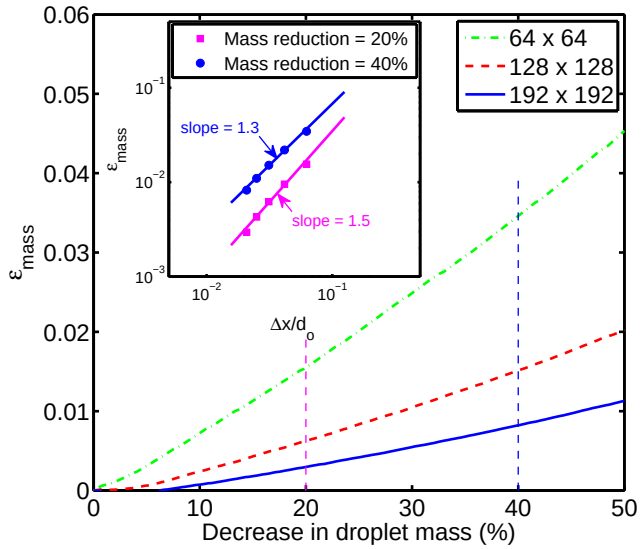

(b)

Figure 4.8: (a) Comparison of the analytical and numerical results for the normalized d^2 plotted versus non-dimensional time t^* for $St = 0.025$, 0.05 and 0.1. The inset shows interface at two instants during evaporation at $t^* = 0$ and 9.14 for $St = 0.05$. Grid: 192×192. (b) The global mass conservation error is plotted against the percentage decrease in droplet mass for $St = 0.025$ for various grid resolutions showing the grid convergence. The inset shows the order of accuracy of the method. For both figures $Sc = 1.0$, $Pr_l = 1.75$, $Pr_g = 0.7$, $\gamma = 5$ and $\zeta = 10$.

have the non-dimensional parameters as $Eo = 10$, $Mo = 10 \times 10^{-4}$, $St = 0.1$, $Sc = 1$, $Pr_l = 5.37$, $Pr_g = 1.0$, $\gamma = 5$ and $\zeta = 20$. The initial droplet diameter d_o is selected as the length scale and $\sqrt{d_o/g}$ is the time scale for this case. Figure 4.9 shows the contour plots of temperature and vapor mass fraction and the global mass conservation error for different grid resolutions. The results clearly indicate that the

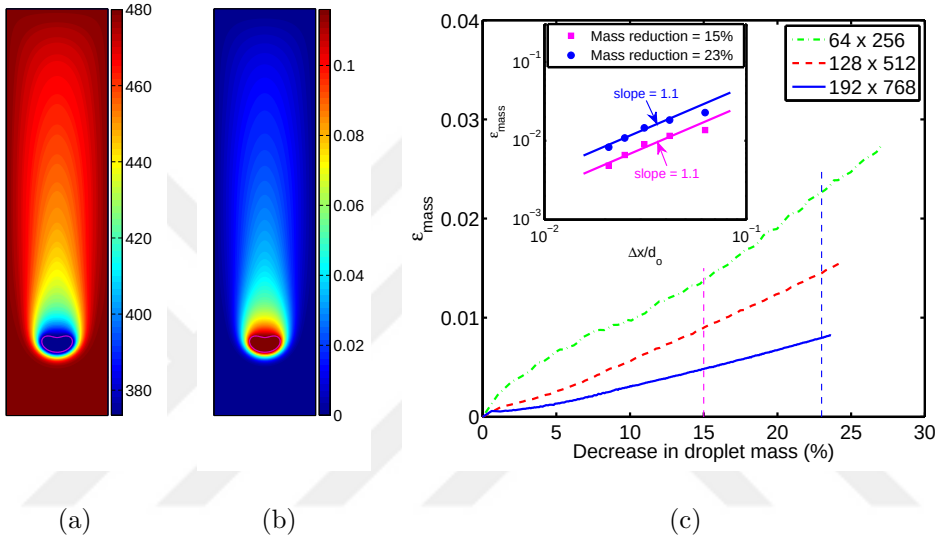

(a) (b) (c)

Figure 4.9: The contour plots of (a) temperature and (b) vapor mass fraction for an evaporating droplet falling under the action of the gravity at $t^* = 13.416$ and 128×512 grid resolution. (c) The global mass conservation error is plotted against the percentage decrease in droplet mass for various grid resolutions showing the grid convergence. The inset shows the order of accuracy of the method. $Eo = 10$, $Mo = 10 \times 10^{-4}$, $St = 0.1$, $Sc = 1.0$, $Pr_l = 5.37$, $Pr_g = 1.0$, $\gamma = 5$ and $\zeta = 20$.

mass conservation error decreases as the grid is refined for this more stringent test case. Also the spatial order of accuracy is almost linear (1st-order). Figure 4.10 shows the contour plots of vapor mass fraction for three separate cases, from left to right, in order of increasing droplet deformation. The corresponding Eo and Mo numbers are $(Eo,\ Mo) = (5,\ 5{\times}10^{-4})$, $(10,\ 10{\times}10^{-4})$ and $(20,\ 20{\times}10^{-4})$. The other parameters are fixed at $St = 0.1$, $Sc = 1$, $Pr_l = 5.37$, $Pr_g = 1.0$, $\gamma = 5$ and $\zeta = 20$ for all the three cases. It is observed that, as the droplet departs from the spherical shape, it evaporates faster as shown in Fig. 4.11. This trend is justified because evaporation is

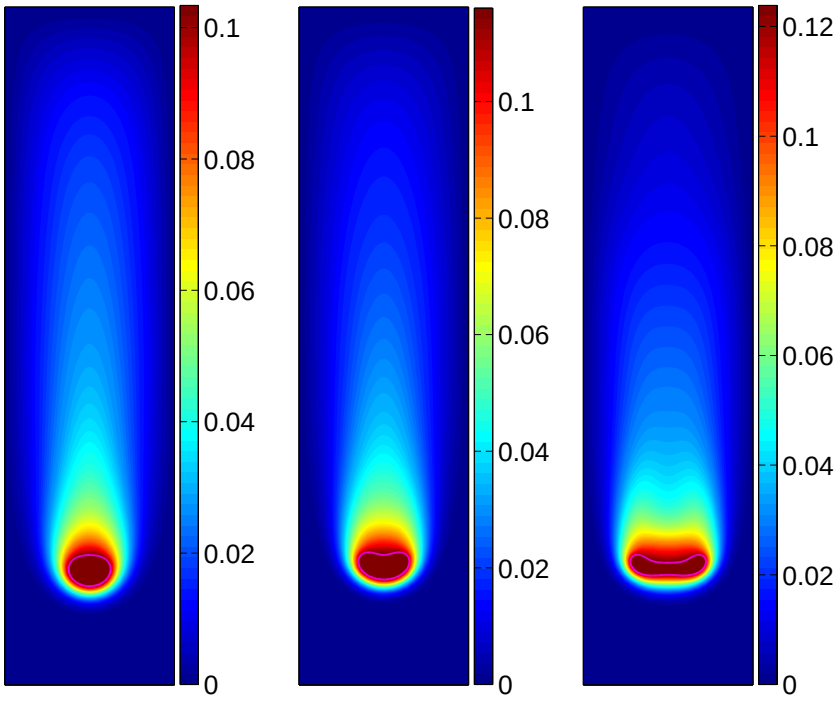

Figure 4.10: Evaporation of droplets falling under gravity with varying degree of deformation. Contour plots of the vapor mass fraction for three separate cases (from left to right): $Eo = 5$, $Mo = 5{\times}10^{-4}$, $t^* = 13.914$; $Eo = 10$, $Mo = 10{\times}10^{-4}$, $t^* = 13.416$; $Eo = 20$, $Mo = 20{\times}10^{-4}$, $t^* = 16.44$. Grid: 128×512.

a surface phenomenon and occurs due to temperature gradient at the interface; and since more surface area is exposed to high temperature in case of deformed droplets as compared to the spherical one, therefore, evaporation is enhanced. It is important to mention that all droplets are in the spherical shape as they start their journey therefore their evaporation histories overlap as shown during the early stages of time. But as the droplets continue to move under the gravitational force, they start to deform depending on their Eo and Mo numbers; the more deformed droplets losing their area faster through evaporation.

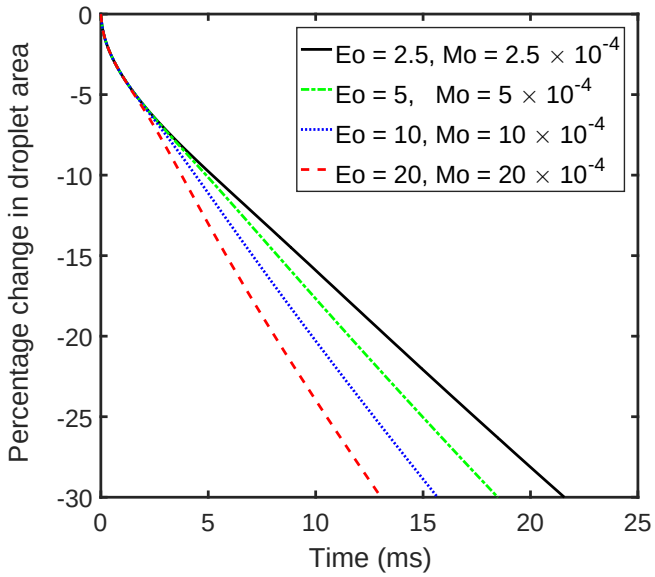

Figure 4.11: The percentage of the droplet area lost as a result of evaporation plotted against time for various combinations of Eo and Mo numbers.

4.2 Species Gradient Based Evaporation Model

This model depicts a more general situation where phase change occurs owing to the species concentration gradient across the interface. A number of tests are performed to validate the numerical solution algorithm. The computation of evaporation mass flux is an important parameter which depends on the correct coupling of the interface

temperature with the species mass fraction at the interface through the Clausius-Clapeyron relation. Also, the implementation of species boundary condition at the interface is very crucial for the species solver to ensure the global mass conservation.

4.2.1 Validation Test - 1: Evaporation Mass Flux

An efficient numerical phase change model must be able to predict evaporation mass flux accurately, since it is an important parameter in the phase change phenomenon that determines the rate of evaporation and consequently the interface location. The problem setup consists of a container filled with water upto a certain level. Air fills the rest of the container. The air-water interface is marked as $y = 0$. Based on the interface temperature, vapor mass fraction at the interface, Y^{Γ}_{vap}, is computed using the Clausius-Clapeyron relation. Sufficiently far from the interface, at $y = L$, the air is dry, i.e., $Y^{L}_{vap} = 0$. At the interface, water vapor diffuses into the air and a Stefan flow is setup in the gas phase that convects the vapor away from the interface. Hence, a complete convective-diffusive species equation needs to be solved for the vapor field in the gas domain. The water is assumed to be motionless. The schematic of this test case is shown in Fig. 4.12. For this simplified test case, the interface temperature

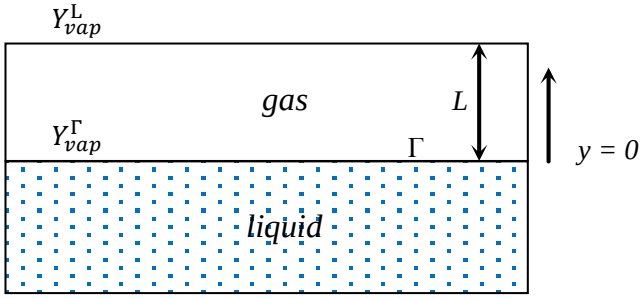

Figure 4.12: A schematic illustration of the validation case for the evaporation mass flux.

is assumed to stay constant during the simulation, therefore Y^{Γ}_{vap} is constant too. Also, it is assumed that the liquid evaporated is replenished exactly and continuously,

therefore the location of the interface stays fixed. Furthermore, the surrounding gas is assumed to be insoluble in water so there is no net transport of surrounding gas into the container. The physical properties of water and air are used for this test case. For one complete simulation where interface temperature stays constant, these physical properties are also assumed to be constant, but for different interface temperature boundary conditions, the properties are varied accordingly.

The mass conservation principle applied over a small control volume for vapor source yields the following differential equation [82],

$$\dot{m}_{vap} = \dot{m}_{vap} Y_{vap} - \rho_g D_\alpha \left. \frac{dY_{vap}}{dy} \right|_\Gamma^g , \tag{4.20}$$

where $\dot{m}_{vap}$ is the evaporation flux per unit time at the interface. Eq. (4.20) is solved subject to the following boundary conditions

$$Y_{vap}|_{y=0} = Y_{vap}^\Gamma , \qquad Y_{vap}|_{y=L} = Y_{vap}^L , \tag{4.21}$$

which results in the analytical solution given by

$$\dot{m}_{vap} = \frac{\rho_g D_\alpha}{L} \ln(1+B), \tag{4.22}$$

where B is the mass number given as

$$B = \frac{Y_{vap}^\Gamma - Y_{vap}^L}{1 - Y_{vap}^\Gamma}. \tag{4.23}$$

The evaporation mass flux per unit time is non-dimensionalized by the factor $\rho_g D_\alpha / L$. An increase in the interface temperature increases Y_{vap}^Γ and therefore the mass number B is also increased since $Y_{vap}^L = 0$. Figure 4.13 compares the numerical results of the non-dimensional evaporation mass flux rate with the analytical solution for various values of mass number B. The computational results approach the analytical solution as the grid is refined which shows that our numerical algorithm is grid convergent and precisely computes the convective and diffusive mass transfer components. For high values of mass number B, i.e., high evaporation rates, much finer grid resolutions are required to reach the analytical values which is quite expected and self explanatory.

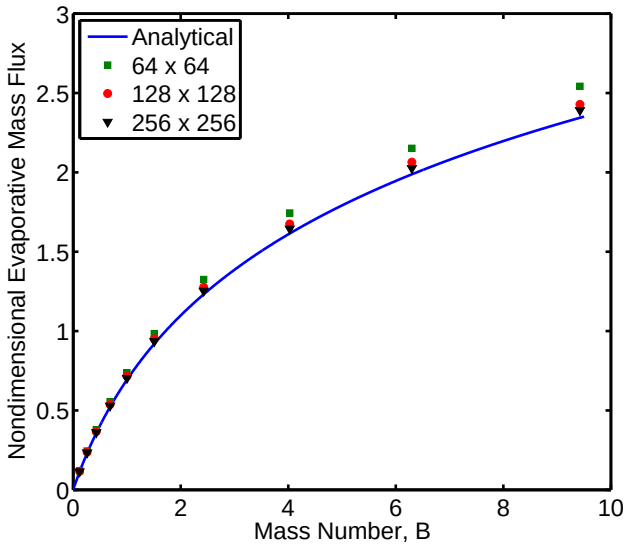

Figure 4.13: The numerical results of the non-dimensional evaporation mass flux rate compared with the analytical solution for various values of mass number B.

4.2.2 Validation Test - 2: Wet Bulb Temperature Comparison with Psychrometric Chart

For this test case, the computational setup consists of a liquid droplet of initial diameter $d_o = 0.25$ mm held stationary at the center of a 1×1 mm^2 domain. Initially, the temperature (dry bulb temperature) is the same throughout the domain and the phase change occurs due to the species gradient at the interface resulting in a low temperature at the interface. This goes lower and lower as evaporation proceeds until a steady state temperature condition is attained at the interface, called the wet bulb temperature. The liquid droplet also comes into equilibrium with the wet bulb temperature. This wet bulb temperature is a function of the dry bulb temperature (DBT) and the relative humidity (RH) in the air. The Dirichlet boundary conditions are specified at the domain boundaries for both the temperature and the vapor mass fraction, i.e., T_g and Y_{vap}, respectively. Y_{vap} can be computed as $Y_{vap} = \omega_h/(1+\omega_h)$, where ω_h is the humidity ratio which is a function of dry-bulb temperature and rela-

tive humidity; and can be read from a psychrometric chart. At the interface, the vapor mass fraction boundary condition Y^{Γ}_{vap} may be specified using any of the strategies discussed in Sections 3.3.1 or 3.3.2. Both of these are first compared for the global mass conservation for the case with DBT = 313 K and RH = 10%. The physical properties of air and water are used for all the following cases unless otherwise stated except for the liquid density ρ_l which is taken as 10 kg/m^3. k_l is modified accordingly to obtain the thermal diffusivity value α_l for water. d_o and d_o^2/D_α are selected as the length and the time scales, respectively, for all the cases related to the static droplet evaporation. The comparison shown in Fig. 4.14(a) suggests that, for the same grid size, the adsorption layer concept of distributing evaporation mass flux in the immediate outer vacinity of the interface and then adding as source term (Section 3.3.2) results in better mass conservation as compared to directly imposing Y^{Γ}_{vap} as the interface boundary condition for species mass fraction (Section 3.3.1). However, for both the methods, the trends of global mass conservation error clearly show the grid convergence. Figure 4.14(b) shows the global mass conservation error plotted against the non-dimensional grid size for the strategy 3.3.2. Two sets of data points are used corresponding to 20 % and 40 % mass losses during the droplet evaporation. The spatial order of accuracy is more than one in this case. For all the cases to follow, we stick with the strategy of Muradoglu and Tryggvason [62, 63] (Section 3.3.2) for implementing the vapor mass fraction boundary condition at the interface.

Various cases are then simulated with dry bulb temperatures in the range 283 K - 313 K and relative humidities 10 - 90 %, and the resulting wet bulb temperatures are compared with the psychrometric chart values. A grid convergence study is performed first to select a suitable grid resolution applicable to the rest of the simulations. Figure 4.15 shows the grid convergence results for the wet bulb temperature and the variation of normalized d^2 with the non-dimensional time t^* corresponding to DBT = 283 K - 313 K and RH = 10 %. It is found that a 128 $\times$ 128 grid resolution yields grid convergent results for both the indicators. Moreover, the temperature results converge faster as compared to the interface location. The results of the normalized

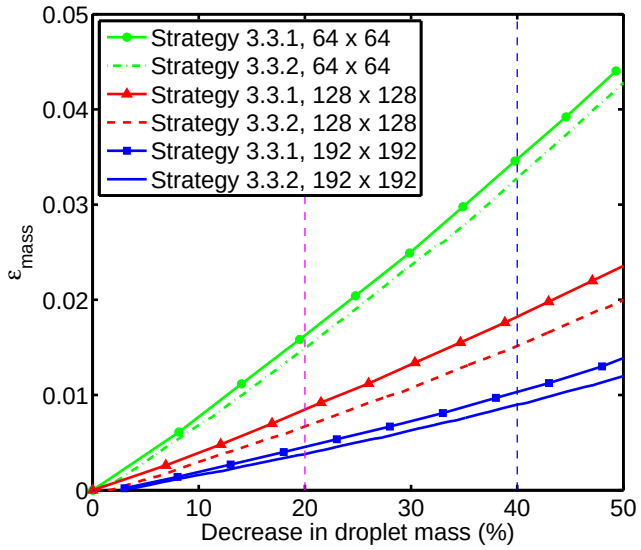

(a)

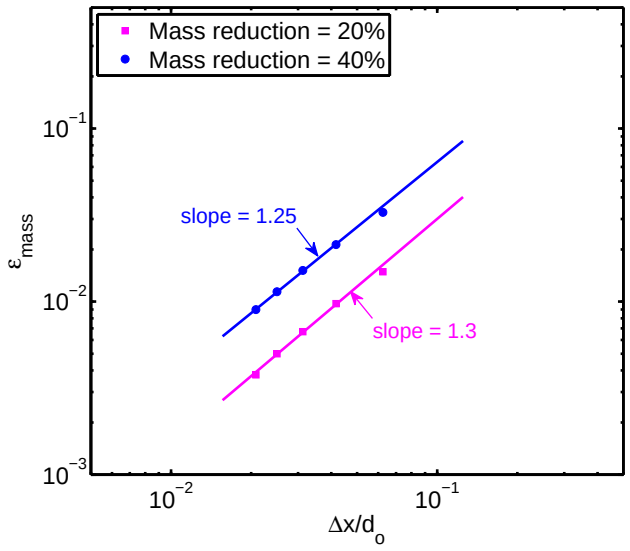

(b)

Figure 4.14: (a) Comparison of the two strategies for implementing the vapor mass fraction boundary condition at the interface. The global mass conservation error is plotted for various grid resolutions demonstrating the grid convergence. The strategy 3.3.2 shows lesser global mass conservation errors as compared to the strategy 3.3.1 for the same grid resolution. (b) The global mass conservation error is plotted against the non-dimensional grid size using the strategy 3.3.2 when 20% and 40% of the droplet mass is evaporated displaying the spatial order of accuracy greater than 1 at both instances. For both plots DBT = 313 K and RH = 10%.

d^2 are also compared with the analytical solution. The analytical expression derived for the variation of d^2 with time for a 2D evaporating droplet case is given by

$$\frac{dd^2}{dt} = -\frac{8\rho_g D_\alpha}{\rho_l} \frac{\ln(1+B)}{\ln(d_{ins}/\sqrt{d^2})}, \tag{4.24}$$

where B is defined by Eq. (4.23) and d_{ins} is the diameter of the inscribed circle in the computational domain. Equation (4.24) is solved using MATLAB ode45 solver. The analytical and numerical profiles for the variation of normalized d^2 with time show good agreement as the grid is refined, as shown in Fig. 4.15.

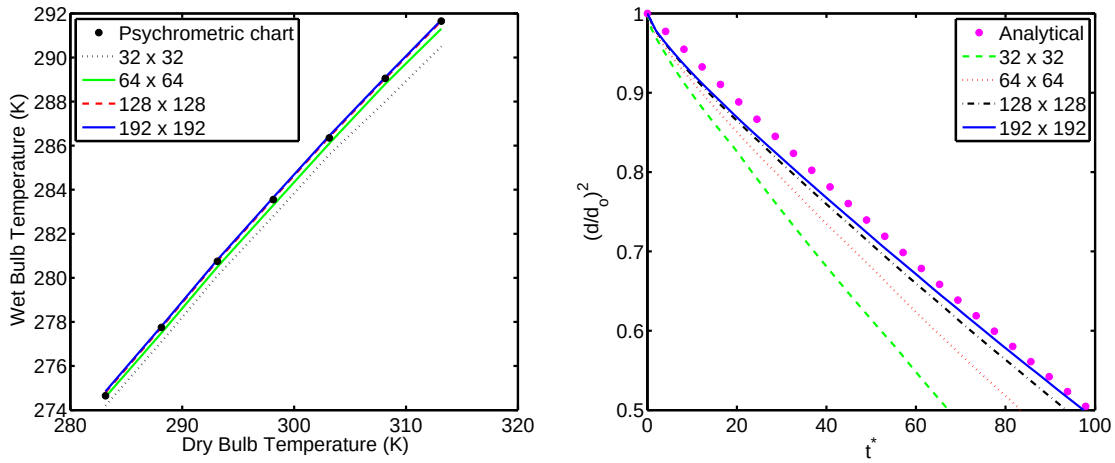

Figure 4.15: Grid convergence study: (Left) Numerical results of wet bulb temperatures converge to the psychrometric chart values for DBT = 283 K - 313 K and RH = 10 %, (Right) The simulation results for the variation of normalized d^2 with the non-dimensional time t^* compared with the analytical solution. DBT = 313 K, RH = 10 %.

Some sample contour and line plots are then presented for the case with DBT = 313 K and RH = 50%. Figure 4.16 shows the contour plots for the evolution of temperature and vapor mass fraction fields. A better illustration of the temperature evolution may be seen in Fig. 4.17, which shows temperature profiles along the horizontal center line of the domain at various time instants during the evaporation. Once an equilibrium wet bulb temperature is attained, all the heat absorbed just results in the phase change.

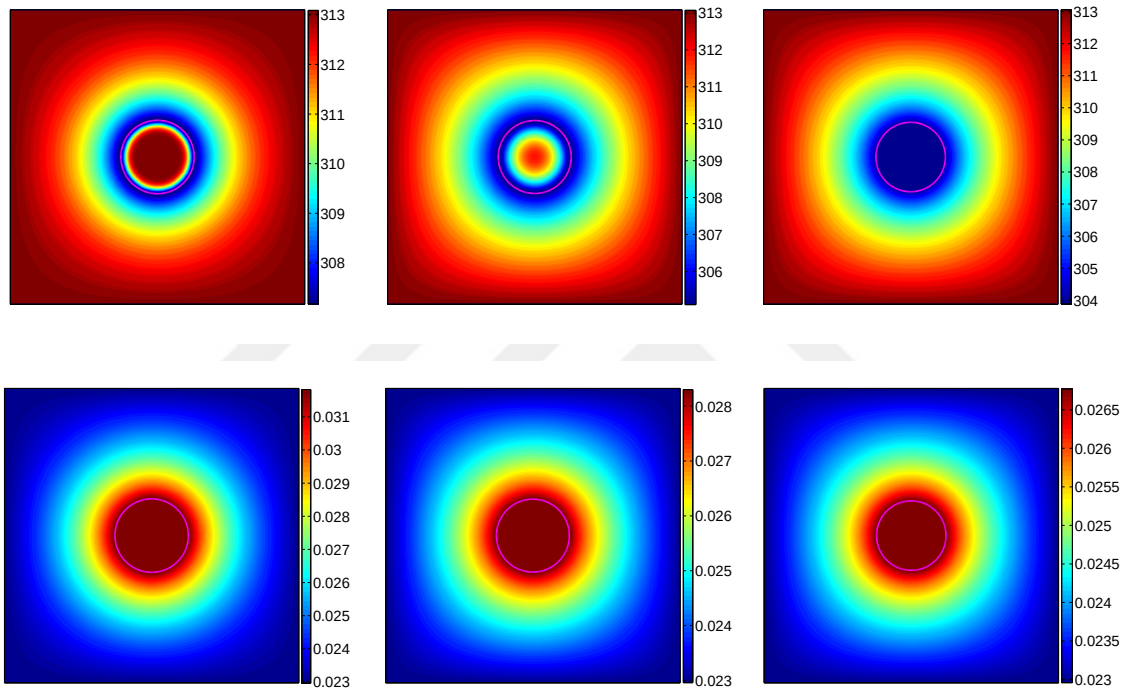

Figure 4.16: Contour plots of temperature (top row) and vapor mass fraction (bottom row) for an evaporating droplet at non-dimensional times (from left to right) $t^* = 0.424$, 4.24 and 42.4; the wet bulb temperature is reached in the right most plot of the top row. DBT = 313 K, RH = 50 % and Grid: 128 $\times$ 128.

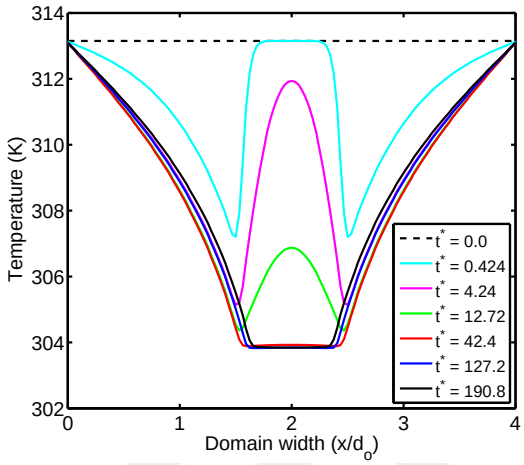

Figure 4.17: Temperature profiles plotted along the horizontal centerline of the domain width at various non-dimensional times t^*. The steady state temperature condition is achieved inside the evaporating droplet. DBT = 313 K, RH = 50 %.

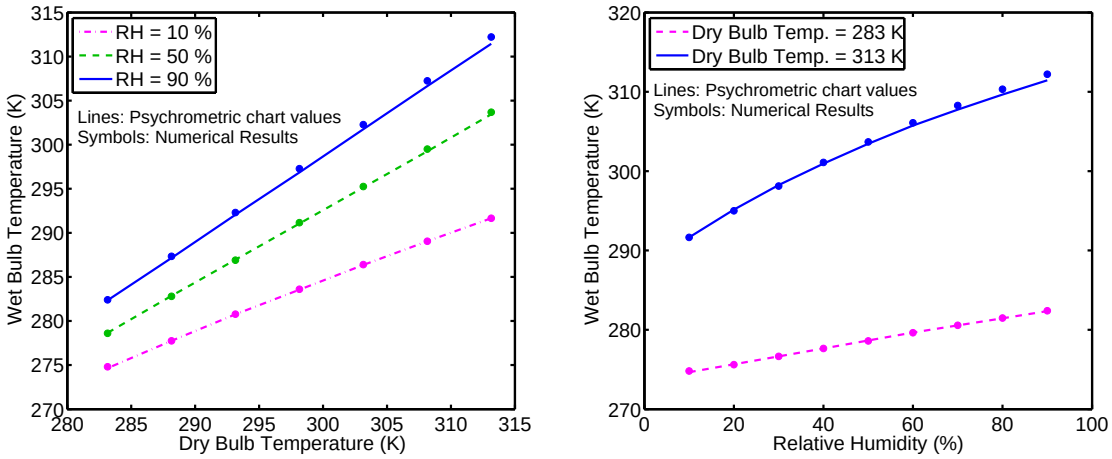

Figure 4.18: Numerical results of wet bulb temperatures compared with the psychrometric chart values for various combinations of dry bulb temperatures and relative humidities. Grid: 128 × 128.

Next, we made three sets of runs by keeping the relative humidity fixed at 10 %, 50 % and 90 % respectively, and varying the dry bulb temperature in the range 283 K - 313 K for each case. In the final batch of runs, the temperature is held constant at 283 K and 313 K and the relative humidity is varied from 10 % to 90 % for the each case. The comparison of the numerical results with the psychrometric chart results are shown in Fig. 4.18. Numerical results are in excellent agreement with the psychrometric chart values, however, some deviation is observed at high dry bulb temperatures and high relative humidities. This may be attributed to our constant properties assumption, since the thermophysical properties vary significantly at high temperatures and high relative humidities [83].

4.2.3 Evaporating Droplet Falling Under Gravity

This section simulates the 2D planar case of an evaporating droplet that moves due to the gravitational acceleration **g**, and deforms during the journey. The initial diameter, d_o, of the droplet is 0.25 mm. The domain size is selected as 1×4 mm^2. The droplet is initially placed with its center at (0.5,3.6) mm and starts from the rest. Temperature is initialized as 371 K in the whole domain whereas the saturation temperature is $T_{sat} =$ 373 K. The domain boundaries are set as walls, and the Dirichlet boundary conditions are specified for the temperature and vapor mass fraction at walls as $T_g = 371$ K and $Y_{vap} = 0$, respectively. The vapor mass fraction boundary condition at the interface is implemented following the strategy 3.3.2 of Muradoglu and Tryggvason [62, 63]. The other physical properties are selected to have the relevant non-dimensional parameters as $Eo = 10$, $Mo = 10 \times 10^{-5}$, $Sc = 1.0$, $Pr_l = 54.08$, $Pr_g = 0.15$, $\gamma = 5$ and $\zeta =$ 20. d_o and $\sqrt{d_o/g}$ are the appropriate length l_s and time t_s scales, respectively; and the velocity scale is calculated as $u_s = l_s/t_s$. Figure 4.19 shows the contour plots of the vapor mass fraction at different time instants during the life of droplet, as it falls due to the gravity. The global mass conservation results are shown in Fig. 4.20. It is observed that the global mass conservation error reduces as the grid is refined. The order of accuracy is close to one for this deformed droplet evaporation case which

shows the ability of our method to handle highly deformed interfaces. The method is overall second order accurate in space but the spatial accuracy reduces to first order for the global mass conservation mainly due to the smoothing of discontinuous fields such as evaporation mass source at the interface.

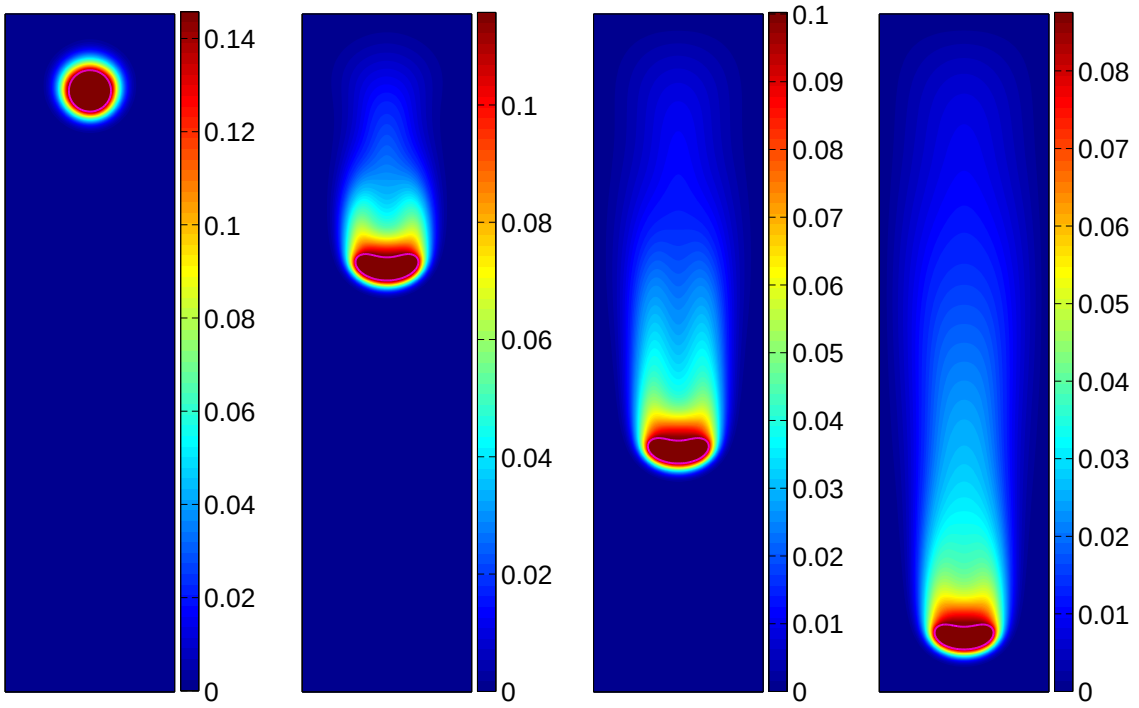

Figure 4.19: Contour plots of the vapor mass fraction for a moving, deforming and evaporating droplet at four time instants $t^* = 0.89$, 5.37, 9.84 and 14.31. Grid: 128 $\times$ 512. The non-dimensional parameters are $Eo = 10$, $Mo = 10 \times 10^{-5}$, $Sc = 1.0$, $Pr_l = 54.08$, $Pr_g = 0.15$, $\gamma = 5$ and $\zeta = 20$.

Finally, some sample results are presented for the multiple droplets that move, evaporate, deform and interact with each other. Two droplets are initially placed with their centers $2d_o$ apart in a 1.5 $\times$ 4 mm^2 domain and move under the action of the gravity. Temperature is initialized as 363 K in the whole domain whereas all other properties are same as for the single droplet case. Figure 4.21 shows the snapshots

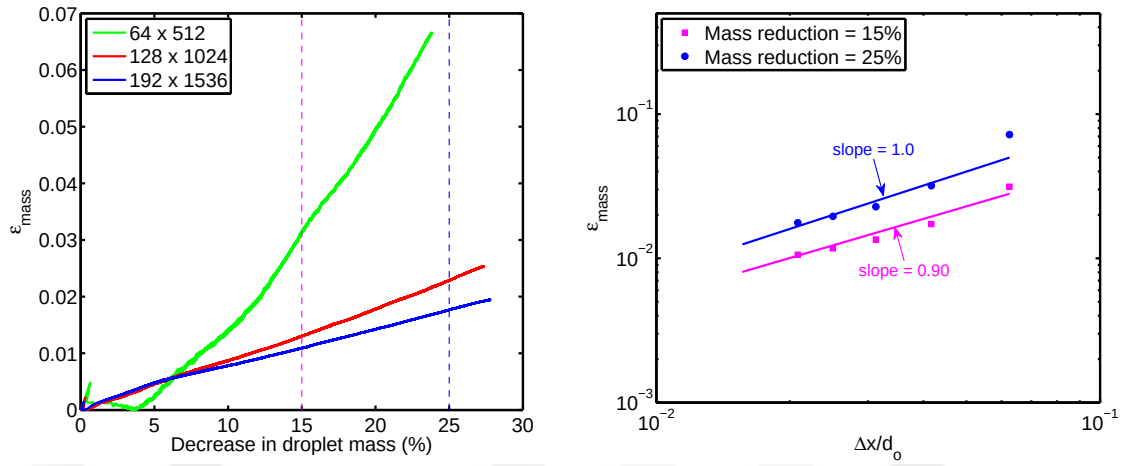

Figure 4.20: (Left) The global mass conservation error plotted against the percentage decrease in the droplet mass for a moving deforming and evaporating droplet at various grid resolutions. (Right) The global mass conservation error versus the non-dimensional grid size after 15% and 25% of the droplet is evaporated. The relevant nondimensional parameters are $Eo = 10$, $Mo = 10 \times 10^{-5}$, $Sc = 1.0$, $Pr_l = 54.08$, $Pr_g = 0.15$, $\gamma = 5$ and $\zeta = 20$.

of their path history as they start from the rest. The global mass conservation error plots are shown in Fig. 4.22.

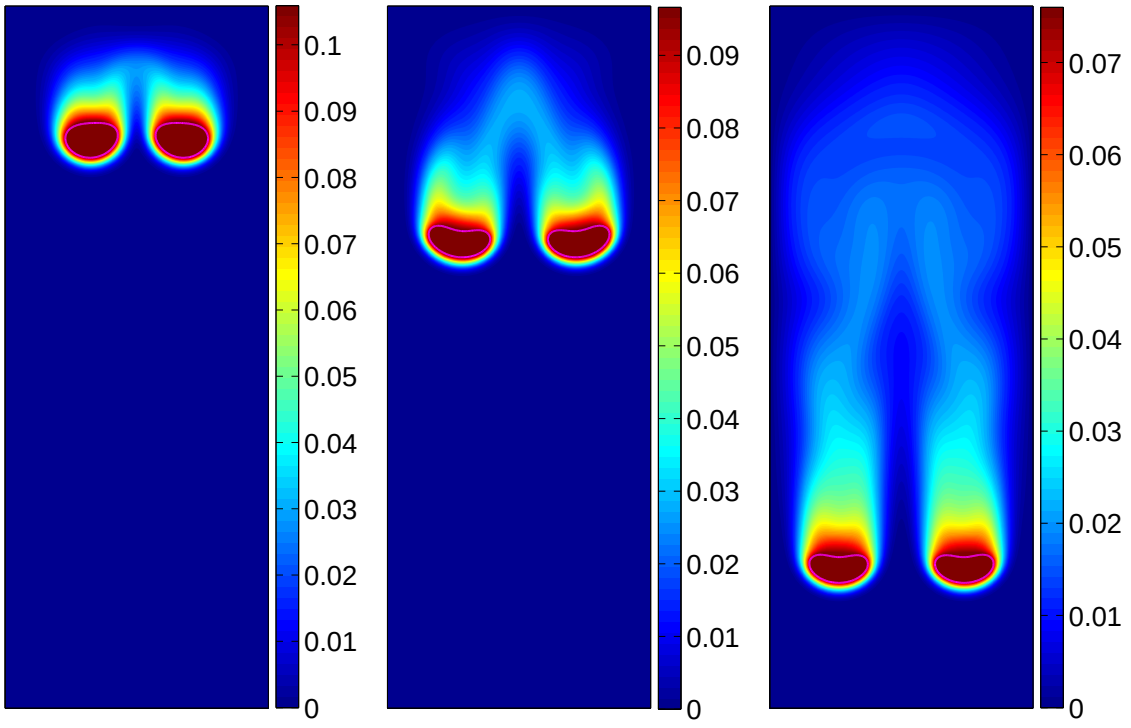

Figure 4.21: Contour plots of the vapor mass fraction for two moving, deforming, interacting and evaporating droplets at various time instants (from left to right): t^* = 2.68, 5.37 and 14.31. The non-dimensional parameters are Eo = 10, Mo = 10 $\times 10^{-5}$, Sc = 1.0, Pr_l = 54.08, Pr_g = 0.15, γ = 5 and ζ = 20. Grid: 192 $\times$ 512.

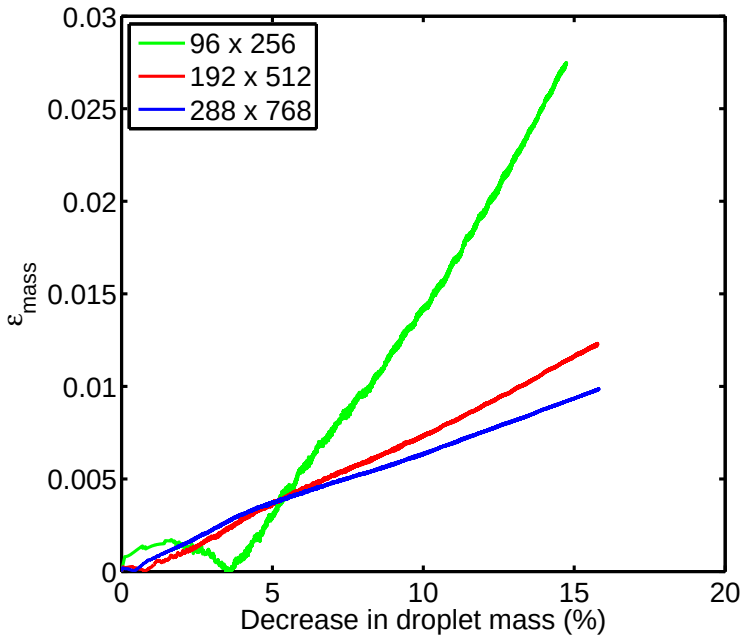

Figure 4.22: The global mass conservation error plotted against the percentage decrease in the droplet mass for two moving, deforming, interacting and evaporating droplets at various grid resolutions. Error reduces as the grid is refined.

Chapter 5

EVAPORATION AND BURNING OF A FUEL DROPLET

Fuel sprays are of fundamental importance in many combustion systems, e.g., internal combustion engines, turbines, rocket engines, etc. The efficiency of such a combustion system is greatly dependent on the design of fuel injectors that produce fuel sprays. The study of the behavior of a single droplet in the fuel spray can give us a good insight into the basic physical and chemical processes taking place in the spray combustion. A liquid fuel droplet evaporates in hot environment producing fuel vapors which further react with oxidizer to produce energy and products of combustion. One of the factors that highly influence the ignition process of a fuel droplet is the ambient gas temperature. Researchers have performed both experimental and numerical studies to explore the combustion of different single and multicomponent fuel droplets under varying ambient conditions. In this chapter we developed and validated multiphase phase change solver in axisymmetric configuration before incorporating the combustion modeling. We preferred to switch from 2D planar configuration to the axisymmetric configuration in order to directly compare our results with the experiments (3D) and the previous axisymmetric numerical studies for validation purposes.

In an axisymmetric configuration, as shown in Fig. 5.1, the momentum conservation equations for v_r and v_z velocity components in the r and z coordinate directions, respectively, can be written in conservative form as

$$\begin{aligned}\frac{\partial \rho v_r}{\partial t}+\frac{1}{r}\frac{\partial r\rho v_r^2}{\partial r}+\frac{\partial \rho v_r v_z}{\partial z} &= -\frac{\partial p}{\partial r}+\Delta\rho g_r+\frac{\partial}{\partial r}\left(2\mu\frac{\partial v_r}{\partial r}\right)+\frac{\partial}{\partial z}\mu\left(\frac{\partial v_r}{\partial z}+\frac{\partial v_z}{\partial r}\right)\\ &\quad+\frac{\partial}{\partial r}\left(2\mu\frac{v_r}{r}\right)+\int_A \sigma\kappa\mathbf{n}\delta(\mathbf{x}-\mathbf{x}_\Gamma)dA\cdot\mathbf{i}_r\ , \qquad (5.1)\end{aligned}$$

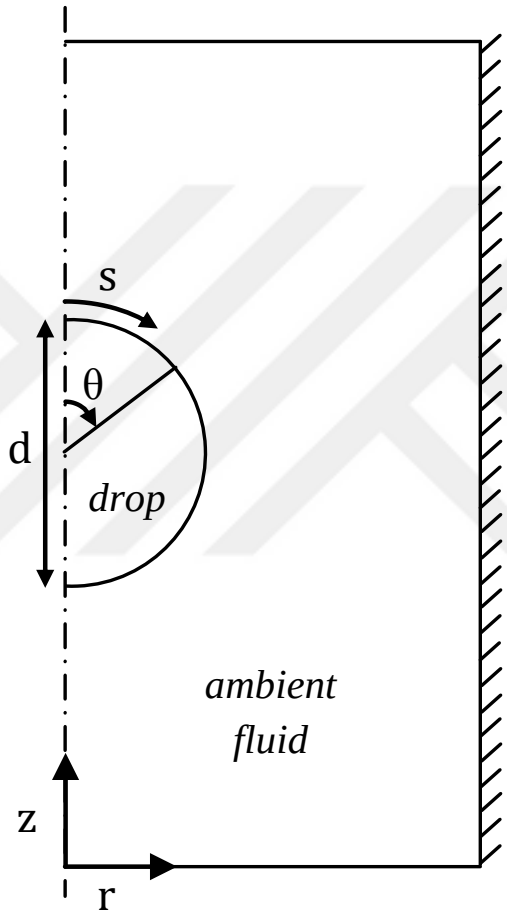

Figure 5.1: The schematic illustration of a drop in an axisymmetric configuration.

$$\frac{\partial \rho v_z}{\partial t} + \frac{1}{r}\frac{\partial r \rho v_z v_r}{\partial r} + \frac{\partial \rho v_z^2}{\partial z} = -\frac{\partial p}{\partial z} + \Delta \rho g_z + \frac{1}{r}\frac{\partial}{\partial r}\mu r \left(\frac{\partial v_r}{\partial z} + \frac{\partial v_z}{\partial r}\right) + \frac{\partial}{\partial z}\left(2\mu \frac{\partial v_z}{\partial z}\right) + \int_A \sigma \kappa \mathbf{n} \delta(\mathbf{x} - \mathbf{x}_\Gamma) dA \cdot \mathbf{j}_z \ . \quad (5.2)$$

The conservative form of energy and species equations can be written for axisymmetric configuration as

$$\frac{\partial \rho c_p T}{\partial t} + \frac{1}{r}\frac{\partial r \rho c_p T v_r}{\partial r} + \frac{\partial \rho c_p T v_z}{\partial z} = \frac{1}{r}\frac{\partial}{\partial r}\left(rk\frac{\partial T}{\partial r}\right) + \frac{\partial}{\partial z}\left(k\frac{\partial T}{\partial z}\right) - \Lambda \int_A \delta(\mathbf{x} - \mathbf{x}_\Gamma) \dot{q_\Gamma} dA_\Gamma - \sum_\alpha \dot{\Omega}_\alpha H_\alpha(T) \ , \quad (5.3)$$

$$\frac{\partial \rho Y_\alpha}{\partial t} + \frac{1}{r}\frac{\partial r \rho Y_\alpha v_r}{\partial r} + \frac{\partial \rho Y_\alpha v_z}{\partial z} = \frac{1}{r}\frac{\partial}{\partial r}\left(r\rho D_\alpha \frac{\partial Y_\alpha}{\partial r}\right) + \frac{\partial}{\partial z}\left(\rho D_\alpha \frac{\partial Y_\alpha}{\partial z}\right) + \dot{S}_\alpha + \dot{\Omega}_\alpha \qquad \alpha = 1, 2, ..., n_s \ , \quad (5.4)$$

where $\dot{\Omega}_\alpha$ represents the rate of production of the species component ρY_α as a result of chemical reaction and $H_\alpha(T)$ represents the enthalpy of the species component α.

5.1 Validation of the Axisymmetric Multiphase Solver

This section aims to validate the front tracking multiphase solver in an axisymmetric configuration as a foundation step towards the development of a solver for the direct numerical simulation of phase change and combustion of a liquid droplet in a gaseous ambient environment. The set of governing equations explained above (Eqs. (5.1) - (5.4)) are used with $\dot{q}_\Gamma = \dot{S}_\alpha = \dot{\Omega}_\alpha = 0$ in combination with the incompressibility condition $\nabla \cdot \mathbf{u} = 0$ satisfied throughout the domain.

The validation case simulates the gravity driven falling droplet in a straight channel for which numerical results are available in the literature [84, 85]. An initially spherical liquid droplet of diameter d is centered at (r_c,z_c) = (0, 13.75d) in a rigid cylinder filled with an ambient fluid. Due to higher density of the droplet as compared to the ambient fluid, the droplet accelerates downwards. The computational domain is 5d and 15d in the radial and axial directions, respectively. At the cylinder walls no-slip boundary condition is applied whereas axisymmetry condition is applied at

the centerline. The problem is governed by four non-dimensional parameters, namely, the Eötvös number $Eo = g_z(\rho_d - \rho_o)d^2/\sigma$, the Ohnesorge number $Oh_d = \mu_d/\sqrt{\rho_d d\sigma}$, the density ratio $\gamma = \rho_d/\rho_o$ and the viscosity ratio $\zeta = \mu_d/\mu_o$. The Ohnesorge number for the ambient fluid is defined as $Oh_o = \mu_o/\sqrt{\rho_o d\sigma}$. The subscripts 'd' and 'o' denote the properties of drop and ambient fluids, respectively. The computational domain is resolved by 512 $\times$ 1536 uniform cartesian grid. For all the results presented here, the physical properties are selected to have the non-dimensional parameters as: Oh_d = 0.0466, $Oh_o = 0.05$, $\gamma = 1.15$ and $\zeta = 1$. The axial component of the gravitational acceleration, g_z, is varied to have the desired Eo numbers as 12, 24, 48 and 96. The time and centroid velocity are non-dimensionalized by the time scale $\sqrt{d/g_z}$ and the velocity scale $\sqrt{dg_z}$, respectively. First, the results are presented for the shape evolution of the droplet as it moves down the channel for $Eo = 48$ and 96. The qualitative comparison with the results of Han and Tryggvason [84] shows excellent agreement as shown in Fig. 5.2. Next, the comparison is made for the non-dimensional centroid velocity V^* of the falling droplet as shown in Fig. 5.3. An excellent quantitative agreement is also observed with the results of Han and Tryggvason [84] for $Eo = 12$ and 24. However, some deviation is seen for higher Eo numbers. This is mainly due to the fact that the drop shape is deformed substantially as Eo increases and in certain regions numerical resolution is not good enough to capture the full physics of the problem. Also, the numerical approximations and the restructuring of the interface for highly deformed geometry may have contributed towards the error. The volume conservation error is also plotted in Fig. 5.3. As can be seen, the error is less than 0.2 % for all the cases studied.

The above mentioned computational setting is then used to test the method for a high density ratio case, $\gamma = 10$. Eight different cases are simulated with Eo number varying from 12 to 96 with an increment of 12. The other non-dimensional parameters relevant to this test case are: $\zeta = 3.164$ and $Oh_d = Oh_o = 0.05$. For all the cases, the droplet starts from rest and accelerates due to the gravity. During the journey the droplet takes various complicated shapes depending on the Eo number:

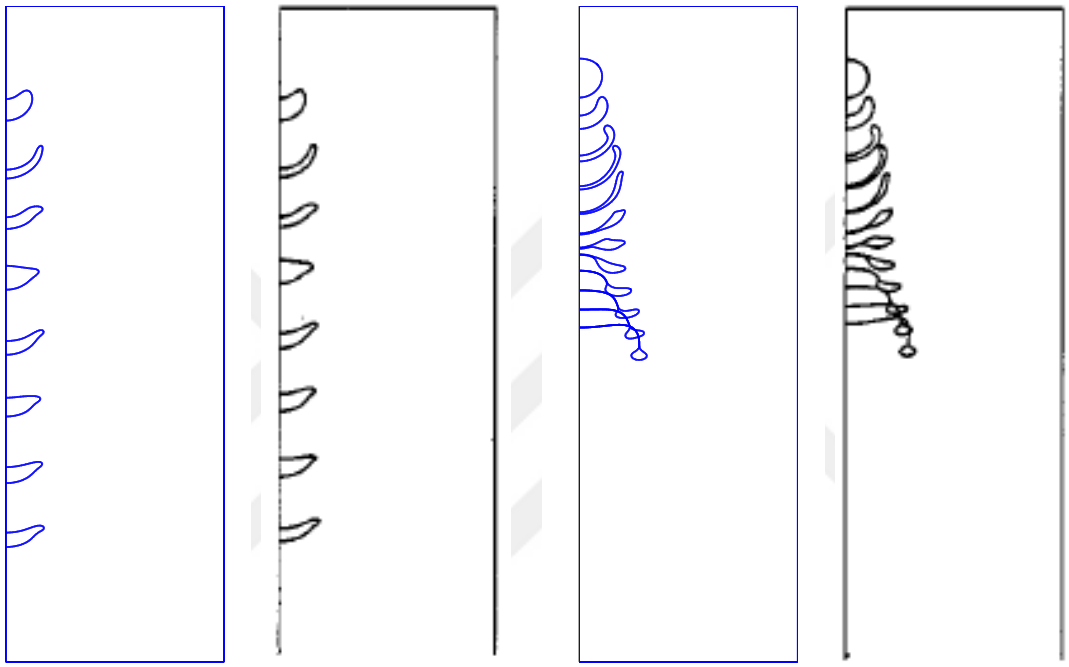

(a) Eo = 48 (b) Eo = 96

Figure 5.2: Comparison of the present results (left in each subfigure) with the numerical results of Han and Tryggvason [84] (right in each subfigure) for the evolution of drop shapes as it moves down the channel under the gravitational force for Eötvös numbers (a)$Eo = 48$ and (b)$Eo = 96$. Other non-dimensional parameters are $Oh_d = 0.0466$, $Oh_o = 0.05$, $\gamma = 1.15$ and $\zeta = 1$. The gap between two successive drops in each column represents the distance the drop travels at a fixed time interval and the last interface is plotted at (a)$t^* = 44.72$ and (b)$t^* = 37.94$. Grid: 512×1536.

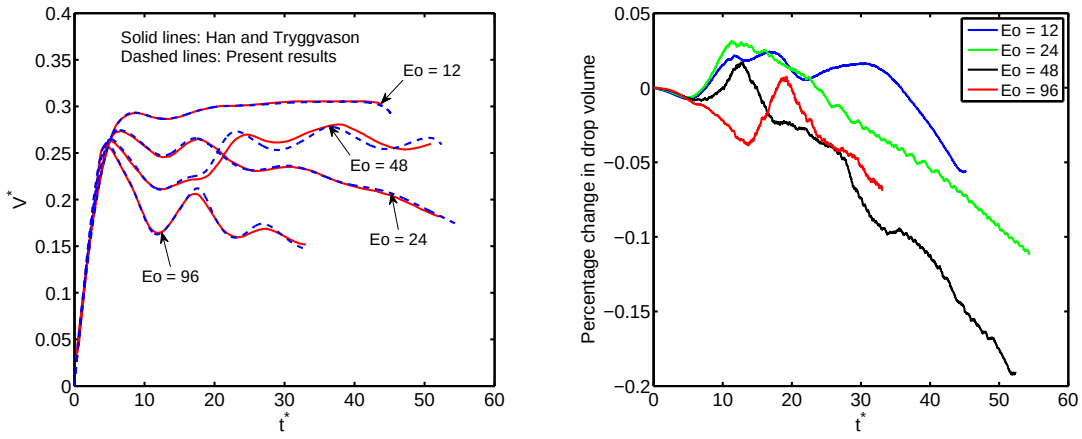

(a) (b)

Figure 5.3: (a) Comparison of the non-dimensional centroid velocity V^* of a falling droplet with the numerical results of Han and Tryggvason [84] for $Eo = 12$, 24, 48 and 96. (b) The volume conservation error is plotted against the non-dimensional time t^*. The error is less than 0.2 % for all the cases. The non-dimensional parameters for this study are $Oh_d = 0.0466$, $Oh_o = 0.05$, $\gamma = 1.15$ and $\zeta = 1$. Grid: 512×1536.

the higher the Eo number, the more is the droplet deformed. Figure 5.4 shows the shape evolution of the falling drop for $Eo = 12$, 24, 48 and 96. It is clear that for $Eo = 96$, the droplet is substantially deformed in the form of a thin filament and may result in a breakup. Note that breakup is not allowed in the present simulations. The centroid velocity of the droplet increases as it moves down the channel and reaches a maximum value. To quantitatively validate our numerical results, the maximum value of the non-dimensional centroid velocity V^* is compared with the results of Han and Tryggvason [84] as shown in Fig. 5.5(a). An excellent agreement is observed for all the Eo number cases, which shows the capability of the current solver to handle high density ratio cases. To further analyze the performance, the volume conservation error is plotted for $Eo = 12$, 24, 48 and 96, as shown in Fig. 5.5(b). The error increases as the Eo number increase which is quite expected. However, the maximum error incurred for the extremely deformed droplet case ($Eo = 96$) is approximately 0.3%. Also, it is important to note that for all the results presented here, the tendency is

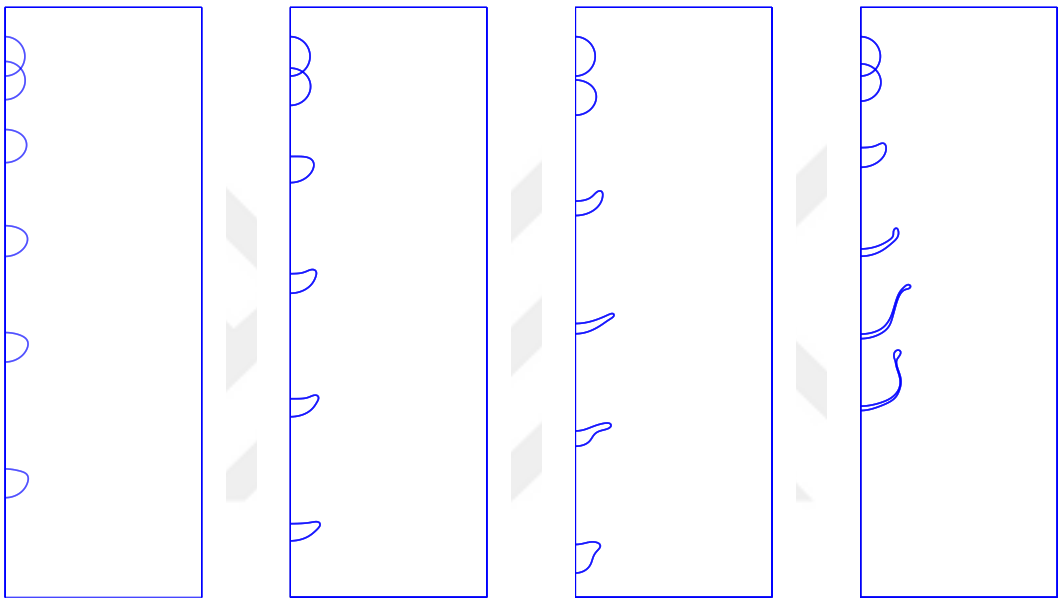

(a) Eo = 12 (b) Eo = 24 (c) Eo = 48 (d) Eo = 96

Figure 5.4: The shape evolution of a falling droplet moving under the action of gravity for four different cases: $Eo = 12$, 24, 48 and 96. The gap between two successive drops in each column represents the distance the drop travels at a fixed time interval and the last interface is plotted at t^* = (a) 6.39, (b) 7.1, (c) 8.21 and (d) 6.45. The non-dimensional parameters are: $Oh_d = Oh_o = 0.05$, $\gamma = 10$ and $\zeta = 3.164$. Grid: 512×1536.

towards the volume loss, i.e., the negative error.

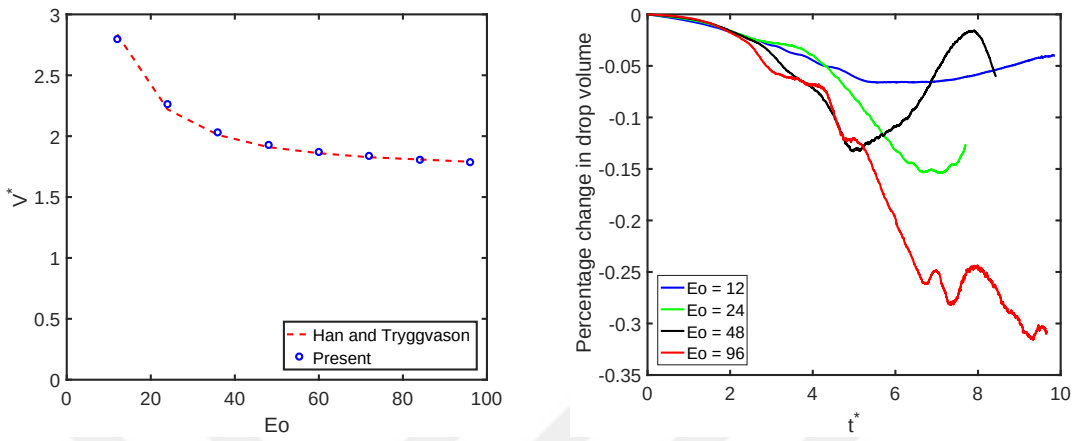

Figure 5.5: (a) The maximum values of the non-dimensional centroid velocity V^* of a falling droplet compared with the numerical results of Han and Tryggvason for various Eo numbers. (b) The volume conservation error (in percent) plotted versus non-dimensional time t^* for four different cases: Eo = 12, 24, 48 and 96. The non-dimensional parameters valid for the whole study are: $Oh_d = Oh_o = 0.05$, $\gamma = 10$ and $\zeta = 3.164$. Grid: 512×1536.

5.2 Temperature Gradient Based Phase Change

The temperature gradient based phase change process is incorporated into the axisymmetric multiphase solver (Section 5.1). The governing equations, Eqs. (5.1) - (5.4), are solved in combination with the modified continuity equation, Eq. (2.2) in the front tracking framework. In this section, chemical reaction is not yet included, therefore, $\dot{\Omega}_\alpha$ is set to 0 in Eqs. (5.3) & (5.4). Numerical implementation details particular to this process are explained in Section 3.2 except for the one modification. The numerical approximation for smoothing an interface quantity, say ϕ_Γ, onto fixed grid node (i, j) for the axisymmetric configuration reads as

$$\phi_{i,j} \;=\; \sum_k \phi_\Gamma^k w_{i,j}^k \frac{r_k \Delta s_k}{r_{i,j} h^2} \;, \tag{5.5}$$

where r_k and $r_{i,j}$ are the radial coordinates of the kth marker point and the grid node (i, j), respectively. The remaining nomenclature retains its previous meaning.

5.2.1 Validation Test - d^2 Law

This case simulates a static liquid droplet of initial diameter d_o evaporating in a hot gaseous environment. An axisymmetric droplet is centered at $(0, 5d_o)$ in a domain of size $5d_o$ and $10d_o$ in the radial and axial directions, respectively. The domain is discretized using 256×512 uniform grid cells. The temperature of the droplet is initialized as T_{sat} and stays fixed during the whole simulation, whereas the gas phase temperature is initialized as T_g which evolves as the simulation proceeds. The same initial gas phase temperature is set as wall temperature boundary condition. At the interface, T_{sat} is applied as the interface temperature boundary condition following the strategy discussed in Section 3.3.1 [65]. The length and time scales are selected as d_o and d_o^2/α_g, respectively, where α_g is the thermal diffusivity of the gaseous phase.

Numerical results are presented and compared with the analytical solution for the variation of normalized d^2 with the non-dimensional time t^* for various Stefan numbers. The analytical solution is available in the combustion textbooks [66, 86] for this classical phase change problem, termed as d^2 law, and is expressed as

$$\frac{dd^2}{dt} = -\frac{8k_g}{\rho_l c_{p,g}} \ln(1 + St). \tag{5.6}$$

A good agreement is achieved between the numerical and analytical results for all the studied cases as shown in Fig. 5.6(a). However, it is observed that a slight difference exists between the slopes of analytical and numerical results. One striking reason is the fact that as the droplet gets smaller and smaller, grid resolution of the droplet gets worse and results deviate from the analytical solution. Second, in the analytical solution it is assumed that droplet evaporates in an infinite domain. But in numerical simulations, the computational cost restricts the domain dimensions to a finite size. We numerically experimented with different domain sizes for $St = 0.025$; the numerical results approach the analytical solution as we increase the domain size, as shown in Fig. 5.6(b). Another reason may be the volume conservation error (negative error in

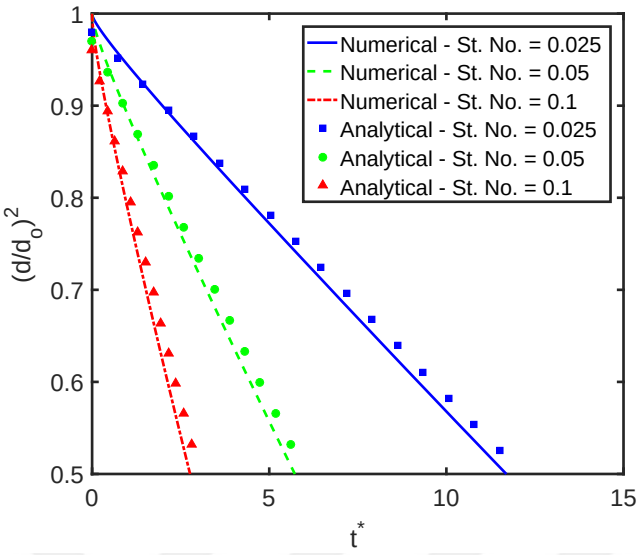

(a)

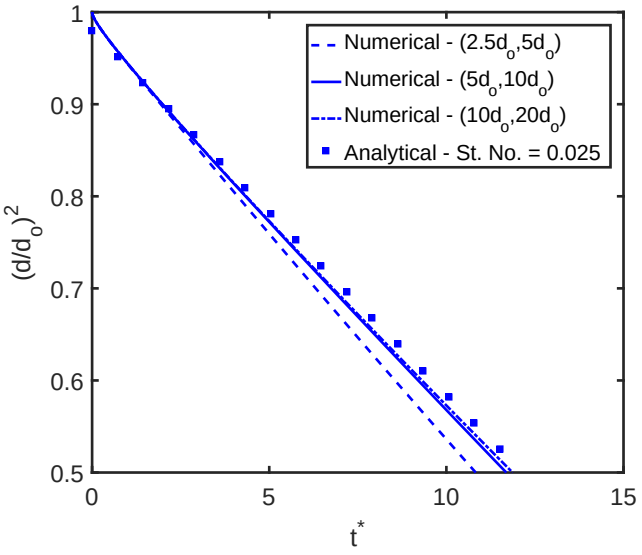

(b)

Figure 5.6: (a) Comparison of the analytical and numerical results for the normalized d^2 plotted against the non-dimensional time t^* for $St = 0.025$, 0.05 and 0.1. The domain size for these results is $5d_o$ and $10d_o$ in the radial and axial directions, respectively. Grid: 256 × 512. (b) Effects of domain size on the numerical results are shown for $St = 0.025$, the analytical solution is also plotted for reference. Three domain sizes are considered: ($2.5d_o$, $5d_o$), ($5d_o$, $10d_o$) and ($10d_o$, $20d_o$) in (r, z) coordinate directions, respectively. The respective grid sizes are: 128 × 256, 256 × 512 and 512 × 1024. The numerical results approach the analytical profile as domain size is increased. $\gamma = 5$ and $\zeta = 10$ for all the results presented.

our case) associated with the front tracking solver itself, as shown in Fig. 5.3. This supports and is consistent with our slightly higher slope. The results are expected to be further improved by grid refinement and by using stretched grid or adaptive mesh refinement.

Next, the results are presented for a n-heptane droplet evaporating in a quiescent nitrogen environment. This case is studied experimentally by Nomura et al. [50] in microgravity environment, and has been used by various researchers as a benchmark case to validate their phase change solvers [53]. Figure 5.7 shows the results of the

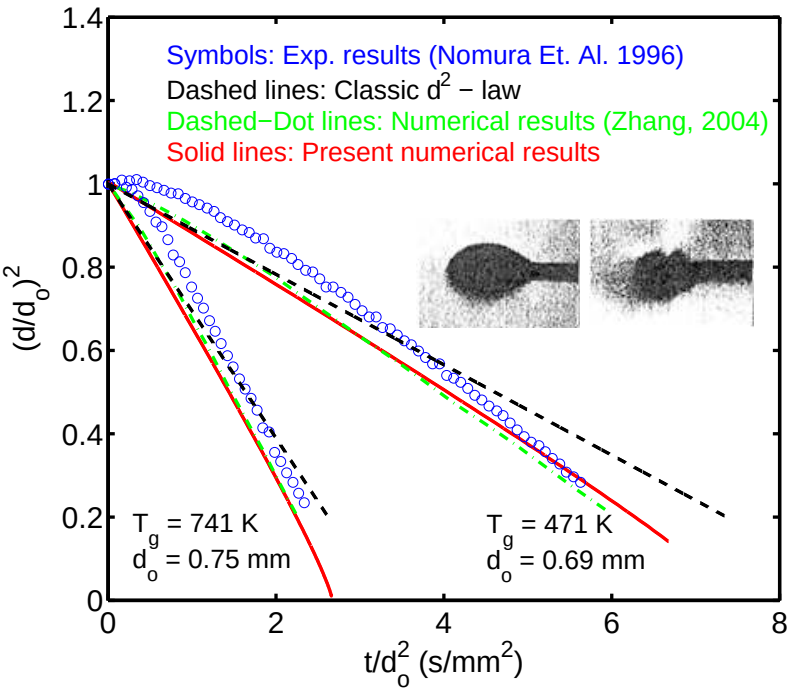

Figure 5.7: Normalized d^2 plotted against t/d_o^2 for an evaporating n-heptane droplet. The present numerical results are compared with the experimental and previous numerical results as well as with the classical d^2-law. Two set of results are plotted with different initial gas phase temperatures T_g and diameters d_o. Insets show two snapshots from the experimantal results of Nomura et. al. during the evaporation process. $\gamma = 100$ and $\zeta = 10$. Grid: 192×384.

normalized d^2 variation with t/d_o^2, d_o being the initial drop diameter. Two separate

cases are studied with different initial gas phase temperature conditions T_g. The domain size is $2.5d_o$ and $5d_o$ in the radial and axial directions, respectively, and resolved by 192 $\times$ 384 uniform grid cells. The temperature inside the droplet is initialized as 300 K whereas initial gas phase temperature T_g is applied as the Dirichlet temperature boundary condition at the domain walls. The density and viscosity ratios are set as 100 and 10, respectively. Higher density ratio is also tested but no significant effect on the results is observed. The gas phase thermophysical properties are evaluated at the boiling temperature and are assumed to stay constant during the whole simulation as suggested by Miller et al. [52]. The present numerical results are in good agreement with the previous numerical results of Zhang [53]. Also, the present results overall follow the trends of the experimental results, however, some deviation is observed which is more at the initial stages of the evaporation process. The possible reasons are highlighted below.

1. The snapshots of an evaporating droplet taken during the experiments [50] are shown in the inset of Fig. 5.7 which reveal that the droplet is far from spherical shape whereas we assume perfect sphere in our numerical simulations.

2. In the experiments, droplet is generated at the tip of a silica fiber whereas no such effects are considered in numerics. In literature, several experimental and numerical studies are available to show the influence of supporting fiber on the droplet heat and mass transfer [42, 87, 88].

3. In the experiments, the droplet is introduced into the hot environment by translating it through some distance which may have introduced some convective currents. The flat portion at the start of the experimental results for both the test cases is supposed to be due to this reason, as also mentioned by Zhang [53].

5.3 Combustion, Chemical Kinetics and CHEMKIN

Combustion is a rapid oxidation process generating heat, or both heat and light. Combustion can takes place either in the flame or non-flame mode. Flames can further

be classified as either premixed or nonpremixed (diffusion) flames. The flame mode can be explained as the one where a thin zone of intense chemical reaction propagates through the unburned fuel-air mixture, as is the case of spark-ignition engine. This thin reaction zone is commonly called as a flame. Under certain conditions, the rapid oxidation reaction takes place at many locations within the unburned gas, leading to a very rapid combustion throughout the volume. Such a situation occurs in the compression ignition engines and is called as nonflame mode. The types of flames, premixed of nonpremixed (diffusion), are based on the mixing state of the reactants. In a premixed flame, the fuel and the oxidizer are thoroughly mixed before any chemical reaction takes place. The spark-ignition engine is an example where premixed flames occur. On the other hand, in the nonpremixed (diffusion) flame, the reactants are initially separated, and reaction occurs only at the interface between the fuel and oxidizer, where both mixing and reaction take place. A typical example of a diffusion flame is a simple candle [66].

The stoichiometric quantity of oxidizer is just that amount needed to completely burn a quantity of fuel. If more than a stoichiometric quantity of oxidizer is supplied, the mixture is said to be fuel lean; otherwsie the mixture is termed as fuel rich. The stoichiometric oxidizer-fuel ratio is determined by writing simple atom balances, assuming that the fuel reacts to form an ideal set of products [66]. For a hydrocarbon fuel C_xH_y, the stoichiometric relation can be written as

$$C_xH_y + a\,(O_2 + 3.76N_2) \rightarrow xCO_2 + (y/2)\,H_2O + 3.76aN_2 \ , \tag{5.7}$$

where

$$a = x + y/4. \tag{5.8}$$

For the current study, the air is assumed to be composed of 21% O_2 and 79% N_2 (by volume), i.e., for each mole of O_2 in air, there are 3.76 moles of N_2 [66].

The overall reaction for the oxidation of fuel can be expressed by the following global reaction mechanism

$$F + a\mathrm{Ox} \rightarrow b\mathrm{Pr} \ , \tag{5.9}$$

where one mole of fuel reacts with a moles of oxidizer to produce b moles of products. The global reaction mechanism for any combustion process can be called as a one-line summary of a set of elementary reactions taking place during the process. The collection of elementary reactions necessary to describe an overall reaction is called a reaction mechanism. Reaction mechanisms may be composed of a few or as many as several hundred elementary reactions involving many intermediate species. For a global reaction given by Eq. 5.9, the rate of fuel consumption can be expressed as [66]

$$\frac{\mathrm{d}\left[X_{\mathrm{F}}\right]}{\mathrm{d}t} = -G(T)\left[X_{\mathrm{F}}\right]^{n}\left[X_{\mathrm{Ox}}\right]^{m} \quad , \tag{5.10}$$

where $[X_{\mathrm{i}}]$ denotes the molar concentration of the ith species in the mixture and G is the global rate coefficient which is a strong function of temperature T. The minus sign indicates that the fuel concentration decreases with time. The rate of consumption of the fuel, given by Eq. 5.10, is proportional to each of the reactants raised to a power. The exponents n and m relate to the reaction order. Equation 5.10 says that the reaction is nth and mth order with respect to fuel and oxidizer, respectively, and $(n+m)$th order overall. For global reactions, n and m are not necessarily integers and arise from curve fitting experimental data, however, for elementary reactions, reaction orders are always integers. Molecular collision theory can be used to derive an expression for the rate coefficient for bimolecular reactions. If the temperature range of interest is not too great, the bimolecular rate coefficient can be expressed by the empirical Arrhenius form as

$$G(T) = A\exp\left(-E_A/RT\right) \quad , \tag{5.11}$$

where A is a constant called the pre-exponential factor or the frequency factor, E_A is the activation energy and R is the general gas constant [66].

CHEMKIN [67, 68] is a powerful tool to incorporate the gas-phase chemical kinetics into the fluid dynamics simulations. CHEMKIN, in combination with a general-purpose stiff ordinary differential equation integration package, VODE [89], is used to simulate the burning of fuel vapors in air produced as a result of evaporation of fuel droplet. Information about elements, species, chemical reaction mechanism and

thermodynamic data is required as an input. This information is provided using two input files: *chem.inp* and *therm.dat*. The CHEMKIN interpreter reads this symbolic information and create two output files: *chem.bin* and *chem.out*. The *chem.bin* file is a binary linking file containing the information on the chemical elements, species, reactions and thermodynamic data extracted from the *chem.inp* and *therm.dat* whereas *chem.out* is a text-format output of the interpreter containing all the details related to chemical reaction and an information about any error occurred while generating the binary linking file. *chem.bin* is then used in combination with the CHEMKIN library, VODE, and a driver file specifying the type of problem and the relevant initial conditions to solve the problem for the desired output data. A general structure of the CHEMKIN package is shown in Fig. 5.8.

5.4 Combustion of an Evaporating n-Heptane Droplet

The combustion of an evaporating droplet is simulated by incorporating the CHEMKIN package into our axisymmetric phase change solver. The whole set of governing equations (Eqs. (5.1) - (5.4)) are solved in addition to the gas-phase chemical kinetics. The continuity condition, Eq. (2.2), must be satisfied during the process. The Navier-Stokes equations are solved using the projection method [76] as explained in Section 3.1. The solution of the energy and species equations is advanced in time using a splitting scheme [69, 72] that computationally decouples the chemistry and the CFD components. The chemistry part is first solved for the evolution of the species and temperature fields in the domain from t^n to t^{n+1}

$$\frac{\partial \rho c_p T}{\partial t} = -\sum_{\alpha} \dot{\Omega}_\alpha H_\alpha(T) \ , \tag{5.12}$$

$$\frac{\partial \rho Y_\alpha}{\partial t} = \dot{\Omega}_\alpha \qquad\qquad \alpha = 1, 2, ..., n_s \ . \tag{5.13}$$

This step is performed using CHEMKIN in combination with VODE [89], a general-purpose stiff ODE solver. VODE uses time-implicit backward difference methods to integrate the chemistry component and utilizes adaptivity in the order of accuracy

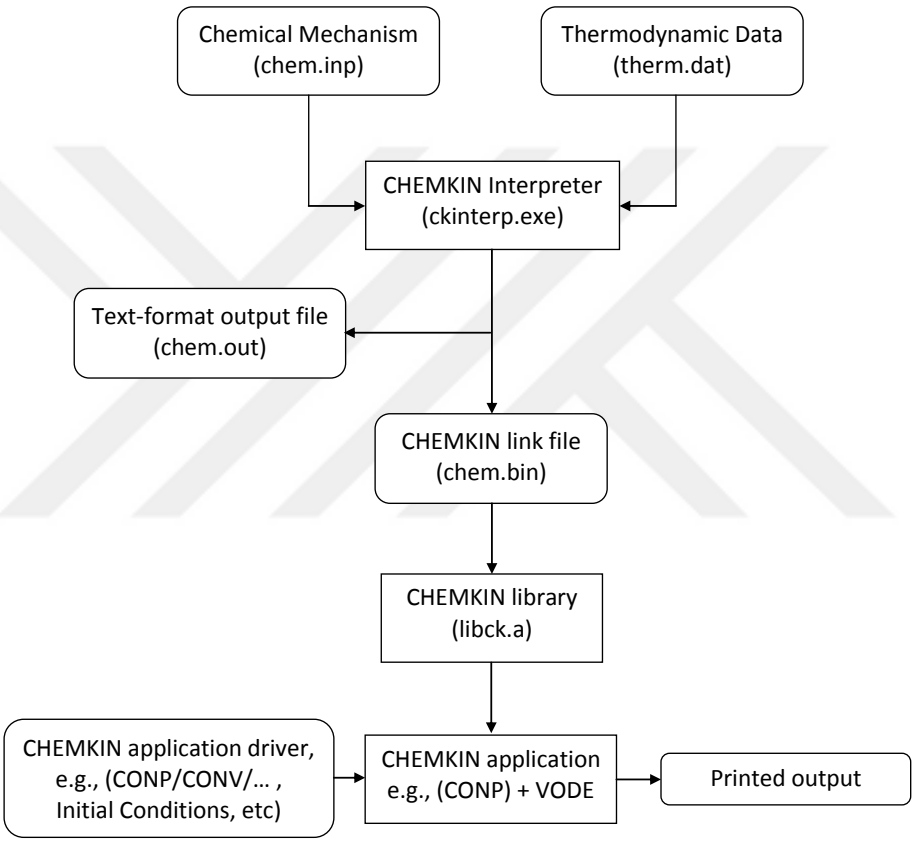

Figure 5.8: Block diagram illustrating the general flow of information in CHEMKIN and its relationship to an application program.

and subcycled time-step selection so that an absolute error tolerance of 10^{-16} in mass fractions is maintained throughout [69]. In the second step, CFD components of the energy and species equations are advanced in time using explicit Euler method, by setting $\dot{\Omega}_\alpha = 0$. This splitting scheme is first order accurate and is consistent with accuracy of the overall solution procedure.

A sample problem is first studied which considers a hydrogen-air reaction under constant pressure conditions [68]. The results reported in the manual [68] for the species mole fractions and temperature are exactly reproduced using the current solver. This verifies the accurate incorporation of the chemical kinetics solver (CHEMKIN) when triggered from our main code. To test the full functionality of the code, i.e., the correct coupling of the phase change and combustion solvers, comprehensive test cases are simulated that involve the combustion of an evaporating droplet in quiescent hot air environment.

5.4.1 Single Step Chemistry

The evaporation and combustion of a *n*-heptane droplet is studied and the numerical results are compared with the previous numerical results [54, 73] and some experimental data [90, 91, 92]. We made some simplifying assumptions for this analysis: Marangoni, Soret and Dufour effects are neglected, radiative heat transfer is not taken into account and a local thermodynamics equilibrium is assumed to be attained at the droplet interface. We assume a single step chemistry, constant thermodynamics properties, unity Lewis number for all the species and an ideal gas behaviour in the gas phase. The global chemical mechanism for *n*-heptane can be written as

$$C_7H_{16} + 11O_2 \rightarrow 7CO_2 + 8H_2O \ . \tag{5.14}$$

A section of *n*-heptane droplet is actually simulated by exploiting the axisymmetry condition at the centerline as schematically shown in Fig. 5.1. The initial diameter (d_o) of the droplet is 0.4 mm and is placed at the centerrline with center point coordinates as (r_o, z_o) = (0, 2) mm. The domain is $5d_o$ in radial and $10d_o$ in the axial direction and is discretized using 256 × 512 uniform grid cells. The droplet temperature is

initialized as the boiling point of the heptane, i.e., $T_o = T_b = 371.6$ K. The initial fuel mass fraction at the interface is 1 whereas all other species mass fractions are initialized as 0; the same values are applied as the species mass fraction boundary conditions at the interface during the whole simulation. Outside the droplet, in the gas domain, temperature is 500 K which evolves as the simulation proceeds. The gas domain is pure air composed of 79% N_2 and 21% O_2. The evaporation of n-heptane droplet produces fuel vapors around the droplet which react with the oxidizer in the air to produce the combustion products. Equation (5.4) is solved for all the species in the gas domain at each time step to obtain an updated species field. At the domain boundaries, the temperature and species boundary conditions are 500 K and pure air, respectively. It is observed that the fuel air mixture does not automatically ignite unless the ignition energy is supplied by artificially increasing the temperature locally using an external heat source. In the present study, temperature is increased to 1800 K in the gas domain around the droplet for 50 time steps subjected to the conditions: $Y_{C_7H_{16}} > 0.01$ and $Y_{O_2} > 0.01$. Once the fuel is ignited the combustion proceeds in a smooth fashion.

First a grid convergence study is performed; results are presented for species mass fractions and temperature for two grid resolutions as shown in Fig. 5.9. Species mass fraction profiles almost overlap for the two grids used whereas temperature profile shows a small gap at the peak. Hence 256×512 grid is considered fine enough to proceed for the rest of the study. Results are then presented for the variation of normalized squared-diameter $(d/d_o)^2$ and fuel gasification rate k with t/d_o^2, as shown in Fig. 5.10(a). The comparison with the previous numerical study [73] shows an overall similar trends with some deviations. One contributing factor towards this gap may be the difference in the computational and operating parameters, e.g., the domain size, ignition heat source and its duration, etc. When the ignition starts, a partially premixed flame first develops near the droplet and then transforms into a diffusion flame. The close proximity of the flame induces excessive droplet vaporization, pushing the flame outwards [54]. This transient phase with high vaporization/gasification

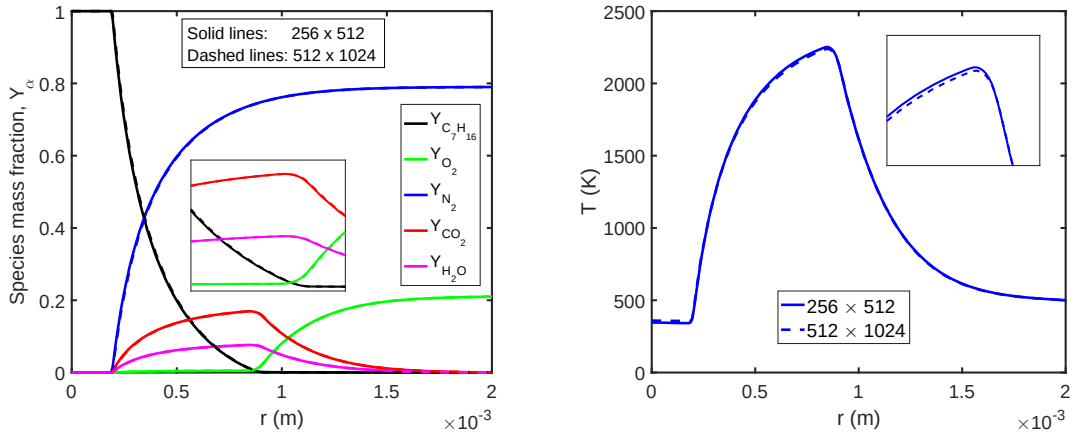

(a) (b)

Figure 5.9: Grid convergence study: Profiles of (a) species mass fractions and (b) temperature plotted along the horizontal centerline for two grid sizes; insets show the magnified views around the sharp gradients. No visible difference is observed for the case of species mass fractions, However, a small difference is observed around the temperature peak. Maximum temperature decreases on grid refinement. For both plots $t/d_o^2 = 0.09375$.

rates results in the fast reduction in the droplet area, i.e., d^2. Both these trends are clearly visible during the early stages of time as shown in Fig. 5.10(a). In contrast, the numerical results of Jin and Shaw [73] show a more extended ignition delay time and low gasification rate at the initial stages. The peak temperatures produced in the gas domain as a result of chemical reaction are plotted and compared with the previous numerical results, as shown in Fig. 5.10(b): a temperature spike is produced as the reaction starts which gradually smooths out to a steady state value. The similar observation is also reported by Cho and Dryer in their numerical study [54]. Figure 5.11 shows the temperature and species mass fraction contour plots for oxygen and nitrogen at four different instants during the droplet burning showing their evolution in time during the course of combustion. The flame is produced and diffuses outwards maintaining the spherical symmetry. Profiles of the species mass fractions and temperature are plotted at $z = 5d_o$ as shown in Fig. 5.12. The peak temperature marks the location of the flame front: to the left of this point there is no oxidizer and

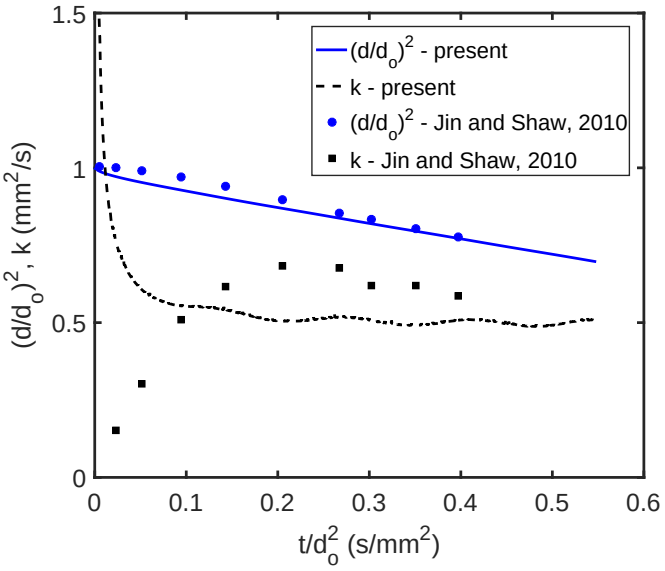

(a)

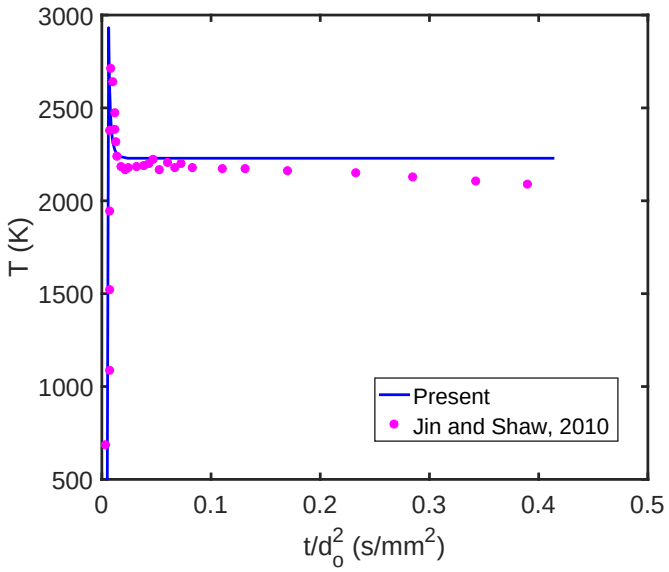

(b)

Figure 5.10: (a) Comparison of the present and previous numerical results for the variation of normalized d^2 and the fuel gasification rate k for an evaporating and burning n-heptane droplet with the time t/d_o^2. The gasification rate k approximately attains a steady state value at $t/d_o^2 = 0.15$ for the present case. (b) The peak values of the gas phase temperatures plotted against t/d_o^2 and compared with the previous numerical results. The present results approach a steady state value whereas results of Jin and Shaw continue to decrease. The initial droplet diameter d_o is 0.4 mm. Grid: 256×512.

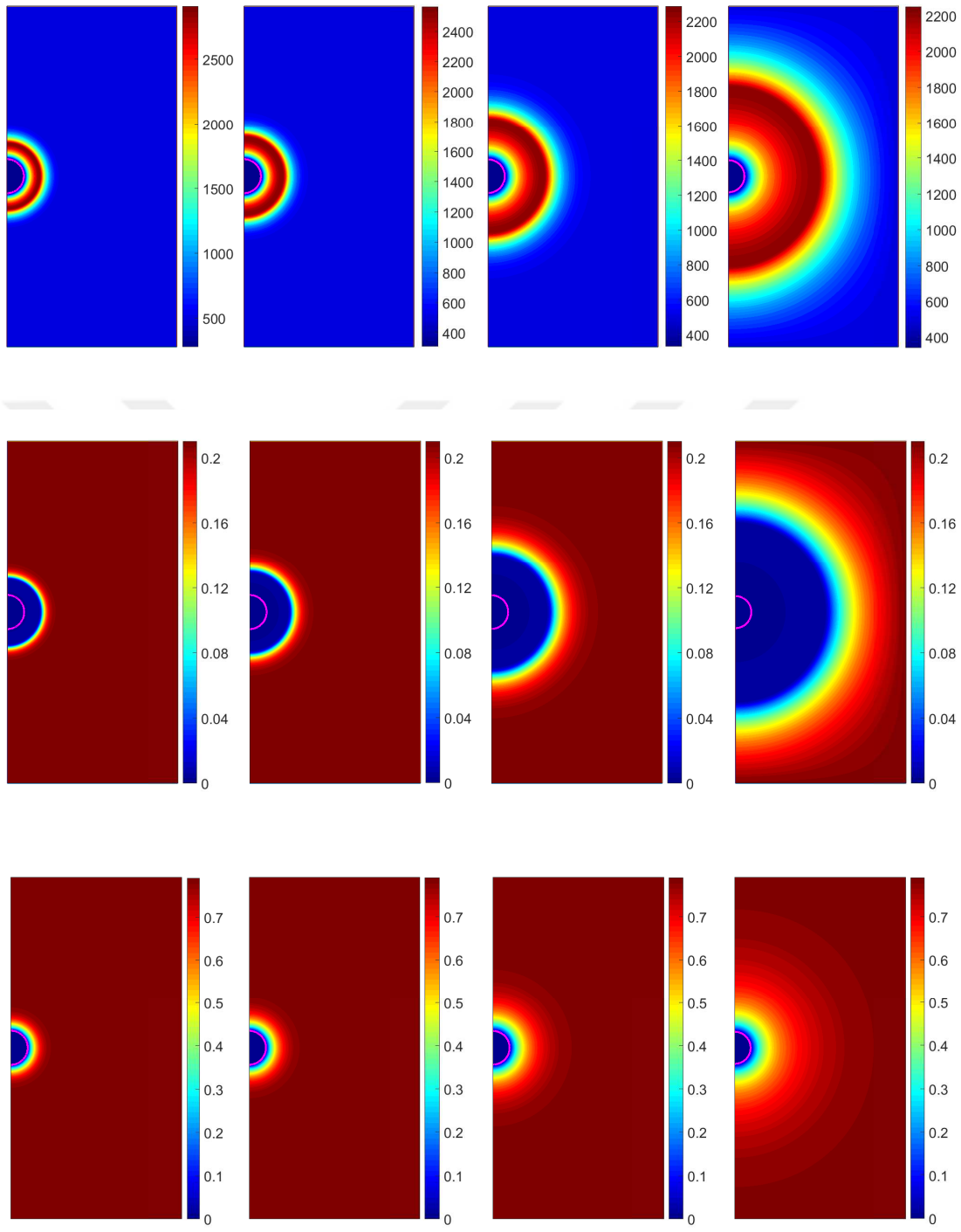

Figure 5.11: Contour plots of temperature (top row), oxygen mass fraction (middle row) and nitrogen mass fraction (bottom row) showing their evolution in time for an evaporating and burning n-heptane droplet at t/d_o^2 (from left to right in each row) = 0.00375, 0.0084, 0.0343 and 0.1875. The initial droplet diameter d_o is 0.4 mm. Grid: 256×512.

to the right there is no fuel. All the fuel transported to the flame front is burnt to produce the combustion products. There is an equilibrium between the fuel gasification and consumption, termed as the steady state condition; the flame temperature being constant during that condition. The initial flame diameter is approximately 1

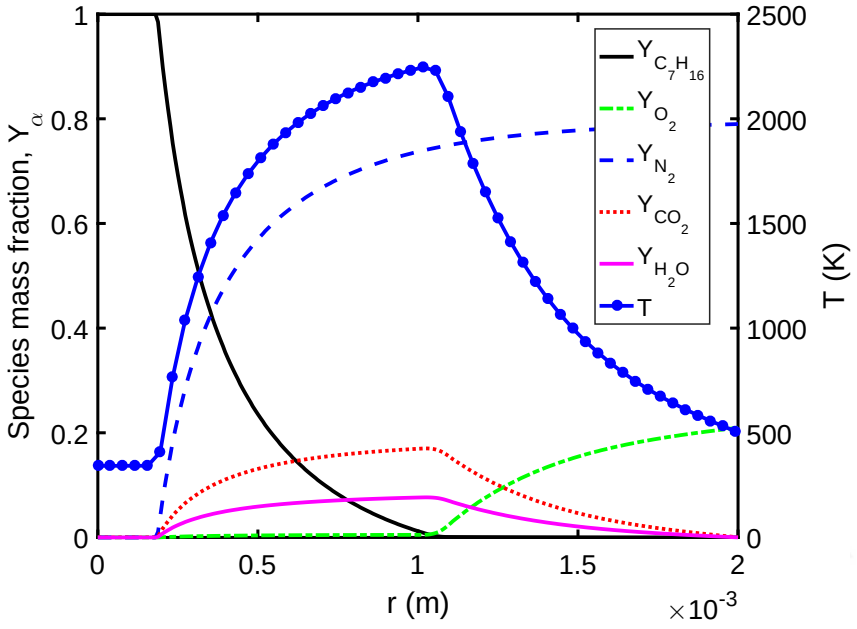

Figure 5.12: Profiles of the temperature and species mass fractions along the horizontal centerline ($z = 5d_o$) of the domain at time $t/d_o^2 = 0.1875$. Peak temperature shows the location of the flame front, species mass fraction fields also show a sharp gradient at that point. The initial droplet diameter d_o is 0.4 mm. Grid: 256 $\times$ 512.

mm which continuously increases before reaching a steady state value. This trend is shown in Fig. 5.13 along with the flame standoff ratio (d_f/d). For this particular test case a bigger domain is used so that the flame size can reach a steady state value. The domain is $10d_o$ in the radial and $20d_o$ in the axial coordinate directions and is resolved using 512 $\times$ 1024 grid cells. It is observed that the ignition starts with a standoff value of 2.5; this is consistent with the previous numerical studies [54, 73]. The standoff value follows the trend of flame diameter but continues to increase linearly as expected, and more quickly towards the end of droplet life time, because the

droplet diameter d is continuously decreasing.

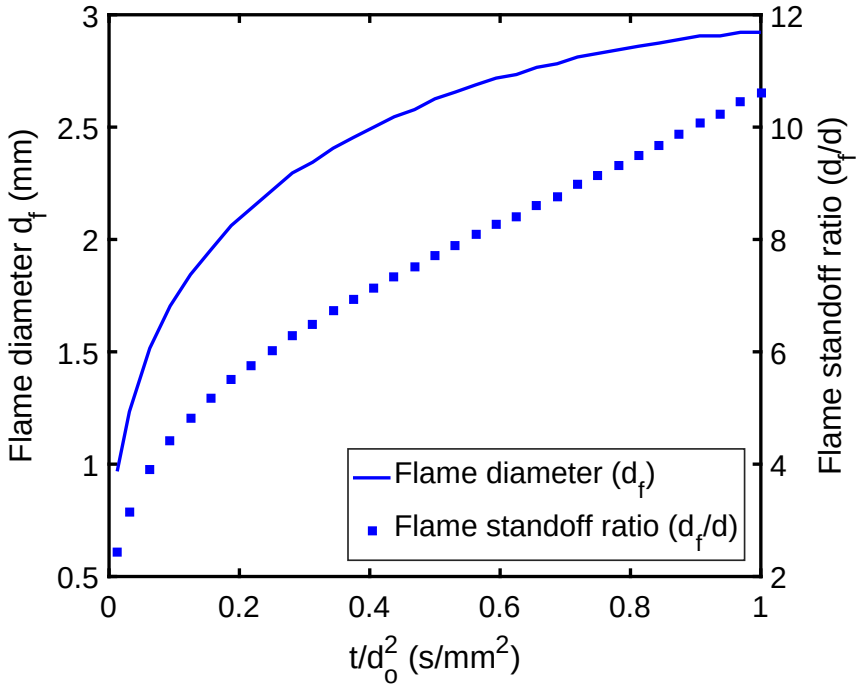

Figure 5.13: Flame diameter (d_f) and standoff ratio (d_f/d) plotted against t/d_o^2 for a burning n-heptane droplet (d_o = 0.4 mm). The flame diameter approaches to a steady state value which, in our observation, is a strong function of the domain size. However, the standoff ratio is expected to increase till the whole droplet is burnt out. The domain size for this case is $10d_o$ is radial and $20d_o$ in axial directions. Grid: 512 $\times$ 1024.

5.4.2 Detailed Chemistry Calculations using a Reduced Chemical Kinetic Mechanism

A reduced chemical kinetic mechanism for n-heptane combustion, comprising of 25 species and 26 reactions [93] (Table 5.1), is then used to rigorously test the functionality of our solver by simulating the evaporation and combustion of a n-heptane droplet. The contours of temperature and OH mass fraction are plotted side by side sharing the common centerline as shown in Fig. 5.14. The contours of maximum temperature and OH mass fraction coincide to mark the location of the propagating flame front

which is quite expected and qualitatively true. To verify our results quantitatively, a test case is simulated to determine the ignition delay times (t_{ign}) during the autoignition of a n-heptane droplet under isobaric condition for various values of gas phase temperature T_g. In contrary to our previous simulations, there is no localized artificial heating of the gas domain near the droplet in this particular test case since we are focusing on the autoignition. Comparison is made with the numerical results of Stauch et al. [55] who also studied a similar case to analyze the effect of gas phase temperature on the ignition delay times. The results compare very well as shown in Fig. 5.15 despite the fact that there are some differences in the physical and computational settings for the two compared cases. Also, Stauch et al. [55] used a more detailed chemical mechanism as compared to the present study. It is observed that the ignition delay time is a strong function of gas phase temperature and decreases as the gas phase temperature is increased.

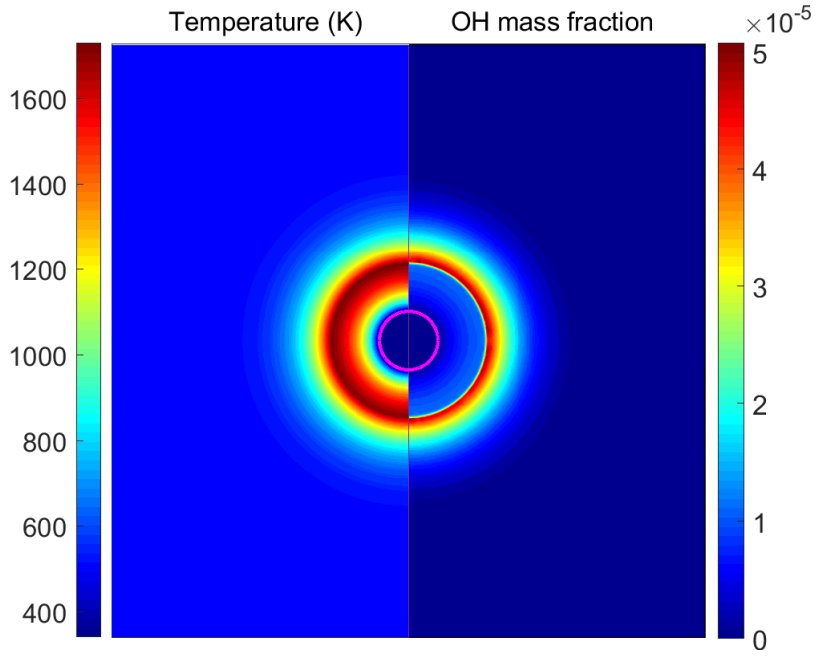

Figure 5.14: Contour plots of temperature and OH mass fraction for a burning n-heptane droplet at $t = 5.5$ msec using reduced chemical kinetic mechanism given in Table 5.1. The gas phase temperature is $T_g = 500$ K and pressure $p = 10$ atm. The domain size is $5d_o$ in radial and $10d_o$ in axial directions where initial diameter $d_o = 0.4$ mm. Grid: 256×512.

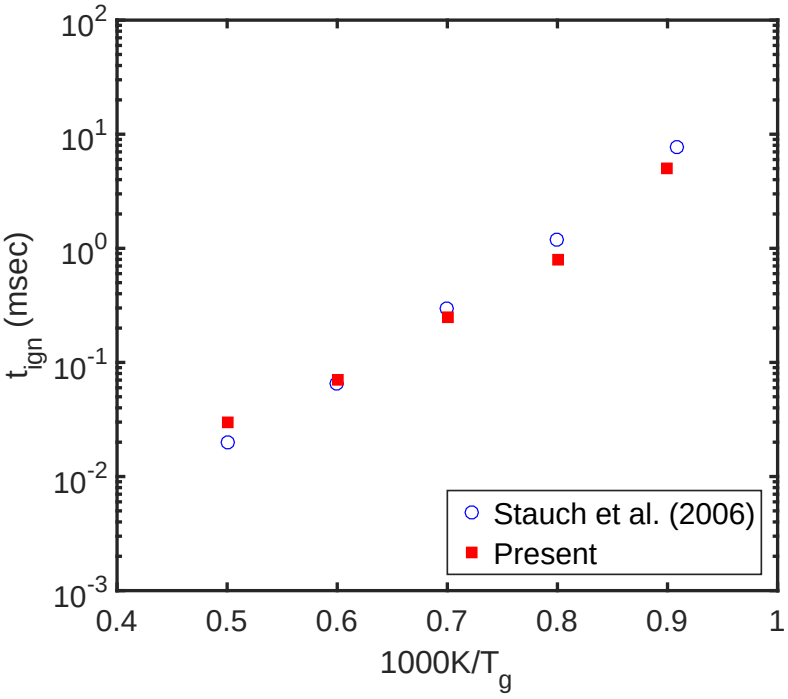

Figure 5.15: The numerical results of ignition delay time t_{ign} compared with the results from a previous numerical study by Stauch et al. (2006) for various gas phase temperatures T_g and $p = 7$ atm. The reduced chemical kinetic mechanism is used as given in Table 5.1. The domain size is $2.5d_o$ is radial and $5d_o$ in axial directions where initial diameter $d_o = 0.4$ mm. Grid: 128×256.

Table 5.1: Reduced mechanism for *n*-heptane combustion. Units: cm-sec-mole-cal-K

No.	Reaction	*A*	*b*	*E*
1	$C_7H_{16} + O_2 = C_7H_{15-2} + HO_2$	2.800E+14	0.0	47180.0
2	$C_7H_{16} + OH = C_7H_{15-2} + H_2O$	4.800E+09	1.3	690.5
3	$C_7H_{15-2} + O_2 = C_7H_{15}O_2$	2.000E+12	0.0	0.0
4	$C_7H_{15}O_2 = C_7H_{14}O_2H$	6.000E+11	0.0	20380.0
5	$C_7H_{14}O_2H + O_2 = C_7H_{14}O_2HO_2$	2.340E+11	0.0	0.0
6	$C_7H_{14}O_2HO_2 = C_7KET21 + OH$	2.965E+13	0.0	26700.0
7	$C_7KET21 = C_5H_{11}CO + CH_2O + OH$	1.000E+16	0.0	42400.0
8	$C_5H_{11}CO = C_2H_5 + C_3H_6 + CO$	1.000E+11	0.0	9600.0
9	$C_7H_{15-2} = CH_3 + 2C_3H_6$	3.000E+13	0.0	29800.0
10	$C_7H_{15-2} = C_2H_5 + C_2H_4 + C_3H_6$	1.200E+13	0.0	29600.0
11	$C_3H_6 + OH = CH_3CHO + CH_3$	3.500E+11	0.0	0.0
12	$CH_3CHO + OH = CH_3 + CO + H_2O$	1.000E+13	0.0	0.0
13	$CH_3 + HO_2 = CH_2O + H + OH$	4.300E+13	0.0	0.0
14	$CO + OH = CO_2 + H$	3.510E+07	1.3	-758.0
15	$O + OH = O_2 + H$	4.000E+14	-0.5	0.0
16	$H + O_2 + M = HO_2 + M$	2.800E+18	-0.86	0.0
	Enhanced third body efficiencies:			
	$O_2 = 0$, $H_2O = 0$, CO = 0.75,			
	$CO_2 = 1.5$, $C_2H_6 = 1.5$, $N_2 = 0$			
17	$H + O_2 + N_2 = HO_2 + N_2$	2.600E+19	-1.24	0.0
18	$HO_2 + HO_2 = H_2O_2 + O_2$	2.000E+12	0.0	0.0
19	$OH + OH (+M) = H_2O_2 + (+M)$	7.600E+13	-0.37	0.0
	Low	4.300E+18	-0.9	-1700.0
	TROE parameters: 0.7346, 94, 1756, 5182			
	Enhanced third body efficiencies:			
	$H_2O = 6$, CO = 1.5, $CO_2 = 2$,			
	$C_2H_6 = 3$, $N_2 = 0.7$, $CH_4 = 2$			
20	$CH_2O + OH = HCO + H_2O$	2.430E+10	1.18	-447.0
21	$CH_2O + HO_2 = HCO + H_2O_2$	3.000E+12	0.0	8000.0
22	$HCO + O_2 = HO_2 + CO$	3.300E+13	-0.4	0.0
23	$CH_4 + O = CH_3 + OH$	1.020E+09	1.5	8604.0
24	$CH_4 + HO_2 = CH_3 + H_2O_2$	1.000E+13	0.0	18700.0
25	$C_2H_4 + OH = CH_2O + CH_3$	6.000E+13	0.0	960.0
26	$C_2H_5 + O_2 = C_2H_4 + HO_2$	2.000E+10	0.0	-2200.0

Chapter 6

CONCLUSION

A finite-difference/front-tracking method is developed for the direct numerical simulation of liquid-vapor phase change phenomenon followed by chemical reaction. A one-field formulation is used to solve the governing equations on a fixed uniform Eulerian grid whereas the interface is represented by a separate Lagrangian grid. Different interpolation schemes are used to communicate between these two grids. The Navier-Stokes equations are solved using a projection method, satisfying the modified continuity equation, whereas the energy and species equations are advanced in time using an explicit Euler method. The temperature gradient based phase change model is first validated using the benchmark cases: the Stefan and the sucking interface problems and the d^2-law. Results are demonstrated to be grid convergent and are in excellent agreement with the analytical solutions. The spherical symmetry of the droplet is perfectly maintained during the course of evaporation. Two-dimensional moving droplet case is then simulated in a 2D planar configuration. Moving droplets take different shapes depending on the Eo and Mo numbers. Simulations are performed for substantially deformed droplet cases and the numerical method is demonstrated to be grid convergent and mass conservant.

The species gradient based evaporation model employs the Clausius-Clapeyron equilibrium relation to compute species mass fraction at the interface and subsequently computes the evaporation mass flux. Species mass fraction boundary condition at the interface is implemented using two strategies. The one that considers evaporative mass flux as a source term is found to be numerically efficient, easy to implement, gives better global mass conservation results and can easily be extended to 3D configuration. The implementation is validated using a simplified test case

for which analytical solution is available in literautre. An excellent agreement is observed between the numerical and analytical results as the grid is refined. In the steady state condition, a static evaporating droplet attains thermal equilibrium with the air temperature at the interface called the wet bulb temperature, and can be read from a psychrometric chart. For various combinations of the dry bulb temperatures and relative humidities, the numerical results of wet bulb temperatures compare very well with the psychrometric chart values. These results ensure the correct coupling of the Clausius-Clapeyron relation with the solution of the flow, energy and species conservation equations. We observed that, for the novel species gradient based evaporation model, approximately 40% of the total computational time is utilized by the phase change solver for a static droplet evaporation case. Also it is observed that the non-conservative form of governing equations behave well when working with large gradients across the interface. The method can also handle highly deformed moving droplet as well as multiple droplets systems as may be the case in the combustion chamber of the internal combustion engines.

The temperature gradient based phase change solver in then incorporated into the axisymmetric multiphase solver for direct comparison of numerical results with the experimental data and previous numerical studies. The d^2-law is satisfied for a static evaporating droplet for various Stefan numbers. n-heptane droplet evaporation is then simulated and results are compared with the experimental as well as previous numerical results with good degree of accuracy. The evaporated fuel vapors then undergo chemical reaction with the ambient oxygen to produce the reaction products. We use single step as well as reduced chemical kinetic mechanism for n-heptane; the chemical kinetics in the gas phase being handled by the CHEMKIN. An operator-splitting approach is used to advance temperature and species mass fraction in time. The gasification rate, normalized d^2, peak temperatures and ignition delay times compare well with the previous numerical results; the discrepancies arise due to slight differences in the computational domain setup, operating parameters and chemical kinetic mechanisms. The contours and the line plots of temperature and

species mass fractions qualitatively confirms the accuracy of our results. The initial flame diameter and flame standoff ratio also compare well with the previous studies. The present numerical results can be compared with the experiments only in a qualitative sense because a real burning droplet experiences various degrees of motion relative to the gas and contains a significant amount of soot in the flame envelope which is not considered here [54]. The detailed chemistry and variable transport and thermodynamic properties are expected to further enhance the quality of our results.

Future Work

The capabilities of the current solver developed to simulate the evaporation and combustion of fuel droplets can further be enhanced to tackle the real world problems of practical interest. The first and logical step is the extension of the solver to full 3D configuration to model the real physical systems. Fuel sprays are of fundamental importance in many combustion systems. To study the spray combustion, multiple droplet systems comprising of thousands of fuel droplets needs to be simulated. The computationally efficient studies can be performed by designing parallel algorithms and using the Adaptive Mesh Refinement (AMR). Parametric studies can be performed to determine the systems operating conditions for an efficient combustion system. Another area of possible application is the evaporation and combustion of multicomponent droplets.

BIBLIOGRAPHY

[1] F. H. Harlow and J. E. Welch, "Numerical calculation of time dependent viscous incompressible flow of fluid with free surface," *Phys. Fluids*, vol. 8, no. 12, pp. 2182–2189, 1965.

[2] C. Hirt and B. Nichols, "Volume of fluid (VOF) method for the dynamics of free boundaries," *J. Comput. Phys.*, vol. 39, no. 1, pp. 201 – 225, 1981.

[3] S. Osher and J. A. Sethian, "Fronts propagating with curvature-dependent speed: Algorithms based on hamilton-jacobi formulations," *J. Comput. Phys.*, vol. 79, pp. 12–49, Nov. 1988.

[4] M. Sussman, P. Smereka, and S. Osher, "A level set approach for computing solutions to incompressible two-phase flow," *J. Comput. Phys.*, vol. 114, no. 1, pp. 146 – 159, 1994.

[5] D. M. Anderson, G. B. McFadden, and A. A. Wheeler, "Diffuse-interface methods in fluid mechanics," *Annu. Rev. Fluid Mech.*, vol. 30, no. 1, pp. 139–165, 1998.

[6] D. Jacqmin, "Calculation of two-phase navierstokes flows using phase-field modeling," *J. Comput. Phys.*, vol. 155, no. 1, pp. 96 – 127, 1999.

[7] J. Glimm, D. Marchesin, and O. McBryan, "A numerical method for two phase flow with an unstable interface," *J. Comput. Phys.*, vol. 39, no. 1, pp. 179 – 200, 1981.

[8] J. Glimm, E. Isaacson, D. Marchesin, and O. McBryan, "Front tracking for hyperbolic systems," *Adv. in Appl. Math.*, vol. 2, no. 1, pp. 91 – 119, 1981.

[9] J. Glimm and O. A. McBryan, "A computational model for interfaces," *Adv. in Appl. Math.*, vol. 6, no. 4, pp. 422 – 435, 1985.

[10] S. O. Unverdi and G. Tryggvason, "A front-tracking method for viscous, incompressible, multi-fluid flows," *J. Comput. Phys.*, vol. 100, no. 1, pp. 25 – 37, 1992.

[11] G. Tryggvason, B. Bunner, A. Esmaeeli, D. Juric, N. Al-Rawahi, W. Tauber, J. Han, S. Nas, and Y.-J. Jan, "A front-tracking method for the computations of multiphase flow," *J. Comput. Phys.*, vol. 169, no. 2, pp. 708 – 759, 2001.

[12] M. Woerner, "Numerical modeling of multiphase flows in microfluidics and micro process engineering: a review of methods and applications," *Microfluid Nanofluid*, vol. 12, no. 6, pp. 841–886, 2012.

[13] S. W. Welch and J. Wilson, "A volume of fluid based method for fluid flows with phase change," *J. Comput. Phys.*, vol. 160, no. 2, pp. 662 – 682, 2000.

[14] J. Schlottke and B. Weigand, "Direct numerical simulation of evaporating droplets," *J. Comput. Phys.*, vol. 227, no. 10, pp. 5215 – 5237, 2008.

[15] G. Son and V. Dhir, "Numerical simulation of film boiling near critical pressures with a level set method," *ASME J. Heat Transfer*, vol. 120, no. 1, pp. 183–192, 1998.

[16] F. Gibou, L. Chen, D. Nguyen, and S. Banerjee, "A level set based sharp interface method for the multiphase incompressible navierstokes equations with phase change," *J. Comput. Phys.*, vol. 222, no. 2, pp. 536 – 555, 2007.

[17] R. P. Fedkiw, T. Aslam, B. Merriman, and S. Osher, "A non-oscillatory eulerian approach to interfaces in multimaterial flows (the ghost fluid method)," *J. Comput. Phys.*, vol. 152, no. 2, pp. 457 – 492, 1999.

[18] S. Tanguy, T. Menard, and A. Berlemont, "A level set method for vaporizing two-phase flows," *J. Comput. Phys.*, vol. 221, no. 2, pp. 837 – 853, 2007.

[19] H. Safari, M. H. Rahimian, and M. Krafczyk, "Extended lattice boltzmann method for numerical simulation of thermal phase change in two-phase fluid flow," *Phys. Rev. E*, vol. 88, p. 013304, Jul 2013.

[20] H. Safari, M. H. Rahimian, and M. Krafczyk, "Consistent simulation of droplet evaporation based on the phase-field multiphase lattice boltzmann method," *Phys. Rev. E*, vol. 90, p. 033305, Sep 2014.

[21] T. Lee, "Effects of incompressibility on the elimination of parasitic currents in the lattice boltzmann equation method for binary fluids," *Comput. Math. Appl.*, vol. 58, pp. 987–994, Sept. 2009.

[22] D. Juric and G. Tryggvason, "Computations of boiling flows," *Int. J. Multiphase Flow*, vol. 24, no. 3, pp. 387 – 410, 1998.

[23] J. Qian, G. Tryggvason, and C. Law, "A front tracking method for the motion of premixed flames," *J. Comput. Phys.*, vol. 144, no. 1, pp. 52 – 69, 1998.

[24] A. Esmaeeli and G. Tryggvason, "Computations of explosive boiling in microgravity," *J. Sci. Comput.*, vol. 19, no. 1, pp. 163–182, 2003.

[25] A. Esmaeeli and G. Tryggvason, "Computations of film boiling. part I: numerical method," *Int. J. Heat Mass Transfer*, vol. 47, no. 25, pp. 5451 – 5461, 2004.

[26] A. Koynov, J. G. Khinast, and G. Tryggvason, "Mass transfer and chemical reactions in bubble swarms with dynamic interfaces," *AIChE Journal*, vol. 51, no. 10, pp. 2786–2800, 2005.

[27] B. Aboulhasanzadeh, S. Thomas, M. Taeibi-Rahni, and G. Tryggvason, "Multiscale computations of mass transfer from buoyant bubbles," *Chem. Eng. Sci.*, vol. 75, pp. 456 – 467, 2012.

[28] A. Esmaeeli and G. Tryggvason, "Computations of film boiling. Part II: multi-mode film boiling," *Int. J. Heat Mass Transfer*, vol. 47, no. 25, pp. 5463 – 5476, 2004.

[29] D. Juric and G. Tryggvason, "A front-tracking method for dendritic solidification," *J. Comput. Phys.*, vol. 123, no. 1, pp. 127 – 148, 1996.

[30] N. Al-Rawahi and G. Tryggvason, "Numerical simulation of dendritic solidification with convection: Two-dimensional geometry," *J. Comput. Phys.*, vol. 180, no. 2, pp. 471 – 496, 2002.

[31] N. Al-Rawahi and G. Tryggvason, "Numerical simulation of dendritic solidification with convection: Three-dimensional flow," *J. Comput. Phys.*, vol. 194, no. 2, pp. 677 – 696, 2004.

[32] T. V. Vu, G. Tryggvason, S. Homma, and J. C. Wells, "Numerical investigations of drop solidification on a cold plate in the presence of volume change," *Int. J. Multiphase Flow*, vol. 76, pp. 73 – 85, 2015.

[33] S. Kotake and T. Okazaki, "Evaporation and combustion of a fuel droplet," *Int. J. Heat Mass Transfer*, vol. 12, no. 5, pp. 595 – 609, 1969.

[34] K. Kobayashi, "On the evaporation rate of a liquid droplet in a hot gas," *J. Japan Soc. Mech. Engrs*, vol. 15, pp. 14 – 19, 1949.

[35] G. Godsave, "Studies of the combustion of drops in a fuel spraythe burning of single drops of fuel," *Symp. (Int.) Combust.*, vol. 4, no. 1, pp. 818 – 830, 1953.

[36] D. Spalding, "The combustion of liquid fuels," *Symp. (Int.) Combust.*, vol. 4, no. 1, pp. 847 – 864, 1953.

[37] G. Faeth, "Current status of droplet and liquid combustion," *Prog. Energy Combust. Sci.*, vol. 3, no. 4, pp. 191 – 224, 1977.

[38] C. Law, S. Chung, and N. Srinivasan, "Gas-phase quasi-steadiness and fuel vapor accumulation effects in droplet burning," *Combust. Flame*, vol. 38, pp. 173 – 198, 1980.

[39] C. Law, "Recent advances in droplet vaporization and combustion," *Prog. Energy Combust. Sci.*, vol. 8, no. 3, pp. 171 – 201, 1982.

[40] W. A. Sirignano, "Fuel droplet vaporization and spray combustion theory," *Prog. Energy Combust. Sci.*, vol. 9, no. 4, pp. 291 – 322, 1983.

[41] A. H. Lefebvre, *Atomization and Sprays*. Hemisphere Publishing Corporation, New York, 1989.

[42] G. Toker and J. Stricker, "Holographic study of suspended vaporizing volatile liquid droplets in still air," *Int. J. Heat Mass Transfer*, vol. 39, no. 16, pp. 3475 – 3482, 1996.

[43] S. Sazhin, W. Abdelghaffar, E. Sazhina, and M. Heikal, "Models for droplet transient heating: Effects on droplet evaporation, ignition, and break-up," *Int. J. Therm. Sci.*, vol. 44, no. 7, pp. 610 – 622, 2005.

[44] B. Abramzon and W. Sirignano, "Droplet vaporization model for spray combustion calculations," *Int. J. Heat Mass Transfer*, vol. 32, no. 9, pp. 1605 – 1618, 1989.

[45] S. S. Sazhin, "Advanced models of fuel droplet heating and evaporation," *Prog. Energy Combust. Sci.*, vol. 32, no. 2, pp. 162 – 214, 2006.

[46] W. A. Sirignano, *Fluid Dynamics and Transport of Droplets and Sprays*. Cambridge University Press, 2 ed., 2010.

[47] C. G. Downing, "The evaporation of drops of pure liquids at elevated temperatures: Rates of evaporation and wet-bulb temperatures," *AIChE J.*, vol. 12, no. 4, pp. 760–766, 1966.

[48] M. C. Yuen and L. W. Chen, "On drag of evaporating liquid droplets," *Comb. Sci. Tech.*, vol. 14, no. 4-6, pp. 147–154, 1976.

[49] S. C. Wong and A. C. Lin, "Internal temperature distributions of droplets vaporizing in high-temperature convective flows," *J. Fluid Mech.*, vol. 237, p. 671687, 1992.

[50] H. Nomura, Y. Ujiie, H. J. Rath, J. Sato, and M. Kono, "Experimental study on high-pressure droplet evaporation using microgravity conditions," *Proc. Combust. Inst.*, vol. 26, no. 1, pp. 1267 – 1273, 1996.

[51] D. L. Dietrich, P. M. Struk, M. Ikegami, and G. Xu, "Single droplet combustion of decane in microgravity: experiments and numerical modelling," *Combust. Theory Model.*, vol. 9, no. 4, pp. 569–585, 2005.

[52] R. Miller, K. Harstad, and J. Bellan, "Evaluation of equilibrium and non-equilibrium evaporation models for many-droplet gas-liquid flow simulations," *Int. J. Multiphase Flow*, vol. 24, no. 6, pp. 1025 – 1055, 1998.

[53] H. Zhang, "Numerical research on a vaporizing fuel droplet in a forced convective environment," *Int. J. Multiphase Flow*, vol. 30, no. 2, pp. 181 – 198, 2004.

[54] S. Cho and F. Dryer, "A numerical study of the unsteady burning behaviour of n-heptane droplets," *Combust. Theory Model.*, vol. 3, no. 2, pp. 267–280, 1999.

[55] R. Stauch, S. Lipp, and U. Maas, "Detailed numerical simulations of the autoignition of single n-heptane droplets in air," *Combust. Flame*, vol. 145, no. 3, pp. 533 – 542, 2006.

[56] Y. Wang and C. Rutland, "Direct numerical simulation of ignition in turbulent n-heptane liquid-fuel spray jets," *Combust. Flame*, vol. 149, no. 4, pp. 353 – 365, 2007.

[57] I. Awasthi, D. N. Pope, and G. Gogos, "Effects of the ambient temperature and initial diameter in droplet combustion," *Combust. Flame*, vol. 161, no. 7, pp. 1883 – 1899, 2014.

[58] M. Ashna and M. H. Rahimian, "LMB simulation of head-on collision of evaporating and burning droplets in coalescence regime," *Int. J. Heat Mass Transfer*, vol. 109, pp. 520 – 536, 2017.

[59] R. Stauch and U. Maas, "The ignition of methanol droplets in a laminar convective environment," *Combust. Flame*, vol. 153, no. 1, pp. 45 – 57, 2008.

[60] I. Awasthi, G. Gogos, and T. Sundararajan, "Effects of size on combustion of isolated methanol droplets," *Combust. Flame*, vol. 160, no. 9, pp. 1789 – 1802, 2013.

[61] M. Irfan and M. Muradoglu, "A front tracking method for direct numerical simulation of evaporation process in a multiphase system," *J. Comput. Phys.*, vol. 337, pp. 132 – 153, 2017.

[62] M. Muradoglu and G. Tryggvason, "A front-tracking method for computation of interfacial flows with soluble surfactants," *J. Comput. Phys.*, vol. 227, no. 4, pp. 2238 – 2262, 2008.

[63] M. Muradoglu and G. Tryggvason, "Simulations of soluble surfactants in 3d multiphase flow," *J. Comput. Phys.*, vol. 274, pp. 737 – 757, 2014.

[64] F. Gibou, R. P. Fedkiw, L. T. Cheng, and M. Kang, "A second-order-accurate symmetric discretization of the poisson equation on irregular domains," *J. Comput. Phys.*, vol. 176, no. 1, pp. 205 – 227, 2002.

[65] Y. Sato and B. Niceno, "A sharp-interface phase change model for a mass-conservative interface tracking method," *J. Comput. Phys.*, vol. 249, pp. 127 – 161, 2013.

[66] S. Turns, *An Introduction to Combustion: Concepts and Applications*. McGraw-Hill, New York, 2000.

[67] R. Kee, F. Rupley, and J. Miller, *Chemkin-II: A Fortran chemical kinetics package for the analysis of gas-phase chemical kinetics*. 1989.

[68] R. J. Kee, F. M. Rupley, E. Meeks, and J. A. Miller, "CHEMKIN-III: A FORTRAN chemical kinetics package for the analysis of gas-phase chemical and plasma kinetics," *Sandia national laboratories report SAND96-8216*, 1996.

[69] M. S. Day and J. B. Bell, "Numerical simulation of laminar reacting flows with complex chemistry," *Combust. Theory Model.*, vol. 4, no. 4, pp. 535–556, 2000.

[70] A. Cuoci, A. Frassoldati, T. Faravelli, and E. Ranzi, "Numerical modeling of laminar flames with detailed kinetics based on the operator-splitting method," *Energy Fuels*, vol. 27, no. 12, pp. 7730–7753, 2013.

[71] A. Cuoci, A. Frassoldati, T. Faravelli, and E. Ranzi, "A computational tool for the detailed kinetic modeling of laminar flames: Application to C2H4/CH4 coflow flames," *Combust. Flame*, vol. 160, no. 5, pp. 870 – 886, 2013.

[72] S. MacNamara and G. Strang, *Operator Splitting*, pp. 95–114. Springer International Publishing, 2016.

[73] Y. Jin and B. Shaw, "Computational modeling of n-heptane droplet combustion in airdiluent environments under reduced-gravity," *Int. J. Heat Mass Transfer*, vol. 53, no. 25, pp. 5782 – 5791, 2010.

[74] S. Nas, M. Muradoglu, and G. Tryggvason, "Pattern formation of drops in thermocapillary migration," *Int. J. Heat Mass Transfer*, vol. 49, no. 1314, pp. 2265 – 2276, 2006.

[75] G. Tryggvason, R. Scardovelli, and S. Zaleski, *Direct numerical simulations of gas–liquid multiphase flows*. Cambridge University Press, 2011.

[76] A. J. Chorin, "Numerical solution of the Navier-Stokes equations," *Math. Comp.*, vol. 22, pp. 745–762, 1968.

[77] R. Borges, M. Carmona, B. Costa, and W. S. Don, "An improved weighted essentially non-oscillatory scheme for hyperbolic conservation laws," *J. Comput. Phys.*, vol. 227, no. 6, pp. 3191 – 3211, 2008.

[78] J. C. Adams, "MUDPACK: Multigrid portable fortran software for the efficient solution of linear elliptic partial differential equations," *Appl. Math. Comput.*, vol. 34, no. 2, pp. 113 – 146, 1989.

[79] H. S. Udaykumar, W. Shyy, and M. M. Rao, "ELAFINT: A mixed eulerianlagrangian method for fluid flows with complex and moving boundaries," *Int. J. Numer. Meth. Fl.*, vol. 22, no. 8, pp. 691–712, 1996.

[80] C. S. Peskin, "Numerical analysis of blood flow in the heart," *J. Comput. Phys.*, vol. 25, no. 3, pp. 220 – 252, 1977.

[81] G. R. Guedon, *Two-phase heat and mass transfer modeling: flexible numerical methods for energy engineering analyses*. Ph.D. Thesis, Politecnico Di Milano, Italy, 2013. `http://hdl.handle.net/10589/82788`.

[82] W. M. Kays and M. E. Crawford, *Convective heat and mass transfer*. Third ed., McGraw-Hill, New York, USA, 1993.

[83] P. Tsilingiris, "Thermophysical and transport properties of humid air at temperature range between 0 and 100 c," *Energ. Convers. Manage.*, vol. 49, no. 5, pp. 1098 – 1110, 2008.

[84] J. Han and G. Tryggvason, "Secondary breakup of axisymmetric liquid drops. i. acceleration by a constant body force," *Phys. Fluids*, vol. 11, no. 12, pp. 3650–3667, 1999.

[85] M. Muradoglu and A. D. Kayaalp, "An auxiliary grid method for computations of multiphase flows in complex geometries," *J. Comput. Phys.*, vol. 214, no. 2, pp. 858 – 877, 2006.

[86] G. Williams, "Combustion theory," Addison-Wesley, 1985.

[87] J. R. Yang and S. C. Wong, "An experimental and theoretical study of the effects of heat conduction through the support fiber on the evaporation of a droplet in a weakly convective flow," *Int. J. Heat Mass Transfer*, vol. 45, no. 23, pp. 4589 – 4598, 2002.

[88] C. Chauveau, M. Birouk, and I. Gkalp, "An analysis of the d2-law departure during droplet evaporation in microgravity," *Int. J. Multiphase Flow*, vol. 37, no. 3, pp. 252 – 259, 2011.

[89] P. N. Brown, G. D. Byrne, and A. C. Hindmarsh, "VODE: A variable-coefficient ode solver," *SIAM J. Sci. Stat. Comput.*, vol. 10, no. 5, pp. 1038–1051, 1989.

[90] H. Hara and S. Kumagai, "Experimental investigation of free droplet combustion under microgravity," *Proc. Combust. Inst.*, vol. 23, no. 1, pp. 1605 – 1610, 1991. Twenty-Third Symposium (International) on Combustion.

[91] G. S. Jackson and C. T. Avedisian, "The effect of initial diameter in spherically symmetric droplet combustion of sooting fuels," *Proc. R. Soc. London Ser. A Math. Phys. Eng. Sci.*, vol. 446, no. 1927, pp. 255–276, 1994.

[92] B. Vieille, C. Chauveau, X. Chesneau, A. Odede, and I. Gkalp, "High-pressure droplet burning experiments in microgravity," *Proc. Combust. Inst.*, vol. 26, no. 1, pp. 1259 – 1265, 1996.

[93] F. Maroteaux and L. Noel, "Development of a reduced n-heptane oxidation mechanism for HCCI combustion modeling," *Combust. Flame*, vol. 146, no. 1, pp. 246 – 267, 2006.